Toward Efficient Electrochemical Reduction of CO_2 to CO: Decorating ZnO nanorods with Cu_xO

by

Muhammed Yusufoğlu

A Dissertation Submitted to the
Graduate School of Sciences and Engineering
in Partial Fulfillment of the Requirements for
the Degree of

Master of Science

in

Materials Science and Engineering

KOÇ
ÜNİVERSİTESİ

August 04, 2023

Toward Efficient Electrochemical Reduction of CO_2 to CO: Decorating ZnO nanorods with Cu_xO

Koç University

Graduate School of Sciences and Engineering

This is to certify that I have examined this copy of a master's thesis by

Muhammed Yusufoğlu

and have found that it is complete and satisfactory in all respects,
and that any and all revisions required by the final
examining committee have been made.

Committee Members:

Assoc.Prof.Sarp Kaya (Advisor)

Dr.Timuçin Balkan (Co-Advisor)

Assoc. Prof. Uğur Ünal

Assist. Prof. Alp Yürüm

Date: August.04.2023

To my mother

For she enveloped me in her love even when self-loathing consumed me,

and forever served as both my refuge and my anchor in the tumultuous sea of life,

for she stood resolutely by my side when the world turned its back on me.

To my father

In your teachings, I found strength,

In your wisdom, I discovered purpose,

In your prayers, our life remains unbroken.

ABSTRACT

Toward Efficient Electrochemical Reduction of CO_2 to CO: Decorating ZnO Nanorods with Cu_xO

Muhammed Yusufoğlu

Master of Science in Materials Science and Engineering

August 04, 2023

This thesis investigates Cu_xO-ZnO based electrocatalyst as a potential cost-effective electrocatalyst for electrochemical reduction of CO_2 to CO (CO_2RR). CO_2RR is a viable solution that can offer a potential source of energy while also reducing the amount of CO_2 in the atmosphere. CO_2RR to CO presents a promising route due to having the highest economical visibility among other targeted products. In response, we have synthesized and examined two sets of Cu_xO-ZnO electrocatalysts derived from earth-abundant elements that have high Faradic efficiency (FE) for CO, exceeding 70%.

We initially synthesized Cu_xO/ZnO electrocatalysts with different amounts of Cu_xO, using the electrodeposition technique. The optimized Cu_xO/ZnO electrode exhibited elevated selectivity towards CO, achieving a Faradaic efficiency (FE) of 75% at a low overpotential of -0.8 V vs. RHE. This, in itself, marked a clear improvement from the performance of bare ZnO, which only achieved a CO selectivity of 48% under identical conditions. However, an even more significant enhancement in CO selectivity was observed when Cu_xO was introduced using atomic layer deposition (ALD). Specifically, the Cu_xO-250/ZnO electrode, prepared with 250 ALD cycles, exhibited a remarkable CO selectivity of 88% at the same potential, demonstrating the superior performance of ALD Cu_xO/ZnO over both bare ZnO and the electrodeposited Cu_xO/ZnO electrodes.

The addition of Cu_xO was found to enhance CO selectivity through the introduction of the new active phase ε-$CuZn_4$ and a reduction in charge transfer resistance (R_{ct}). Furthermore, the incorporation of Cu_xO significantly influenced the surface reconstruction process, resulting in a distinct surface morphology for the Cu_xO/ZnO electrodes after CO_2RR. This led to an increased surface area compared to bare ZnO, suggesting a possible contribution to enhanced CO_2RR performance.

We also demonstrated that the applied potential substantially impacts the reconstruction process, affecting the Cu/Zn ratio at the surface, which in turn influences CO selectivity. We proved that after CO_2RR at -0.8 V, the Cu/Zn atomic ratio was higher than that after

-1.2 V of the same electrode, aligning with our findings on CO selectivity and highlighting the crucial role of surface Cu in CO production.

We further noted that after CO_2RR, the surface composition underwent significant changes, and the highest Cu/Zn ratio was not necessarily associated with the greatest initial amount of Cu. Rather, the maximum Cu/Zn ratio was observed in the Cu_xO-250/ZnO electrode, which also exhibited the highest FE of CO. We attribute this variation to the surface reconstruction process and the galvanic effect between Cu and Zn atoms, both of which influence the surface composition and, by extension, electrode selectivity.

In summary, this thesis presents a new earth-abundant electrocatalyst that is highly selective toward CO and provides new insights into the dynamic behavior and surface composition of Cu-Zn electrocatalysts during CO_2RR. These insights will significantly contribute to future studies aiming to design more effective and efficient Cu-Zn based electrocatalysts.

ÖZETÇE

CO_2'nin CO'ya verimli elektrokimyasal dönüşümü: ZnO Nanoçubuklarinin Cu_xO ile Dekorasyonu/Modifikasyonu

Muhammed Yusufoğlu

Malzeme Bilimi ve Mühendisliği, Yüksek Lisans

04 Ağustos 2023

Bu çalışma, maliyet/etkinlik açısından potansiyeli yüksek Cu_xO-ZnO elektrokatalizörlerinin CO_2'nin CO'ya elektrokimyasal indirgenme (CO_2RR) reaksiyonu üzerine elektro-katalitik etkisini incelemektedir. CO_2RR reaksiyonu hem enerji kaynağı sağlayabilmesi hem de eş zamanlı atmosferdeki CO_2 miktarını azaltabilmesi sebebiyle uygun bir çözüm sunmaktadır. Diğer hedeflenen ürünler arasında, CO_2'nin elektrokimyasal yol ile CO'ya dönüştürülmesi ve bu ürünün en yüksek ekonomik görünürlüğe sahip olması nedeniyle ön plana çıkmaktadır. Bu çerçevede, yapılan çalışmada yeryüzünde bol bulunan elementlerden türetilmiş iki set Cu_xO-ZnO elektrokatalizörleri sentezlenmiş ve incelenmiştir. Bu elektrokatalizörlerin CO için yüksek Faradaik verime (FE) sahip olduğu gösterilmiş ve bu verimlerin %70'i aştığı tespit edilmiştir.

Çalışmanın ilk kısmında, elektrodepozisyon tekniği kullanarak farklı miktarlarda Cu_xO'ya sahip Cu_xO/ZnO elektrokatalizörleri sentezlenmiştir. Optimize edilmiş Cu_xO/ZnO elektrodunun, -0.8 V (vs. RHE) düşük aşırı gerilimde %75 faradaik verimlilik (FE) ile yüksek CO seçiciliği göstermiştir. Bu sonuç çıplak ZnO'nun performansı ile kıyaslandığında belirgin bir iyileşmenin olduğunu göstermektedir., Çıplak ZnO'nun aynı koşullar altında CO'ya karşı gösterdiği seçicilik %48 faradik verime sahiptir.

İkinci kısımda, elektrokimyasal biriktirme yöntemi yerine atomik katman biriktirme (ALD) kullanılarak Cu_xO'nun ZnO üzerine kaplanması ile, CO seçiciliğinde daha da belirgin bir artışın olduğu bulunmuştur. Özellikle, 250 ALD döngüsü ile hazırlanan Cu_xO-250/ZnO elektrodu, aynı potansiyelde (-0.8V vs. RHE) CO seçiciliği %88 faradaik verime ulaşmıştır. Bu sonuçlar ALD yöntemi ile hazırlanan Cu_xO/ZnO elektrotlarının hem çıplak ZnO hem de elektrokimyasal biriktirme yöntemi ile hazırlanan Cu_xO/ZnO elektrotlarından üstün performansını göstermiştir.

Cu_xO'nun yapıya eklenmesinin potansiyel altında yeni aktif faz ε-$CuZn_4$'ün oluşumuna neden olduğu ve bununla bağlantılı olarak yük transfer direncindeki (R_{ct}) azalmanın CO seçiciliğini arttırdığı bulunmuştur. Ayrıca, Cu_xO'nun, CO_2RR sonrası Cu_xO/ZnO elektrotları için belirgin bir yüzey morfolojisine yol açarak, yüzeyin yeniden yapılanması sürecini önemli ölçüde etkilediği tespit edilmiştir. Bu da çıplak ZnO'ya kıyasla artmış bir yüzey alanına yol açmış vedaha iyi CO_2RR performansına katkı sunmuştur.

Ayrıca, uygulanan potansiyelin yeniden yapılanma sürecini önemli ölçüde katkı sunduğu gösterilmiştir. Bu sürecin yüzeydeki Cu/Zn oranını etkileyerek CO seçiciliğini değiştirebileceği bulunmuştur. CO_2RR sonrası aynı elektrot için hesaplanan Cu/Zn atomik oranının -0.8 V'ta -1.2 V'a göre daha yüksek olduğu vebunun da CO seçiciliği üzerindeki bulgularımızla uyuştuğu gözlemlenmiştir. Bu sonuçlar yüzeyde bulunan Cu'nun CO üretimindeki kritik rolünü vurgulamaktadır.

CO_2RR sonrası, yüzey kompozisyonunun önemli değişiklikler geçirdiği ve en yüksek Cu/Zn oranının mutlaka en yüksek ilk Cu miktarı ile ilişkili olmadığı da tespit edilmiştir. Bunun yerine, maksimum Cu/Zn oranı, aynı zamanda en yüksek FE değerine de sahip olan Cu_xO-250/ZnO elektrodunda gözlemlenmiştir. Bu varyasyonun yüzey yeniden yapılanma sürecine ve Cu /Zn atomları arasındaki galvanik etki ile ilgili olduğu düşünülmektedir. Her iki olgunun da de yüzey kompozisyonunu ve dolayısıyla elektrot seçiciliğini etkilediği tespit edilmiştir.

Sonuç olarak, bu tez, CO'ya karşı yüksek seçiciliğe sahip ucuz,yeryüzünde bol bulunan elementlerden tasarlanmış alternative bir elektrokatalizör olduğuna inanılan Cu-Zn elektrokatalizörlerinin CO_2RR sırasındaki dinamik davranışı ve yüzey kompozisyonu hakkında yeni bilgiler sunmaktadır. Bu bilgiler, daha etkili ve verimli Cu-Zn tabanlı elektrokatalizörler tasarlama hedefindeki gelecek çalışmalara önemli ölçüde katkıda bulunacağı düşünülmektedir.

AKNOWLEDGEMENTS

In the name of God, the Merciful, the Compassionate (بسم الله الرحمن الرحيم)

I would like to express my deepest gratitude to all those who supported and guided me in completing this thesis. I was fortunate to conduct my master's work at Koç University, where I was constantly surrounded by an enriching scientific environment that expanded my horizons.

Foremost, I would like to thank my advisor Dr. Sarp Kaya whose expertise, understanding and patience added a lot to my graduate experience. I stepped into his lab with limited research experience, and now I am departing with a heightened enthusiasm for solving complex scientific problems, thanks to his mentorship.

I am also deeply indebted to my co-advisor, Dr. Timuçin Balkan the principal investigator for this project, and first individual who taught me to laboratory skills. His understanding approach and consistent drive to encourage our development rather than passing judgment, played a crucial role in finalizing this thesis. His friendship and supportive attitude have always been a great source of motivation, making him feel like a caring brother than just a project. leader. I would also like to thank my group member Saeede Tafazoli, who substantially contributed to this project. She was always a role model in hardworking. Overall "CO_2 group was the best".

My committee members, Assoc. Prof. Uğur Ünal and Assist. Prof. Alp Yürüm deserve my heartfelt appreciation for their valuable feedback and interesting questions.

I want to express my gratitude towards all my lab members as well. The friendship we shared and the fun we had during this journey greatly enhanced my experience.

A special mention must go to my family. Their unwavering support and encouragement throughout this journey have been invaluable and a source of strength for me.

Finally, I would be remiss not to mention Asil foundation, their steadfast support has been like a beacon of light during my challenging journey abroad. We were not just a collective, but rather, we became a family united.

TABLE OF CONTENTS

List of Tables xi

List of Figures xii

Chapter 1: Introduction 1

1.1.The Electrochemical Reduction of CO_2 (CO_2RR) 2

1.1.1Thermodynamic of CO_2RR 3

1.1.2.Advantages of CO_2RR 4

1.1.3.Challenges of CO_2RR 5

1.2.CuZn electrocatalyst 6

1.3.CO_2RR to CO 7

1.3.1.CuZn as an electrocatalyst for CO 8

1.4.Scope and Objectives of the Study 9

Chapter 2: Experimental Methods 11

2.1. Synthesis Procedure 11

2.1.1. Electrodeposition 11

2.1.2. Atomic layer deposition (ALD) 13

2.2.Electrochemical Characterization 14

2.2.1.Electrocatalytic CO_2RR Performance Test Setup 14

2.2.2.Electrochemical Surface Area (ECSA) 16

2.2.3.Electrochemical Impedance Spectroscopy (EIS) 17

2.3 Structural and Morphological Characterization 18

2.3.1 X-ray Diffraction (XRD) 18

2.3.2.Feild Emission Scanning Electron Microscopy (FESEM) 18

2.3.3.Energy Dispersive Spectrometer (EDS) 19

2.3.4.X-ray Photoelectron Spectroscopy (XPS) 19

2.3.5. Raman Spectroscopy 20

Chapter 3: Modification of ZnO by Electrodeposited Cu_xO for Enhancing CO selectivity 22

3.1.Introduction 22

3.2.Experimental Methods 24

3.3.Results and Discussion 25

3.4.Conclusion 33

Chapter 4: Modification of ZnO by ALD Cu_xO for Enhancing CO Selectivity 34

4.1.Introduction 34

4.2.Experimental procedure 35

4.2.1.Electrochemical measurements: 35

4.2.2. Quantitative Analysis of ε and η Phases 36

4.3.Results and Discussion 36

4.4.Conclusion 45

Chapter 5: Summary and Conclusions 46

Chapter 6: Bibliography 48

Chapter 7: Appendix 57

Appendix A: Supporting Information for Modification of ZnO by Electrodeposited Cu_xO for Enhancing CO Selectivity. 57

Appendix B Supporting Information for Modification of ZnO by ALD Cu_xO for Enhancing CO Selectivity 62

LIST OF TABLES

Table 1.1. Electrochemical reduction of CO_2 products with standard potentials [22]. 4

Table A1.1. FE of liquid products obtained at 2 different potentials after 1 h of electrolysis in CO_2-saturated 0.1 M $KHCO_3$ analyzed by H-NMR……57

x

LIST OF FIGURES

Figure 1.1. Projected CO_2 emissions from 1990 to 2050, comparing scenarios with and without the implementation of mitigation strategies [12]. 2

Figure 1.2. Schematic illustration of CO2RR [19]. 3

Figure 1.3. Classification of monometallic electrocatalysts based in their selectivity [33]. 6

Figure 1.4. Classification of CO_2RR metals [10, 18] 7

Figure 1.5. Two possible routes of CO formation during CO_2RR [45]. 8

Figure 2.1. Schematic representation of electrodeposition cell [56]. 11

Figure 2.2. the potential difference with time during electrodeposition of ZnO. ... 12

Figure 2.3. As-prepared (a) Cu_xO-25/ZnO (b) Cu_xO-50/ZnO, and (c) Cu_xO-120/ZnO. 13

Figure 2.4. Illustration of ALD cycle with precursor A contains metal source B is the oxidant [59]. 14

Figure 2.5. Randles circuit model 17

Figure 2.6. Schematic representation of how (a) photoelectron and (b) Auger electrons are generated [67]. 20

Figure 2.7. Energy states of Raman spectra [69]. 21

Figure 3.1.FESEM images of (a) ZnO, (b) Cu_xO-25/ZnO, (c) Cu_xO-50/ZnO, and (d) Cu_xO-120/ZnO. (e) The atomic percent of Cu collected from EDS quantitative analysis. 25

Figure 3.2.(a) Raman spectra of as-prepared electrodes. (b) Zn 2p and (c) Cu 2p XPS spectra. 26

Figure 3.3. (a) FEs of electrocatalyst pre-reduced at -0.7 V for 30 min. The same electrodes were used at all potentials, each potential was applied for 30 mins sequentially. (b) Nyquist plots obtained at OCP for as-prepared electrodes in CO_2-saturated 0.1 M $KHCO_3$. 28

Figure 3.4. FESEM images of Cu_xO-50/ZnO (a) as-prepared, after 1h of CO_2RR at (b) -0.8 V and at (c) -1.2 V. FESEM images of ZnO (e) as-prepared, after 1h of CO_2RR at (f) -0.8 V and (g) -1.2 V. EDS quantitative analysis for as-prepared and tested (d) Cu_xO-50/ZnO, and (h) ZnO electrodes. 29

Figure 3.5. XRD reflections of (a) fresh Cu_xO-50/ZnO and ZnO. XRD reflections after -0.8 V and -1.2 V of (b) Cu_xO-50/ZnO, and (c) ZnO. 30

Figure 3.6. Double layer capacitance of Cu_xO-50/ZnO and ZnO after testing at (a) -0.8 V, and (b) -1.2 V in CO_2-saturated 0.1 M $KHCO_3$. Nyquist plots of Cu_xO-50/ZnO and ZnO at (c) -0.8 V, and (d) -1.2 V in CO_2-saturated 0.1 M $KHCO_3$. 31

Figure 3.7. The change in Cu/Zn ratio with increasing sputtering time. 32

Figure 4.1.FESEM images of as-prepared electrodes. (a) ZnO, (b) Cu_xO-100/ZnO, (c) Cu_xO-150/ZnO, (d) Cu_xO-250/ZnO, (e) Cu_xO-400/ZnO, and (f) Cu_xO-500/ZnO. .. 37

Figure 4.2. Raman spectra of as-prepared electrodes. 38

Figure 4.3. (a) C_{dl} of the as-prepared electrodes estimated from the changes in anodic and cathodic charging measurement at different potential scan rates. (b) Nyquist plots of as-prepared electrodes. Both performed in CO_2-saturated 0.1 M $KHCO_3$. 39

Figure 4.4. FEs of (a) gaseous products and, (b) liquid products at -0.8 V. 40

Figure 4.5. (a) Double layer capacitance of the electrodes, and (b) Nyquist plots employed at -0.8 V. Both measurements were implemented for CO_2RR tested electrodes at -0.8 V in CO_2-saturated 0.1 M $KHCO_3$. 42

Figure 4.6. FESEM images of electrodes after CO_2RR at -0.8 V for 1 h. (a) ZnO, (b) Cu_xO-100/ZnO, (c) Cu_xO-150/ZnO, (d) Cu_xO-250/ZnO, (e) Cu_xO-400/ZnO, and (f) Cu_xO-500/ZnO. 43

Figure 4.7. (a). Cu/Zn ratio obtained from XPS and EDS after CO_2RR at -0.8 V for 1 h. The quantification of the surface Cu/Zn ratio was performed by first normalizing the background of the spectra, followed by the integration of Zn $2p_{3/2}$ and Cu $2p_{3/2}$ XPS peaks. (b) The ratio of ε and η phases was calculated from Cu-Zn phase diagrams (Additional details pertaining to the calculation methods can be found in the Experimental section) 44

Figure A1.1. XPS spectra of as-prepared electrodes: (a) Cu LMM (b) O 1s……..57

Figure A1.2. ECSA-normalized J_{CO} of Cu_xO-50/ZnO and ZnO electrodes. 58

Figure A1. 3. Faradaic efficiency (FE) of the gaseous product of Cu_xO-50/ZnO electrode at -0.8 V, measured three times for consistency. 58

Figure A1.4. Elemental mapping obtained by FESEM-EDS of (a) fresh Cu_xO-50/ZnO, after 1 h electrolysis at (b) -0.8 V and (c) -1.2 V. 59

Figure A1.5. CV scans at different scan rates in CO_2-saturated 0.1 M $KHCO_3$ of (a) Cu_xO-50/ZnO after -0.8 V, and (b) after -1.2 V. ZnO electrode after (c) -0.8 V and (d) -1.2 V..... 59

Figure A1.6. XPS depth profile analysis of Cu_xO-50/ZnO after 1 h of electrolysis at -0.8 V (a) Zn $2p_{3/2}$ (b) Cu $2p_{3/2}$ (c) Cu LMM (d) O 1s..... 60

Figure A1.7. XPS depth profile analysis of Cu_xO-50/ZnO after 1 h of electrolysis at -1.2 V (a) Zn $2p_{3/2}$ (b) Cu $2p_{3/2}$ (c) Cu LMM (d) O 1s..... 61

Figure A1.8. The stability test of Cu_xO-50/ZnO at -0.8 V in 0.1 M $KHCO_3$..... 61

Figure B1.1. XPS spectra of as-prepared electrodes (a) Zn 2p (b) Cu 2p. 62

Figure B1.2. XPS spectra of as-prepared electrodes (a) Zn 2p (b) Cu 2p..... 62

Figure B1.3. FEs of gaseous products of the 6 electrodes, pre-reduced at -0.7 V for 30 min. The same electrodes were used at all potentials, each potential was applied for 30 mins sequentially. 63

Figure B1.4. FEs of gaseous products of the 6 electrodes, pre-reduced at -0.7 V for 30 min. The same electrodes were used at all potentials, each potential was applied for 30 mins sequentially. 63

Figure B1.5. (a) Partial current density of CO (J_{CO}) at five different potentials. (b). ECSA-normalized J_{CO} at -0.8 V estimated by dividing J_{CO} by C_{dl} found after -0.8 V.. 64

Figure B1.6. XRD reflections obtained after pre-reduction at -0.7 V for 30 min in 0.1 M $KHCO_3$. 65

Figure B1.7. (a) Zn concentration in the electrolyte after pre-reduction and CO_2RR at -0.8 V obtained from ICP. It's noteworthy that before initiating CO_2RR at -0.8 V, a pre-reduction step was carried out utilizing the same electrolyte. (b). represents the XRD reflection after pre-reduction step and CO_2RR at -0.8 V in 0.1 M $KHCO_3$ for Cu_xO-250/ZnO. 66

Figure B1.8. (a) Zn concentration in the electrolyte after pre-reduction and CO_2RR at -0.8 V obtained from ICP. It's noteworthy that before initiating CO_2RR at -0.8 V, a pre-reduction step was carried out utilizing the same electrolyte. (b). represents the XRD reflection after pre-reduction step and CO_2RR at -0.8 V in 0.1 M $KHCO_3$ for Cu_xO-250/ZnO. 66

Figure B1.9. (a) Zn 2p, (b) Cu 2p XPS spectra of the electrodes after CO_2RR at -0.8 V., recorded after 60 s of sputtering with Ar^+ at sputtering rate of 0.2 $nm.s^{-1}$. 67

Figure B1. 10. The equilibrium Cu-Zn binary phase diagram used for quantitative calculation of each phase [120] 67

Figure B1.11. Stability test of Cu_xO-250/ZnO at -0.8 V. The current density was maintained stable for more than 4 h. 68

Chapter 1:Introduction

For thousands of years, the rate of carbon dioxide (CO_2) production in the atmosphere was relatively balanced. This natural equilibrium was then disturbed by the industrial activity and the utilization of carbon-based fuels, leading to a rapid rise in the emission of CO_2[1]. Presently, the planet is witnessing a huge accumulation of CO_2 in the atmosphere, that has started from the early 1700's [2,3]. Between 1750 and 2021, the global concentration of CO_2 in the atmosphere has observed a significant increase from a 280 ppm to 415 ppm [4,5]. Figure 1.1 shows the estimated CO_2 emission levels up to 2050. It is evident that, unless serious actions are taken toward this issue, the CO_2 amount will surge into extremely high levels. This high CO_2 concentration and its severe implication cannot be overlooked, as it is accounting for 60% of the climate change.[6]. Therefore, an urgent and efficient solution must be found to mitigate climate change consequences. One of the proposed solutions is decarbonization, primarily shifting to energy sources that produce lower levels of greenhouse gases, like photovoltaics and wind turbines. However, these technologies come with limitations, including challenges related to electrical energy storage, scalability and versatility [7]. Moreover, energy use is not the sole contributor to CO_2 emission. A considerable portion of these emissions comes from the production of industrial products such as steel and cement, accounting about 12% of total CO_2 emission [8,9]. Thus, the reliance on decarbonized energy sources would surely mitigate and decrease climate change effects but will never solve the issue completely.

Carbon capture and storage (CCS) technology serves as another option that could possibly lower the high CO_2 emissions in the atmosphere. CCS essentially involves the process of capturing generated CO_2 and storing it in a location that ensures no environmental impact. The International Energy Agency (IEA) has set a target to decrease CO_2 emission by the year of 2035, and it is projected that 17% of the planned reduction will be achieved by utilizing CCS technology.[10]. Nonetheless, the high current cost of CCS technology, estimated at around 60 $ per ton of CO_2, presents a considerable barrier for the high scalability of the process. Thus, making the wide implementation of CCS both challenging and commercially unviable at present [11]

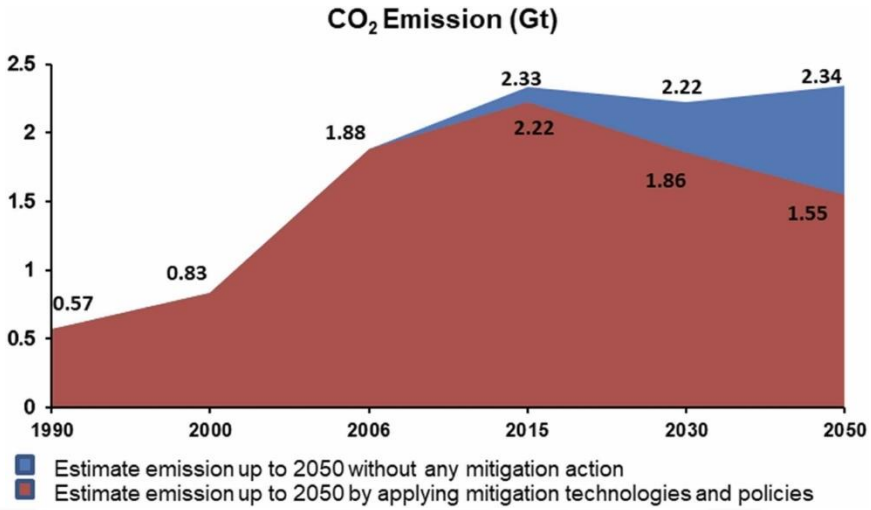

Figure 1.1. Projected CO_2 emissions from 1990 to 2050, comparing scenarios with and without the implementation of mitigation strategies [12].

Carbon recycling offers an innovative approach of reducing carbon emission in the atmosphere. One of the promising methods in this regard is converting CO_2 into chemicals and energy sources, which offers extensive market opportunities and substantial advantages [13]. A particular method in carbon recycling is CO_2 hydrogenation, which involves a thermal reaction between hydrogen and CO_2 to form other chemical products with lower oxidation state of carbon such as methanol, methane, formic acid etc. [13]. However, while being promising, the process of CO_2 hydrogenation still faces big obstacles that needs to be overcome. The procedure demands a large quantity of catalysts and requires a high temperature and pressure. Additionally, the process requires long time for the reaction, which limits its scalability and industrial application [14].

1.1.The Electrochemical Reduction of CO_2 (CO_2RR)

Other methods are under investigation and research for carbon recycling. These methods involves different strategies such as photoreduction of CO_2 (named as artificial photosynthesis) [15], photoelectrochemical [16], biochemical [17], radiochemical [18] and electrochemical reduction of CO_2 [8]. The electrochemical reduction of CO_2 (CO_2RR) has caught a significant attention of researchers worldwide. Figure 1.2 summarizes the carbon recycling process using CO_2RR. CO_2RR is a process that utilizes

electrical current to make an electrochemical reaction occurs. In the cathodic side, the carbon atom in CO_2 molecule is reduced from a high oxidation state of +4 to a lower oxidation one, while water undergoes oxidation and releases oxygen on the anode side. Both cathodic and anodic reactions are presented in the following equations in an alkaline condition.

$$CO_2 + xH_2O + ye^- = \text{product} + zOH^- \qquad \text{Cathodic reaction } (CO_2RR)\ (1.1)$$

$$2H_2O = O_2 + 4e^- + 4OH^- \qquad \text{Anodic reaction (OER) } (1.2)$$

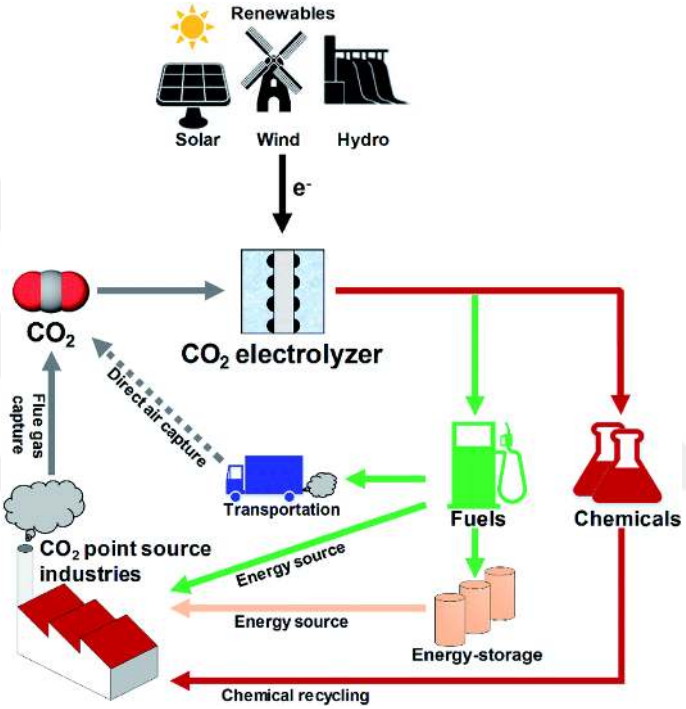

Figure 1.2. Schematic illustration of CO2RR [19].

1.1.1Thermodynamic of CO_2RR

CO_2RR is a thermodynamically favorable reaction at relatively low potentials. Table 1.1 shows the thermodynamic cell potential of the half redox reaction taking place in standard condition (1M reactants and products, 25°C, 1 atm pressure). Calculated from Gibbs energy formula shown below. However, in practical condition, CO_2RR requires typically higher potentials that the one indicated in Table 1.1. The reason behind this is that carbon dioxide is a highly stable molecule with 750 KJ of dissociation energy. This makes the chemical activation of carbon dioxide quite difficult [20]. Furthermore, CO_2RR consists

of multiple electron proton transfer steps and accompanied with slow reaction kinetics, therefore an overpotential is essential to be applied to fasten up these intermediate steps. and to run the reaction in acceptable rate [21]. Overall, to overcome CO_2RR barriers such as mass transport limitation, ohmic resistances and activation energies, a high overpotential needs to be applied.

$$\Delta G^{o} = -nFE^{o}_{rxn} \quad (1.3)$$

Table 1.1. Electrochemical reduction of CO_2 products with standard potentials [22].

Reaction	E° (V vs. SHE)	Product
$CO_{2(g)} + 2H_2O + 2e^- = HCOO^-_{(aq)} + OH^-$	-1.078	Formate
$CO_{2(g)} + 2H_2O + 2e^- = CO_{(g)} + 2OH^-$	-0.934	Carbon monoxide
$CO_{2(g)} + 2H_2O_{(l)} + 4e^- = C_{(s)} + 4OH^-$	-0.627	Graphite
$CO_{2(g)} + 5H_2O_{(l)} + 6e^- = CH_3OH_{(l)} + 6OH^-$	-0.812	Methanol
$CO_{2(g)} + 6H_2O_{(l)} + 8e^- = CH_{4(g)} + 8OH^-$	-0.659	Methane
$2CO_{2(g)} + 9H_2O_{(l)} + 12e^- = CH_3CH_2OH_{(l)} + 12OH^-$	-0.744	Ethanol
$2CO_{2(g)} + 8H_2O_{(l)} + 12e^- = CH_2CH_{2(g)} + 12OH^-$	-0.764	Ethylene

1.1.2.Advantages of CO_2RR

CO_2RR has numerous advantages that makes it more favorable than other pre-mentioned techniques. Notably, it does not require a high temperatures and pressures that are necessary of the hydrogenation process. Instead, CO_2RR can be conducted under atmospheric pressure and room temperature. Furthermore, the energy input required for CO_2RR is solely electrical current, which can be obtained from renewable energy sources. This makes CO_2RR to be a viable technique for energy storage that converts the electrical energy, harvested from photovoltaics and wind turbines into chemical products, which paves the way for more sustainable and less expensive than alternative than batteries.

Moreover, CO_2RR can result a various type of products depending on the nature of the catalyst and operating conditions. This feature allows us to synthesize complex products such as ethanol or propanol via a single step reaction. It is important to note that this feature can turn into a potential disadvantage if the catalyst produces a mixture of products that needs long and costly separation processes [23].

1.1.3.Challenges of CO_2RR

In order to scale up the CO_2RR process from a lab scale to industrial levels, several challenges have to be overcome. As discussed before, current CO_2RR catalysts requires a large overpotential to derive the reaction at the rate that is industrially acceptable. This energy barrier makes the process inefficient and remains an active area of investigation. Finding selective catalysts is another challenge that needs to be addressed. As noted earlier, CO_2RR can yield various type of products. Therefore, a highly selective catalyst must be utilized to avoid post-production separation processes. H_2 evolution reaction (HER) is another concern for CO_2RR. HER occurs at thermodynamical potential of 0 vs. RHE, which is close the thermodynamical potentials of CO_2RR products shown in Table 1.1. Therefore, the electrocatalysts should be designed in a way that inhibits the undesired competing HER, while promoting the production of the target product. In some cases, H_2 is a desirable product in specific ratios when syngas is the intended product. Overall, HER has to be controlled during CO_2RR to assure production of target product [24]. The third challenge relates to ensuring an adequate amount of CO_2 on the surface of the catalyst. Any limitation in mass transfer can decrease the reaction rate, and consequently reduce the efficiency of the process. Low solubility of CO_2 in aqueous electrolytes is the main cause for mass transfer limitation [11–14] and to solve this issue, researchers have thought about two distinct strategies. The first strategy is to directly send of CO_2 onto the catalyst surface, such as in case of gas diffusion electrodes (GDE) [29]. Alternative strategy is to increase the pressure of CO_2, as a higher pressure can drive more CO_2 into the electrolyte, mitigating the effect of mass-transport limitation [30]. Additionally, several research have been dedicated to find and optimize the electrolyte for CO_2RR. Different electrolytes were used to reduce the of mass transfer limitation and solve this issue [10,16-17].
Lastly, the stability of the electrocatalyst over adequate amount of time is a fundamental requirement for commercialization of CO_2RR. The catalyst needs to remain active and selective over prolonged periods to enable efficient and continuous operation of the process.

Addressing these challenges and trying to overcome them is crucial to move from laboratory-scale research to an industrial-scale and have a viable solution for climate energy.

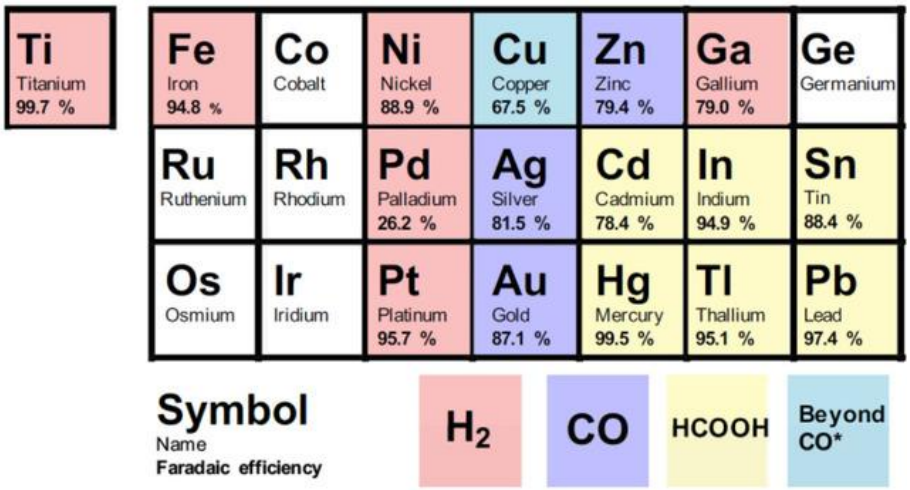

Figure 1.3. Classification of monometallic electrocatalysts based in their selectivity [33].

1.2.CuZn electrocatalyst

CO_2RR catalysts are generally classified according to their favored product. One pivotal study conducted in 1985 by Hori and his team [34]. They conducted CO_2RR in 0.5 M $KHCO_3$ under constant current 5 $mA.cm^{-2}$ and used polycrystalline mono-metals as electrocatalysts, which resulted in categorizing them into four primary groups as seen in Figure 1.3. Gold (Au) and silver (Ag), along with zinc (Zn), form a group of metals that are primarily selective towards CO. Another group, including titanium (Ti), iron (Fe), nickel (Ni), gallium (Ga), palladium (Pd), and platinum (Pt), is selective towards H_2, implying their intrinsic characteristic to reduce water rather than CO_2. Cadmium (Cd), indium (In), tin (Sn), mercury (Hg), thallium (Tl), and lead (Pb) makes the third group, displaying selectivity towards formate or formic acid (HCOOH). The fourth group comprises of only one metal which is copper (Cu). Cu stands apart as the only metal capable of moving beyond the pre-mentioned products. Its unique characteristic can be attributed to its adsorption energies with key intermediates as seen in Figure 1.4. Specifically, Cu is the only metal that has optimum binding energy toward adsorbed CO (CO*) and adsorbed H_2 (H*) neither weak nor strong binding. This distinct feature and optimum binding energies allows adsorbed H* and CO* to further react on the surface and forms hydrocarbon products [35].

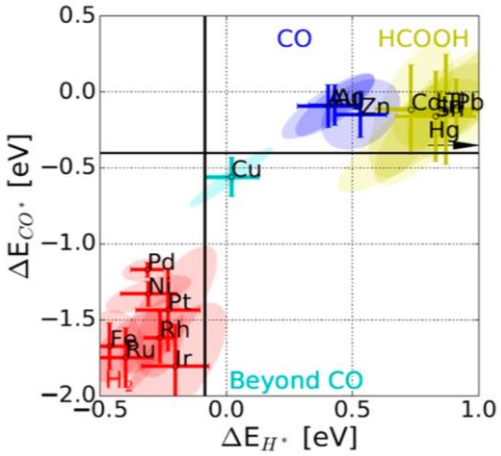

Figure 1.4. Classification of CO_2RR metals [10, 18]

1.3.CO_2RR to CO

Among all pre-mentioned possible products, CO and HCOOH are the only product that have high industrial feasibility. This is due to the fact that the FE of these products have reached superior values near 100% [35–37]. Additionally, CO is considered to be highly valuable feedstock in industry, as it is used in the famous Fischer-Tropsch process to synthesize CHO products [39]. CO is formed on the surface of catalyst by two possible routes that can be seen in Figure 1.5. The first route starts with the formation of COOH* intermediate by concerted proton electron transfer (CPET) process [39–41].The formed COOH* is then converted to form CO* and H_2O by another CPET process. Finally, CO* desorbs from the surface and forms gaseous CO. The other possible route differs by the formation of COOH*, where it forms by proton decoupled electron transfer process, where adsorbed CO_2* is reduced and protonated in two separated steps as seen in Figure 1.5. Optimizing the binding energy of COOH* is very crucial while designing CO forming catalyst. Previous studies indicated that the activity of the catalysts is directly related to COOH* binding energy[42–43].

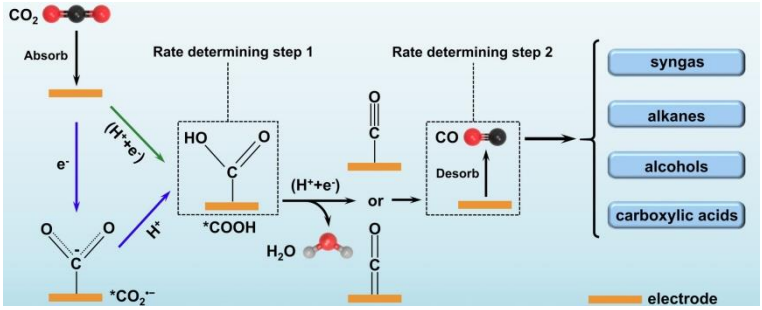

Figure 1.5. Two possible routes of CO formation during CO_2RR [45].

1.3.1.CuZn as an electrocatalyst for CO

While Zn is the sole earth-abundant metal among those monometallic metals selective towards CO, it demonstrates lower selectivity and activity than both Ag and Au. To boost Zn's catalytic performance, addition of another element has been proposed, and Cu emerges as a promising candidate. Cu owes an optimal binding energy to CO* and has a high charge transfer capacity that can boost the activity and selectivity of Zn [46]. Furthermore, Cu possesses a relatively low market price, making it more financially feasible compared to other costly alternatives [47]. Several research have used Cu-Zn electrocatalysts for CO_2RR. When Zn ratio is higher than Cu, the catalyst tends to be selective toward CO. Several researchers have noticed a marked increase in CO selectivity by addition of Cu, with various reasons proposed for this improvement. For instance, Wang et al used a galvanic replacement procedure on a Zn foil to prepare a Cu-Zn catalyst. They observed that the Cu-Zn catalyst surpassed the selectivity of both Zn and Cu foils, achieving a Faradaic efficiency (FE) for CO of about 95% at -1.0 V vs. RHE. This was attributed to the stabilization of the carboxyl intermediate (COOH*) [48]. In contrast, Lue et al prepared two different Cu-Zn catalysts: a core-shell and a phase-separated one. They found that the phase-separated Cu-Zn catalyst demonstrated superior selectivity towards CO, reaching 94% at -1.0 V vs. RHE [49]. TEM results showed a formation of Zn layer on the surface of the core-shell catalyst after CO_2RR. This demonstrates that the catalyst underwent reconstruction process and attributed the lower catalytic activity of core-shell catalyst to the absence of Cu on the interface.

Moreover, Xue and his colleagues reported that Cu-decorated ZnO nanosheets, synthesized via a wet chemistry approach, exhibited a high catalytic performance towards

CO. By combining is-situ IR spectroscopy , quasi in-situ measurements and DFT calculation., they found that Cu decoration had reduced the angle of Zn-O, created more surface defects and improved the physisorption and chemisorption of CO_2. They further hypothesized that the presence of Cu decreased the energy barrier from CO_2* to COOH* while promoting the formation of COOH* [46]. Additionally, Wang et al observed that Cu-doped ZnO yielded an FE for CO higher than 80%. With the help of theoretical calculation and in-situ measurement, they posited that Cu atoms stabilize neighboring oxygen vacancies and tune the local electronic structure. This resulted in an increase in the number of active sites, enhanced electrical conductivity, and a lowered barrier for CO formation [50]. In conclusion, the use of Cu-Zn based catalysts for CO_2RR to CO has shown impressive results. This motivated researchers to investigate more on this type of catalysts, given its appealing low cost and plentiful availability, which reinforces their potential for commercial utilization.

Other reports observe an increase in different products selectivity while using Cu-Zn catalyst. Mainly, when Cu amount is high enough, the catalyst starts to form other products beyond HCOOH and CO, such as methane, ethylene and ethanol [50–53]. However, given the concentration of this thesis on the conversion of CO_2 to CO, an in-depth exploration of these alternate products is beyond its scope. For a more comprehensive understanding, the reader is directed to two pertinent review articles [10, 24].

1.4.Scope and Objectives of the Study

This study is conducted to understand the effect of Cu_xO addition on the selectivity of ZnO nanorods. As explained above, Zn is a metal that belongs to the CO-selective group, but its low selectivity and activity limit its use on a large scale. The addition of Cu_xO is intended to enhance CO selectivity and activity due to having an optimum binding energy to reaction intermediates. However, more in-depth understanding of oxide-derived Cu-Zn electrocatalysts is still required due to the dynamic behavior of the surface and the galvanic effect between Cu and Zn. In this study, we showed that the addition of Cu_xO improved the FE of CO. Several compositional, structural, and physical characterizations were implemented to understand the origin of the enhancement. The addition of Cu_xO was shown to have a significant effect on the reconstruction process of the surface,

resulting in a higher surface area of the electrode. Furthermore, we showed that a new active phase, ε-$CuZn_4$, formed after the pre-reduction step and CO_2RR. The addition of Cu_xO further improved the charge transfer resistance (R_{ct}) of the electrodes, which results in faster charge transfer and hence, enhanced CO_2RR performance.

In Chapter 2, the experimental procedure of electrocatalyst synthesis, CO_2RR performance testing, and structural and compositional characterizations are explained.

In Chapter 3, we examined the first set of synthesized electrocatalyst, ZnO nanorod with different amount of Cu_xO nanoparticles, both layers synthesized using electrodeposition methods. We further proved that the applied potential affects the compositional characteristics of the surface, where high CO was observed when the Cu/Zn ratio was higher on the surface.

In Chapter 4, we examined the second set of Cu_xO-ZnO, where Cu_xO was added using advanced atomic layer deposition (ALD) technique. The addition of Cu_xO using ALD showed a more significant improvement in CO selectivity than electrodeposited Cu_xO. Furthermore, ALD Cu_xO showed a greater improvement in reducing R_{ct} and increasing the surface area. Different amounts of Cu_xO were deposited on the surface. We showed that the initial amount of Cu_xO doesn't necessarily reflect the compositional characteristics of the surface. As XPS results suggest, Cu_xO-250/ZnO showed the highest Cu/Zn ratio on the surface, while Cu_xO-400/ZnO and Cu_xO-500/ZnO showed a lower amount of Cu on the surface. This result aligns with the FE of CO, further proving the importance of the presence of Cu on the surface for having high selectivity to CO.

Chapter 2:Experimental Methods

2.1. Synthesis Procedure

2.1.1. Electrodeposition

Electrochemical synthesis is a well-known deposition technique, operates on the principle of electrochemical reduction or oxidation, where an electric current or potential difference is applied between two conductive electrodes that are separated by an electrolyte. In this process, the substrate (cathode) and the counter electrode (anode), which is generally graphite or platinum electrode are immersed into an electrolyte that contains the source of metal ions. The applied potential or current reduces the metal ions and forming metal atoms that adheres and crystallize on the surface. The morphology, thickness, and composition of the deposited layer can be carefully controlled by adjusting the process parameters, such as applied potential or current density, deposition time, the composition of the electrolyte, the distance between the two electrodes etc.

Electrodeposition holds a distinct edge over alternative deposition techniques, due to its simplicity and cost-effectiveness, as it does not require expensive or complex instruments and operates at ambient pressure and temperature. Several materials, compositions and morphologies can be obtained using electrodeposition by simply adjusting parameters including potential, temperature, and pH. Furthermore, Electrodeposition stands out due to its suitability for large-scale deposits which make it a suitable technique for industrial applications.

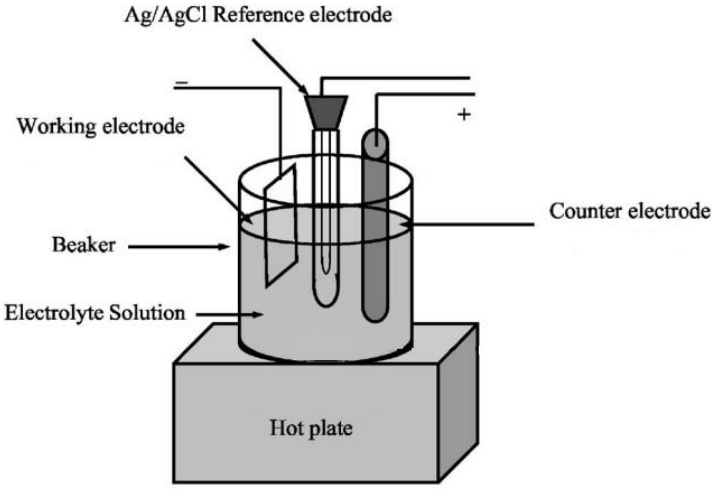

Figure 2.1. Schematic representation of electrodeposition cell [56].

2.1.1.1. Electrodeposition of ZnO

Electrodeposition of zinc oxide nanorods (ZnO) were prepared using the recipe shown in previous report [57] with slight modifications. Zn foils (substrate) were first cleaned in absolute C_2H_5OH and then with ultrapure water in an ultrasonic bath for 10 mins each, followed by drying with a lab tissue to avoid rapid oxidation. Electrodeposition of ZnO nanorods was then implemented in an aqueous solution, which includes 5 mM $Zn(NO_3)_2 \cdot 6H_2O$ and 5 mM HMT. Constant current -0.25 $mA.cm^{-2}$ was applied for 1 h at 75 °C. Ag/AgCl and platinum (Pt) electrodes were used as reference and counter electrodes, respectively. The electrodes prepared were then rinsed with water and dried in an oven for 6 h. Figure 2.2 shows the potential difference versus time during the electrochemical deposition of ZnO nanorods. The obtained electrode was homogenously coated with white ZnO layer as depicted in Figure 2.2.

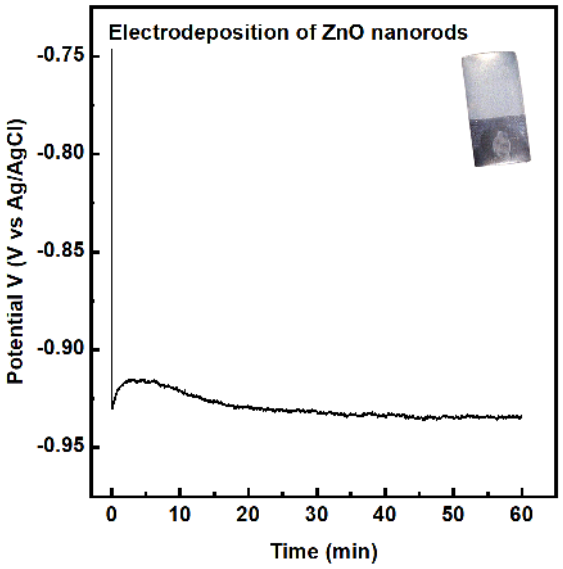

Figure 2.2. the potential difference with time during electrodeposition of ZnO.

2.1.1.2. Electrodeposition of Cu_xO

For Cu_xO/ZnO electrocatalysts, similar recipe reported by Ren et al was used with slight modification [57]. 0.4 M $CuSO_4.5H_2O$ and 3 M $C_3H_6O_3$ aqueous solution were used as an electrolyte for Cu_xO deposition. 5 M NaOH was used to adjust the pH of the electrolyte to 11.5. For the electrodeposition of Cu_xO, constant current (-0.9 $mA.cm^{-2}$) was applied for 25, 50, and 120 s at 45 °C, followed by similar cleaning and drying steps

as in the ZnO electrode. Cu_xO/ZnO electrocatalysts were named as Cu_xO-25/ZnO, Cu_xO-50/ZnO, and Cu_xO-120/ZnO according to Cu_xO deposition time.

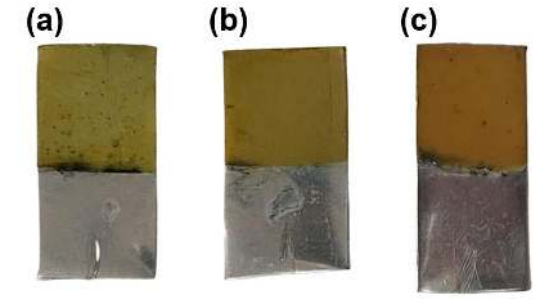

Figure 2.3. As-prepared (a) Cu_xO-25/ZnO (b) Cu_xO-50/ZnO, and (c) Cu_xO-120/ZnO.

2.1.2. Atomic layer deposition (ALD)

Atomic layer deposition (ALD) is a deposition technique belongs to chemical vapor deposition (CVD) family, that is typically used for thin film deposition. ALD provides high uniformity and control over thickness with the ability of having single atomic layer deposition thickness. ALD starts with first pumping the reaction chamber, where then a precursor A is pulsed into reaction chamber and chemisorbs to the surface. Then the precursor A is removed by purging the camber with an inert gas. The chamber is evacuated again and precursor B which is typical an oxidant such as water (H_2O), Oxygen(O_2) or ozone (O_3) is pulsed into the chamber. The oxidant reacts with precursor A where the desired thin film is formed. The unreacted oxidants species are then removed by similar purging with an inert gas. This entire cycle is then repeated several times depending on the desired deposit thickness[57-58] .

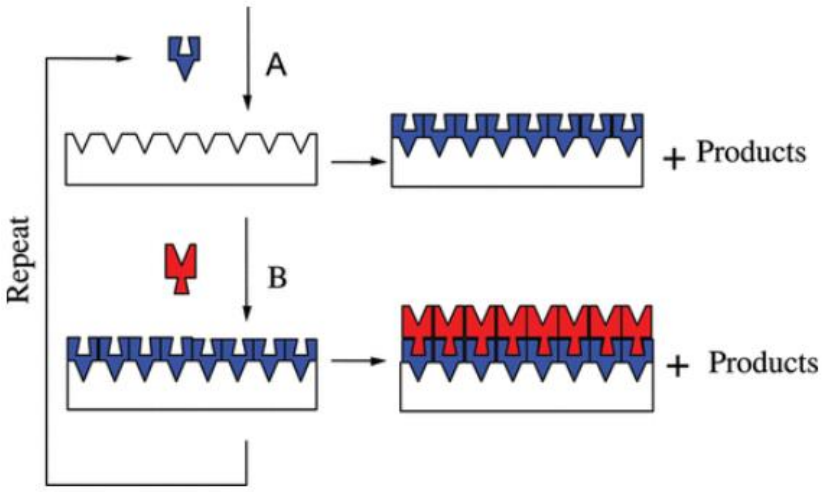

Figure 2.4. Illustration of ALD cycle with precursor A contains metal source B is the oxidant [59].

2.1.2.1. ALD of Cu_xO

ALD Cu_xO/ZnO electrocatalysts were fabricated by depositing Cu_xO using ALD. Water functioned as an oxidant where copper(II) hexafluoroacetylacetonate ($Cu(hfac)_2$) was used as a copper source. The substrate holder was heated to 280°C, while the precursor holder was maintained at 75°C. ZnO electrodes were added to the chamber and kept for 5 minutes for heating prior to pulsing. Precursor was then pulsed for 1 second, held in the chamber for 5 seconds before being removed by the pump. Water is then pulsed for 3 seconds and held for 5 seconds. $Cu(hfac)_2$ and water were pulsed subsequently 100, 150, 250, 400, and 500 times, where the electrodes are named based on the cycle number (e.g., Cu_xO-100/ZnO, Cu_xO-150/ZnO, etc.).

2.2.Electrochemical Characterization

2.2.1.Electrocatalytic CO_2RR Performance Test Setup

Electrocatalytic CO_2RR performance tests were conducted in H-cell of a 35 mL capacity of each compartment. The anode and the cathode were separated by a Nafion 212 membrane. Ag/AgCl and Pt were used as reference and counter electrodes, respectively. 0.1 M $KHCO_3$ was used as an electrolyte and purged with CO_2 for 30 mins prior to the tests and continuously supplied to each compartment at 8.8 sccm using a digital flowmeter.

2.2.1.1.Gas Chromatography (GC)

Gas chromatography (GC) is a widely used technique for analyzing and quantifying a mixture of gases. The analysis starts with injecting the sample into GC. The sample is then transported by a carrier gas into a column, where it passes through a stationary phase. Each gas molecules interacts differently with the stationary phase, causing the gaseous molecules to exist the column at the different elution times depending on the interaction strength. More specifically, the gas molecules that have a weak interaction with the stationary phase does not absorb for a long period of time and will exist the column quicker and the converse holds true for those with a stronger interaction[60].

After the gas separation, the eluted gas molecules pass through two different detectors TCD and FID. In TCD, the eluted compound enters the detector. The difference in thermal conductivity between a pure carrier gas (reference) and the eluted gas is then measured. The conductivity difference indicates the concentration of eluted gas in the sample.

In FID, the eluted gas is injected into hydrogen air-flame. This causes the organic elute gas to break down into cations and electrons that would result in a creation of a current between two collector electrodes. The current is then measured, which gives information about concentrations of the eluted organic gas in the sample [60].

For gaseous product analysis, a 7820A Agilent gas chromatograph (GC) equipped with a thermal conductivity detector (TCD) and flame ionization detector (FID) was used.

2.2.1.2.Hydrogen Nuclear Magnetic Resonance (H-NMR)

Hydrogen nuclear magnetic resonance (H-NMR) is a powerful analytical technique that is used for several purposes including chemical identification of molecules. H-NMR relies on the magnetic properties of hydrogen atoms in the molecules. When the sample with hydrogen containing-molecules is placed in a strong, uniform magnetic field, the hydrogen nuclei (protons) align either with or against the direction of the magnetic field. The protons are then exposed to a radio frequency pulse that causes the protons to switch from low energy state to high energy state. Upon the removal of the radio frequency, the protons are back to the low energy state and releases the energy in form of radiofrequency (resonant frequency) that is measured by a receiver coil. The energy released upon the removal of the radiofrequency gives information about the chemical environment of the protons, which allows us to understand and quantify several proton-containing molecules such as formic acid, ethanol, and acetate [61].

2.2.1.3.Faradic Efficiency (FE) Calculation

For calculating FE of gaseous products, standard gas mixture with known composition was used for calibration, and the below formulas were used for calculations:

$$FE_{gas\ (x)} = \frac{n_x \times n_e \times F}{Q_{total}}$$

$$n_{x\ flow} = C_x \times n\ (V_{total})$$

$$C_x = \left(\frac{\text{Peak area of gas x obtained during } CO_2RR}{\text{Peak area of gas x obtained from standard gas measurement}}\right) \times (\text{Volumetric \% of gas x in the standard mix gas})$$

$$n(V_{total}) = \frac{\text{Duration of experiment (min)} \times \text{Flow rate of gas (sccm)}}{22400}$$

F represent Faraday constant whereas, n_x represents the number of moles of gas x being sent to GC. C_x represents the volumetric percentage of gas x present in the sample. The total number of moles of gas being sent to GC is represented by $n(V_{total})$. n_e shows the number of electrons that are transferred for the reduction of product x.

$$FE_{liquid\ (x)} = \frac{V_{electrolyte} \times C_x \times n_e \times F}{Q_{total}}$$

$V_{electrolyte}$ is the volume of the electrolyte used during CO_2RR (L). C_x is the concentration of the product x obtained from H-NMR ($mol.L^{-1}$), and n_e shows the number of electrons that are transferred for the reduction of product x.

2.2.2.Electrochemical Surface Area (ECSA)

Cyclic voltammetry (CV) is popular electroanalytical technique used to study the electrochemical properties of a material in solution, where a potential sweep is applied between two distinct potentials. The current is measured during the sweep to provide information about redox reaction taking place between the two potentials. In this study, CV scans were implemented for measuring electrochemical surface area (ECSA) of the electrodes. The CV scans must be applied in a non-faradic region that is no redox reaction takes place on the selected range. Different scan rates are required to be applied to determine the double layer capacitance. The obtained capacitance current is proportional to ECSA values [62].

In this study, we calculated the difference between the anodic and cathodic currents and then divided the result by two for each scan rate. Finally, we plotted the scan rate versus

this difference and determined the slope of the resulting line, representing the double-layer capacitance (Cdl) of our electrocatalysts. More details about scan rates and potential range are given in experimental part in chapter 3 and 4.

2.2.3.Electrochemical Impedance Spectroscopy (EIS)

Electrochemical impedance spectroscopy is a powerful technique used to investigate electrochemical characteristics of an electrode such as charge transfer resistance (R_{ct}),solution resistance (R_s), double layer capacitance (C_{dl}), etc. In EIS measurement, a small amplitude sinusoidal voltage or current is applied and the response current and voltage is measured. As a result of the test, Nyquist plot is typically obtained which represents imaginary and real resistance of the system at different frequency values.

Different frequencies are applied in order to separate different processes that might take place at the electrode-electrolyte interface at different frequencies such as electron transfer, diffusion, adsorption or desorption of species. Randles circuit is the selected model to represents the obtained Nyquist plots as shown in Figure 2.5. R_s often called the solution or ohmic resistance coming from the electrolyte, connection wires and the used cell. R_{ct}, is the charge transfer resistance where the lower R_{ct} value is, the faster the reaction rate [63]. CPE stands for constant phase element which represents non-ideal capacitor due to roughness, porosity and other irregularities on the surface of the electrode.

In this study, EIS measurements were performed in the H-cell in CO_2-saturated 0.1 M $KHCO_3$ electrolyte solution. All measurements were implemented in a frequency range from 0.01 Hz to 100,000 Hz. Difference potentials were applied depending on the type of the measurement which is specified in the experimental section in chapter 3 and 4.

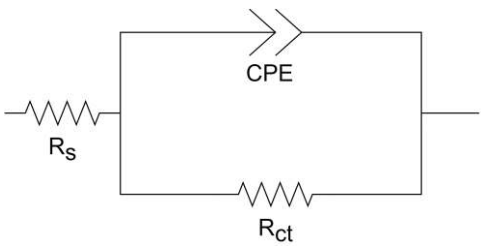

Figure 2.5. Randles circuit model

2.3 Structural and Morphological Characterization

2.3.1 X-ray Diffraction (XRD)

X-ray diffraction (XRD) is a wild known non-destructive characterization technique that is used for phase identification, where each crystalline material has characteristic XRD pattern. In XRD experiment, X-ray is generated by a cathode ray tube which is generally made of Cu. The emitted X-ray is then filtered to have monochromatic radiation and directed toward the target material. When the x-ray enters lattice planes, it gets diffracted according to Bragg's law that is shown in the formula below. The sample is scanned in a range of 2θ to effectively probe different planes of atoms. From XRD pattern, different information can be obtained such as formation or losing of crystalline phases, crystallographic orientation, crystallite size and size distribution, impurities etc [64]. In this study, the crystal structure was analyzed through X-ray diffraction (XRD) using a D2 Bruker phaser with Cu Kα radiation as the X-ray source (30 kV, 10 mA).

$$n\lambda=2d \sin \theta$$

2.3.2.Feild Emission Scanning Electron Microscopy (FESEM)

Field emission scanning electron microscopy (FESEM) is an important microscope technique that is used for obtaining images of the surface morphology and topography. In principle, a high energy electron beam emitted from field emission source is focused on the sample. The sample interacts with the electron beam, generating a signal that is collected and translated into a detailed image. More specifically, when the incident beam hits the surface of the sample, the low energy electrons on the surface of the sample are ejected, which is known as secondary electrons. These electrons are collected by a detector and analyzed according to it intensity. Back scattered electrons (BSE) are another way for getting information of the material, where the incident beam scatters back and collected by a specific detector. BSE images are usually good for compositional contrast and identification of different phases, while SE images are better for morphological and topological analysis as the image gives more surface details. The use of FESEM provide smaller and more coherent beam of electrons with results in better and brighter resolution than conventional SEM [65].

In this study, Field emission scanning electron microscopy (FESEM) images were measured by Zeiss Ultra Plus Field Emission Scanning Microscope equipped with an energy-dispersive spectrometer (EDS).

2.3.3.Energy Dispersive Spectrometer (EDS)

Energy dispersive spectrometer (EDS) is an analytical technique that is used for elemental compositional characterization of materials. In EDS, the surface of the specimen is bombarded with high energy electrons. When these electrons hit an atom in the specimen, an inner shell electron gets ejected, leaving a vacancy that is later filled with an outer shell electron. The energy difference between the outer and inner shells is emitted in a form of X-ray. The emitted x-ray is characteristic of their originating elements, where each element has a distinct x-ray. This X-ray is then collected by a detector and analyzed, giving a quantitative elemental characterization of the specimen [65].

2.3.4.X-ray Photoelectron Spectroscopy (XPS)

X-ray photoelectron spectroscopy is a surface sensitive spectroscopy technique that is widely used to identify the surface composition and electronic structure of a material. The fundamental of XPS involves the interaction between incident x-ray beam with the surface of the specimen. The photoelectron effect results in an ejection of electron from core level as shown in Figure 2.6. The ejected photoelectrons are emitted with a kinetic energy that is defined by the equation shown below, where hν represents the energy of the incident X-ray, BE is the binding energy of the electron in its original orbital, Φ_{XPS} is the work function of the spectrometer, and KE is the kinetic energy of the photoelectron [66].

$$BE = h\nu - (KE + \Phi_{XPS})$$

After the ejection of core-level electron (photoelectron), another electron moves from outer shell to the core shell to fill the vacancy. The energy difference between the two levels is transferred to a second outer shell electron that causes that electron to be ejected known as Auger electron. The energy of this electron is then measured and gives characteristics of the atom. Overall, XPS technique is considered to be surface sensitive

technique, giving an information about topmost surface only due to the mean free path of these electrons. Typically, photoelectrons have a mean free path of around 1-10 nm while Auger possesses even shorter mean free path due to lower kinetic energy [66]. In this study, XPS measurements were performed on a Thermo K-alpha laboratory XPS system with a monochromatized Al K-alpha X-ray source.

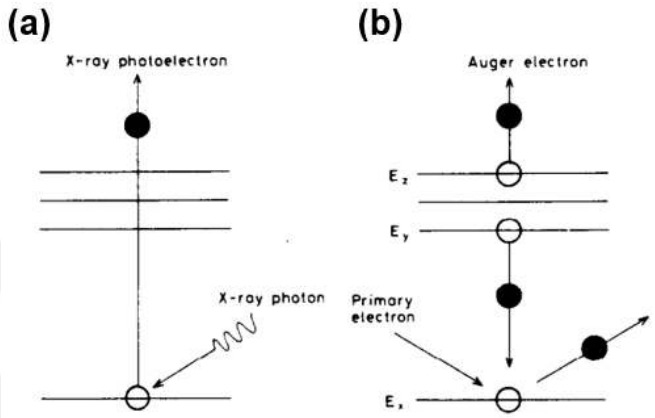

Figure 2.6. Schematic representation of how (a) photoelectron and (b) Auger electrons are generated [67].

2.3.5. Raman Spectroscopy

Raman spectroscopy is non-destructive characterization technique that gives information about molecular composition, structural characteristics, and chemical environment of a specimen. The principle of Raman spectroscopy starts with illuminating the specimen with monochromatic light which is typically a laser. The laser interacts with the specimen, where most of the incident light is elastically scattered known as Rayleigh scattering. At the same time, a very small amount of the incident light (1 in 10^6-10^8 elastic scattering) is scattered inelastically known as Raman scattering [67-68]. The resultant of laser-matter interaction can be seen in Figure 2.7

The inelastic scattering causes energy exchange between the incident light and the specimen molecules, where they change their vibrational or rotational state to either higher or low energy states. In case of higher energy state transition, the molecules absorb energy from the incident light, and hence, scatters with lower energy known as Stocks Raman scattering. Meanwhile, in case of lower energy state transition, the molecules emit energy, which causes incident light to scatter with higher energy known as Anti-Stokes

Raman scattering. Raman scattering gives information about energy difference between incident light and the scattered photons that corresponds to energy of the rotational or vibrations transitions of molecules. Each molecule has a characteristic Raman spectrum due to unique energy level and this technique offers a powerful identification of different molecules and any changes in their energy levels. In this study, Raman spectra were generated by Renishaw Invia Raman Microscope with 633 nm excitation laser

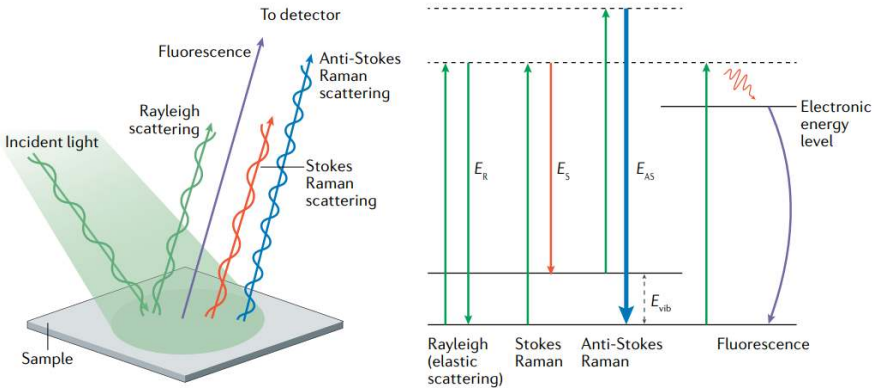

Figure 2.7. Energy states of Raman spectra [69].

Chapter 3: Modification of ZnO by Electrodeposited Cu_xO for Enhancing CO selectivity

3.1.Introduction

Carbon dioxide (CO_2) is a greenhouse gas that is released into the atmosphere through human activities such as burning fossil fuels and deforestation. These emissions contribute to climate change and have catastrophic consequences for the environment [69 -70]. This issue causes serious global concern and calls for an urgent solution. Many technologies have been implemented to reduce CO_2 amount in the air, including CO_2 capturing [72], thermochemical [73], biochemical [74], photochemical [75], photoelectrochemical, and electrochemical conversion of CO_2 [76]. Among all, electrochemical reduction of CO_2 (CO_2RR) drew significant attention [35] due to several advantages over other processes, such that it can be performed at room temperature and ambient pressure while thermochemical conversion needs high temperature and pressure conditions. Moreover, electrochemical CO_2RR is performed using electrochemical principles where the only source of energy needed is electricity that can be harvested from renewable sources such as solar cells or wind turbines [45], [77].

Different products varying from C_1 [78], C_2 to even C_3 [78-79] can be produced via electrochemical CO_2RR. The activity and selectivity are affected by several parameters, including the nature of the electrocatalyst, applied potential, pH, type of electrolyte, etc. [77]. Thermodynamically, CO_2 can be reduced to the pre-mentioned products by proton-coupled multielectron transfer steps at low potential [24]. However, CO_2RR has kinetic limitations so it requires high overpotential and consequently lowers the energy efficiency of the process [77]. Meanwhile, the hydrogen (H_2) evolution reaction (HER) is a competing reaction that takes place at similar electrode potentials. Therefore, the electrocatalyst should be designed in a way to lower overpotential while suppressing HER [81]. Syngas (a mixture of carbon monoxide (CO) and H_2) with a high (CO/H_2) ratio is an important raw material for many industrial processes, mainly for Fischer-Tropsch (F-T) process [82].

In CO_2RR, CO is formed on the surface of the electrocatalyst by two possible routes. CO_2 is firstly adsorbed on the surface ($*CO_2$), and one electron is transferred to $*CO_2$

resulting in a carboxylate anion (CO_2^-). Then $*CO_2^-$ gets protonated and converts to carboxyl (COOH). *COOH is then further reduced to *CO and H_2O molecules by a concerted proton-electron transfer (CPET) process, and finally, *CO desorbs from the surface to form gaseous CO. The second possible route differs in terms of *COOH formation, where it is directly formed by the CPET process, which then undergoes another CPET as the first route [24], [81]. It is suggested that the rate-determining steps (RDS) in the second route of the CO formation are COOH* formation and CO* desorption [45]. Therefore, high activity and selectivity toward CO can be achieved by overcoming the kinetic bottleneck in these steps.

First route

$$CO_{2(g)} + * + e^- \rightarrow *CO_2^-$$

$$*CO_2^- + H^+_{(aq)} \rightarrow *COOH$$

$$*COOH + H^+_{(aq)} + e^- \rightarrow *CO + H_2O$$

$$*CO \rightarrow * + CO_{(g)}$$

Second route

$$CO_{2(g)} + * + H^+_{(aq)} + e^- \rightarrow *COOH$$

$$*COOH + H^+_{(aq)} + e^- \rightarrow *CO + H_2O$$

$$*CO \rightarrow * + CO_{(g)}$$

To date, the most common metal electrocatalysts in CO_2RR toward CO are silver (Ag) and gold (Au), as they have high activity and selectivity [83], [84]. However, both metals are rare and expensive, opening the door for the investigation of more abundant and cost-effective alternatives. Zinc (Zn) is the only earth-abundant non-precious metal that is among CO-selective metals [35]. However, bulk Zn metal suffers from lower selectivity and activity, where many attempts were implemented to boost their performance. For example, nanostructured Zn, such as nanoparticles, porous, and dendritic structures, have been widely studied, as they showed high faradaic efficiency (FE) of CO >70% due to increased surface area and hence, new active sites [85]–[87]. Another way to enhance the selectivity of Zn is by using oxide-derived Zn, where they showed better activity than metallic Zn. These enhancements were attributed to the

introduction of new active sites. However, the chemical nature of those sites (oxide species (O^{2-}), edges, or O vacancies) are still debated [87–91].

Bimetallic or oxide-derived Zn-Cu electrocatalysts are promising candidates for CO_2RR as Cu is a cost-effective metal with moderate binding energy to CO that can optimize the binding energies of Zn-CO and other crucial intermediates [48]. Previous studies showed that if the Cu amount is higher than Zn on the surface, the electrocatalyst is more likely to produce hydrocarbons and formate ($HCOO^-$), while if Zn is in a higher fraction, it is more likely to produce CO [47], [48], [88], [92–94]. The improvement in CO selectivity in previous studies was attributed to different reasons, such as (i) weakening the adjacent Zn-O bond induced by Cu, which increases the number of active sites for CO_2 adsorption [95], (ii) the electronic effect of Cu adatoms on Zn surface [48], and (iii) optimization of the binding energy of key intermediates such as *COOH and *CO [49], [93].

Herein, we report electrodeposited ZnO nanorods modified with Cu_2O nanocubes that are more active and selective toward CO formation than pristine ZnO nanorods. We attribute the improvement to the enlarged electrochemical surface area, lower charge transfer resistance (R_{ct}), and alloy formation, which are supported by electrochemical surface area (ECSA), electrochemical impedance spectroscopy (EIS), and X-ray diffraction (XRD) measurements, respectively. X-ray photoelectron spectroscopy (XPS) depth profile analysis suggests that at -0.8 V (vs. RHE) at which CO selectivity is higher, the Cu/Zn content on the surface was found to be higher than that at -1.2 V. This finding shows that the optimum amount of Cu/Zn ratio is required for high selectivity toward CO. In addition to this, our electrocatalyst showed high stability (more than 4 h) and therefore, we believe that our study will help in the process of designing cost-effective commercial electrocatalyst for CO_2RR to CO.

3.2.Experimental Methods

The Cu_xO-ZnO electrocatalyst were synthesized and characterized as described in chapter 2. ECSA measurements were carried out in a CO_2 saturated 0.1 M $KHCO_3$ electrolyte solution using cyclic voltammetry (CV) scans at 5 different scan rates: 20, 40, 60, 80, and 100 $mV.s^{-1}$. The potential range was selected in a non-faradic region between -0.5 and -0.6 V.

3.3.Results and Discussion

Figure 3.1a-d shows as-prepared electrodes examined by FESEM. The ZnO electrode shows a homogeneous distribution of ZnO nanorods on the substrate with an average diameter of ~45 nm. The nanorods are compact, with small gaps between the rods. Meanwhile, Cu_xO/ZnO electrodes show that Cu_2O deposition takes place primarily between ZnO nanorods. This suggests that the deposition starts from the substrate and grows and reaches the tip of the nanorods, as in Cu_xO-25/ZnO and Cu_xO-50/ZnO. When deposition time is long enough, Cu_2O particles grow and settle on top of the nanorods, which is observed in the Cu_xO-120/ZnO electrode. Figure 3.1e shows the changes in the Cu amount with increasing deposition time. The atomic fraction of Cu increases linearly with deposition time, with the amount of Cu ranging from 3 to 16% for Cu_xO-25/ZnO and Cu_xO-120/ZnO, respectively. It is expected from the EDS result that, since Zn is the predominant metal on the surface, the electrocatalysts are more likely to be selective toward CO, as demonstrated in the next section.

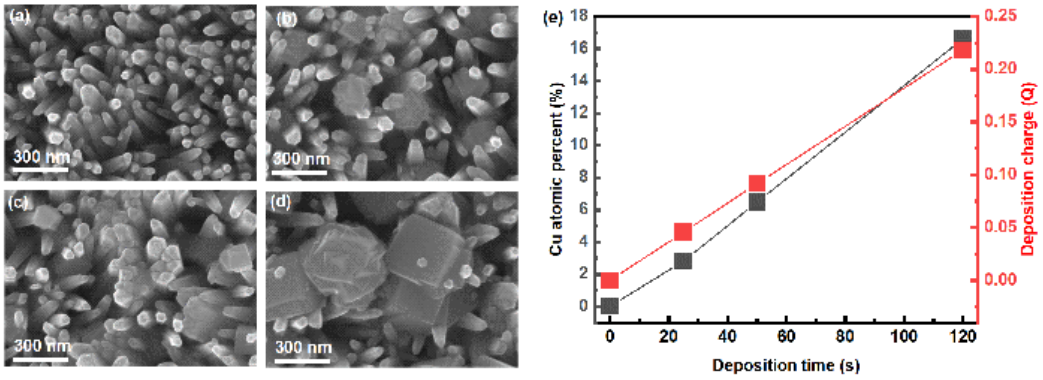

Figure 3.1.FESEM images of (a) ZnO, (b) Cu_xO-25/ZnO, (c) Cu_xO-50/ZnO, and (d) Cu_xO-120/ZnO. (e) The atomic percent of Cu collected from EDS quantitative analysis.

The Raman spectra shown in Figure 3.2a were conducted to examine the local bonding geometry and oxidation states of electrodes. The most intense peaks for ZnO are E_2^{low} and E_2^{High} at 99 cm^{-1} and 438 cm^{-1}, respectively. E_2^{low} is ascribed to Zn sublattice vibration, while E_2^{High} is assigned to oxygen vibration in the lattice [96]. Cu_xO/ZnO electrodes show extra peaks at 147, 220, and 648 cm^{-1} which are assigned to the vibrations of Cu_2O. The two peaks at 147 and 648 cm^{-1} are assigned to T_{1u} vibration mode, while the intense peak at 220 cm^{-1} is assigned to E_u. T_{u1} and E_u are both modes that represent

the rotation of Cu tetrahedra around their centers [97]. Raman spectroscopy results suggest that the electrodeposited Cu_xO is mostly Cu^+ in the bulk. With increasing deposition time of Cu_xO, Raman spectral features of this phase gained intensity. Although SEM images indicate that ZnO and Cu_xO crystals are likely separated from each other, the appearance of new broad peaks at around 200 and 400 cm^{-1} can be attributed to a chemical interaction that could be established during the deposition of Cu_xO. These new broad peaks are close to the main peaks of Cu_2O and ZnO, which could be an indication of a change in the electronic environment of some of the electrodeposited Cu_2O and ZnO.

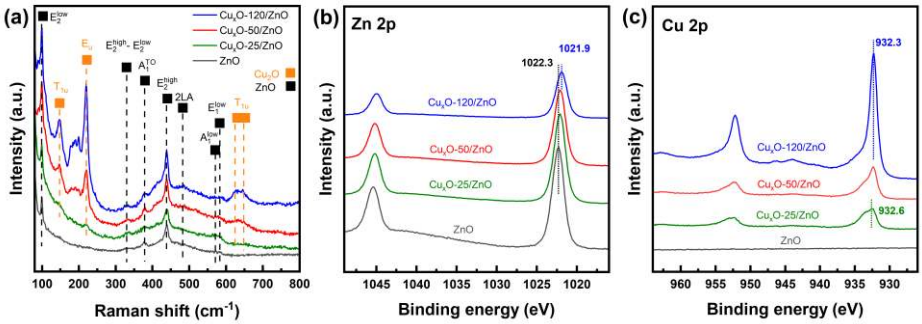

Figure 3.2.(a) Raman spectra of as-prepared electrodes. (b) Zn 2p and (c) Cu 2p XPS spectra.

To understand the chemical composition of the surface, XPS measurements were performed for all as-prepared electrodes, as shown in Figure 3.2b-c. XPS results indicate the presence of both Cu and Zn elements on the surface. Zn 2p XPS spectra show a peak at around 1022.3 eV that belongs to the ZnO phase. Zn 2p peak shifts to lower binding energy with increasing Cu_xO amount, emphasizing the interaction between Cu_xO and ZnO [98]. Since the Cu_2O deposition is cathodic, partial reduction of the ZnO surface can also be expected. Cu 2p peak intensity increases while Zn 2p decreases with increasing Cu_xO deposition time, indicating an increase in Cu amount on the surface. A similar increase in the intensity of the Cu LMM Auger spectra was also observed (Figure A1.1a). Cu 2p XPS spectrum of Cu_xO-25/ZnO shows a peak at 932.6, which could be assigned to Cu^+. An intense higher binding energy shoulder that could indicate the presence of Cu^{2+} species on the surface is also observed at 933.5 eV. This shoulder feature seems to remain intact with increasing the amount of Cu_xO, however, the main peak gains intensity and shifts to lower binding energy, similar to the Zn 2p. Cu_2O and CuO have strong and distinctive shake-up features residing between 940 and 948 eV (for Cu $2p_{3/2}$ component). These shake-up features are seen in the Cu 2p XPS spectrum of Cu_xO-120/ZnO, however,

they are lacking in other spectra. This observation might be another sign of chemical interaction, as Cu^{2+} species are , at least partially, incorporated into the ZnO structure. Both XPS and Raman spectra suggest that there is a slight interaction between both phases. O 1s spectra in Figure A1.1b points out that all electrodes might contain $Zn(OH)_2$ on the surface, which can be attributed to the conversion of ZnO to $Zn(OH)_2$ in air exposure.

The performance of the electrodes for CO_2RR was evaluated in two-compartment H-cell at constant potentials ranges from -0.8 to -1.2 V in CO_2-saturated 0.1 M $KHCO_3$. The electrodes were tested sequentially by first pre-reducing at -0.7 V for 30 min and then applying each potential for 30 min. Figure 3.3a shows the FE values of CO and H_2 for the four different electrodes. At -0.8 V, the FE of CO jumped from 48% for bare ZnO to ~75% for Cu_xO/ZnO and H_2 dropped from 35% to almost 23-26%, which suggests that the addition of Cu_xO has increased the selectivity toward CO, while reducing H_2. Interestingly, each of the Cu_xO/ZnO electrodes exhibited the highest CO selectivity at a different potential. As the amount of Cu_xO was increased, the potential at which the maximum CO production observed also increased. Specifically, Cu_xO-25/ZnO showed the highest CO production at -0.8 V, whereas Cu_xO-50/ZnO and Cu_xO-120/ZnO showed the highest CO production at -0.9 V and -1.0 V, respectively. These findings suggest that a higher potential is required to form an alloy that is responsible for the high selectivity towards CO production as the amount of Cu_xO is increased. The bare ZnO electrode exhibited high H_2 selectivity at -0.8 V, which decreased at -0.9 V that could be due to the formation of liquid formate.

To compare the intrinsic properties of electrodes, ECSA-normalized partial current densities (J_{CO}/ECSA) were estimated for both Cu_xO-50/ZnO and ZnO (see Figure A1.2). The J_{CO}/ECSA value of Cu_xO-50/ZnO was found to be slightly higher than that of ZnO at all potentials except the one at -1.2 V. This indicates that Cu_xO-50/ZnO contains a higher level of active catalytic sites, which can facilitate the reduction of CO_2 to CO.

Observations show that the total FE of the ZnO electrocatalyst was not consistently 100%. This may be attributed to the re-oxidation of the produced formate, which could pass through the membrane and reach the anode, as suggested by previous research [99]. Liquid products were measured at two different potentials, -0.8 and -1.2 V (see Table S1). At -0.8 V, a negligible amount of formate was observed, which increased at -1.2 V for

both electrodes, indicating that at a higher potential, formate formation is more favorable due to the reaction of physisorbed CO_2 with a surface *H that is more available at -1.2 V [100]. No multicarbon products were detected, which suggests that our electrodes are only active for C1 products. This could be attributed to the low *CO binding energy on the electrocatalyst and further hydrogenation requires increased binding energy of *CO [101]. To ensure reproducibility, Cu_xO-50/ZnO was repeated three times at -0.8 V and results are seen in Figure A1.3.

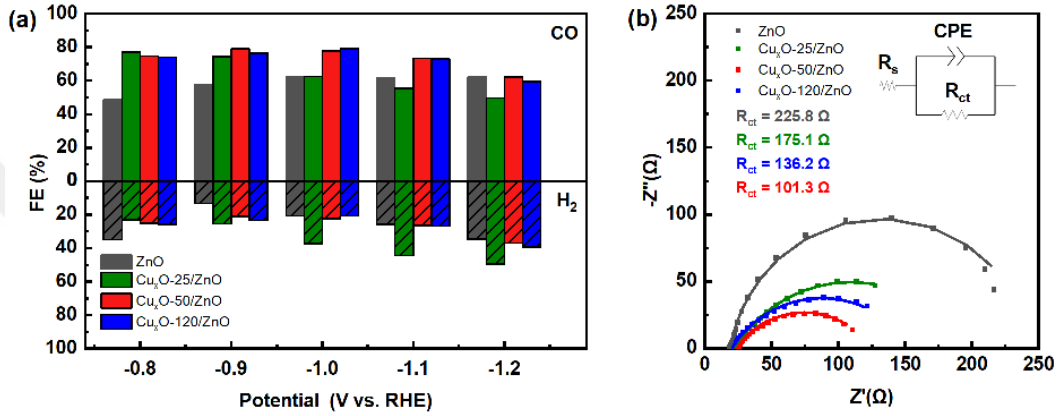

Figure 3.3. (a) FEs of electrocatalyst pre-reduced at -0.7 V for 30 min. The same electrodes were used at all potentials, each potential was applied for 30 mins sequentially. (b) Nyquist plots obtained at OCP for as-prepared electrodes in CO_2-saturated 0.1 M $KHCO_3$.

EIS was performed on the as-prepared electrocatalysts in 0.1 M $KHCO_3$ at open circuit potentials (OCPs), and Nyquist plots are shown in Figure 3.3b. All Cu_xO/ZnO electrodes exhibited lower charge transfer resistance (R_{ct}) than bare ZnO, which indicates faster charge transfer kinetics and hence, facilitated CO_2RR. Among the different electrocatalysts, Cu_xO-50/ZnO showed the lowest R_{ct} due to its more dispersed and larger amount of small nanocubes of Cu_2O as observed through FESEM characterization. It is important to note that the EIS results in Figure 3.3b represent the surface of the electrocatalysts prior to exposure to the pre-reduction process, during which significant reconstruction and alloy formation occur. Therefore , to understand the origin of the improved CO selectivity, Cu_xO-50/ZnO and bare ZnO were chosen among other electrocatalysts for post-reaction characterizations, which are shown in the following sections.

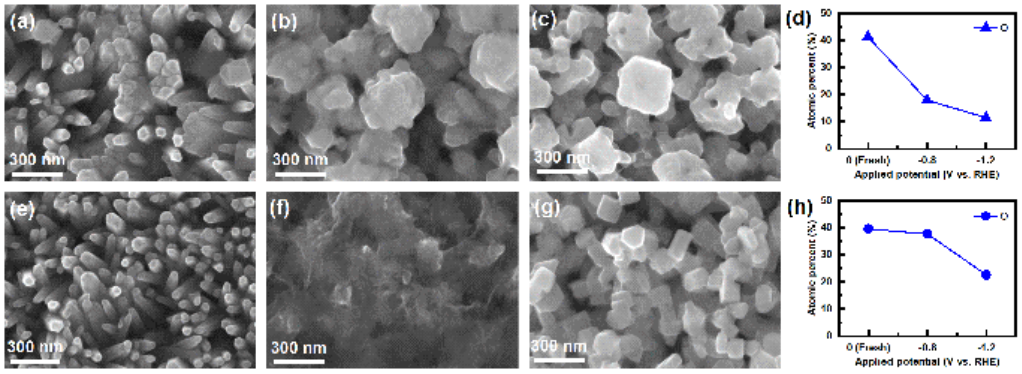

Figure 3.4. FESEM images of Cu_xO-50/ZnO (a) as-prepared, after 1h of CO_2RR at (b) -0.8 V and at (c) -1.2 V. FESEM images of ZnO (e) as-prepared, after 1h of CO_2RR at (f) -0.8 V and (g) -1.2 V. EDS quantitative analysis for as-prepared and tested (d) Cu_xO-50/ZnO, and (h) ZnO electrodes.

Cu_xO-50/ZnO and ZnO were examined after CO_2RR at two different potentials using SEM and EDS, as shown in Figure 3.4. At both potentials, electrodes underwent reconstruction where both ZnO nanorods and Cu_2O particles lost their initial morphology. FESEM images show that ZnO and Cu_xO-50/ZnO both have different final structures, which confirm that Cu has a significant influence on the structural reconstruction process. At -0.8 V, ZnO presents a porous-like structure, while at -1.2 V, it crystallizes and forms nanoparticles. It is suggested that the ZnO reduction process starts by first dissolving into the electrolyte due to the high local pH on the interface, which results in forming $Zn(OH)_4^{-2}$ ions [102] and then reduce to metallic Zn and crystalize on the surface of the electrode. Previous studies suggest that the applied potential affects the final morphology due to the difference in dissolution and re-deposition rates of the ions [91], [103]. In Cu_xO-50/ZnO, at both potentials, morphologies are so close to each other, that the surface becomes rough with chunks of particles that contain both Cu and Zn as seen in EDS mapping in Figure A1.4. Quantitative analysis by EDS presented in Figure 3.4d and h shows that, at -0.8 V, the atomic percent of oxygen in the ZnO electrode is close to the initial amount. This suggests that ZnO is partially reduced while the bulk is still in the oxide state. Meanwhile, Cu_xO-50/ZnO shows much lower O content at -0.8 V, which can be attributed to a faster reduction in Cu_xO-50/ZnO due to lower charge transfer resistance. At -1.2 V, both electrodes show a greater drop in O content which suggests a further reduction of oxides at higher potentials.

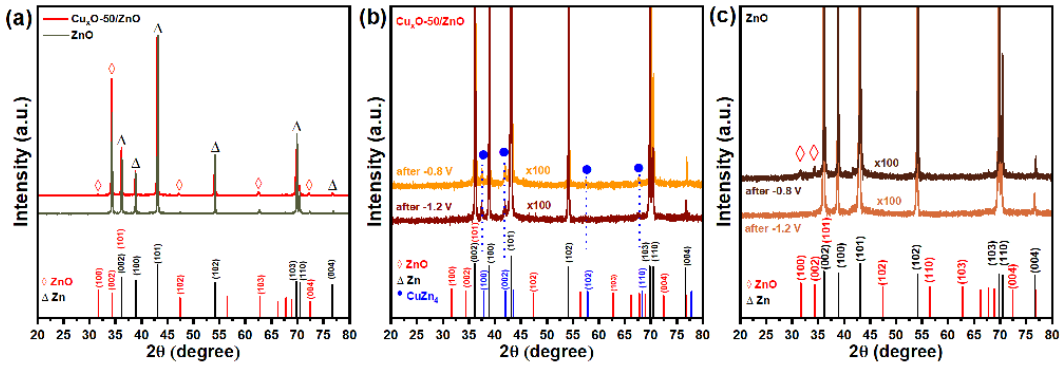

Figure 3.5. XRD reflections of (a) fresh Cu_xO-50/ZnO and ZnO. XRD reflections after -0.8 V and -1.2 V of (b) Cu_xO-50/ZnO, and (c) ZnO.

XRD reflections of both Cu_xO-50/ZnO and ZnO were measured before and after 1 h of CO_2RR at -0.8 V and -1.2 V and results are shown in Figure 3.5a-c. No reflection that can be attributed to Cu_xO planes was detected on the as-prepared Cu_xO-50/ZnO. At -0.8 V, Cu_xO-50/ZnO electrode showed a complete reduction where all peaks that belong to ZnO disappeared. Meanwhile, the ZnO electrode shows 2 peaks at 31.7° and 34.3° after 1 h at -0.8 V which indicate that ZnO is reduced faster in Cu_xO-50/ZnO than pristine ZnO, matching with EDS results. At both potentials, XRD of the Cu_xO-50/ZnO electrode showed the evolution of 4 new reflections at 37.6°, 41.9°, 57.4°, and 67.9°, which could be assigned to $CuZn_4$ alloy, confirming the dynamic behavior of the electrocatalyst and alloy formation during CO_2RR. Previous works suggest that CuZn alloys can have different binding energy to CO_2RR intermediate. For instance, Ren et al. showed that by changing Zn to Cu ratio, different FEs for CO and HCOOH were obtained, attributing this to changing *COOH binding energy [54]. Another work by Wang et al. showed that the binding energy of *COOH on the uncoordinated stepped sites of $Zn_{10}Cu$ was higher than that of on the metallic Zn, hence, a higher selectivity toward CO could be obtained [104]. We postulate that the CO selectivity enhancement we observed could be attributed to the $CuZn_4$ forming in the course of CO_2RR, presumably due to the optimized binding energy of *COOH.

To measure ECSAs of the electrodes after CO_2RR, CV scans with different scan rates were applied for Cu_xO-50/ZnO and ZnO after -0.8 V and -1.2 V (see CVs in Figure A1.5 in the Appendix). After both potentials, Cu_xO-50/ZnO showed higher double-layer capacitance than bare ZnO as shown in Figure 3.6a and b, which corresponds to a higher surface area. By dividing double layer capacitance of Cu_xO-50/ZnO to bare that of ZnO

after testing at -0.8 V, the roughness factor of Cu_xO-50/ZnO was estimated as ~1.31, whereas selectivity is 1.5 times better than bare ZnO. Therefore, it might be concluded that the improvement in the selectivity toward CO could be associated with the introduction of new active sites which have an optimum binding energy for *COOH, also confirmed by the result J_{CO}/ECSA.

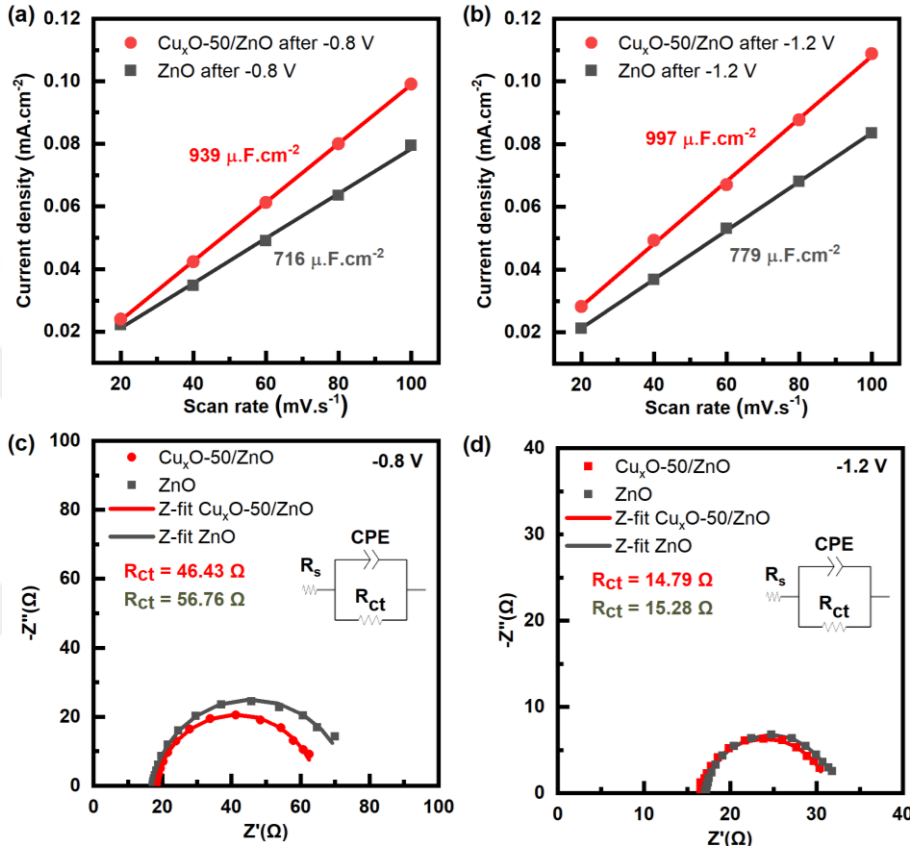

Figure 3.6. Double layer capacitance of Cu_xO-50/ZnO and ZnO after testing at (a) -0.8 V, and (b) -1.2 V in CO_2-saturated 0.1 M $KHCO_3$. Nyquist plots of Cu_xO-50/ZnO and ZnO at (c) -0.8 V, and (d) -1.2 V in CO_2-saturated 0.1 M $KHCO_3$.

EIS was measured to compare the R_{ct} of both electrocatalysts. Figure 3.6c and d exhibit Nyquist plots of Cu_xO-50/ZnO and ZnO at two different potentials in CO_2-saturated 0.1 M $KHCO_3$. To quantify circuit elements, data were fitted in a three-component circuit where R_s, R_{ct}, and CPE represent solution resistance, charge transfer resistance, and constant phase element, respectively. It is observed that at -0.8 V, Cu_xO-50/ZnO exhibits lower R_{ct} than ZnO, matching with EIS employed at OCP for as-prepared electrocatalysts. Lower R_{ct} might be a sign of a faster electron transfer which might

facilitate the conversion of adsorbed CO_2 to $*CO_2^-$ and hence, improving selectivity toward CO [46]. Meanwhile, at -1.2 V, both electrodes exhibit close charge transfer resistance where Cu_xO-50/ZnO and ZnO exhibit a value of 14.79 and 15.28 Ω, respectively. Interestingly, both electrodes showed similar FE for CO at this potential which further emphasizes the impact of lower R_{ct} in the elementary steps of CO_2RR.

The surface composition of Cu_xO-50/ZnO electrode was determined by XPS depth profile analysis after -0.8 V and -1.2 V (see Zn $2p_{3/2}$, Cu $2p_{3/2}$, Cu LMM, and O 1s spectra in Figure A1.6 and A1.7). 7 different depths were scanned every 60 s of argon ion sputtering with a total of 420 s sputtering time. Figure 3.7 shows the Cu/Zn ratio with time at the two different potentials. The results indicate that the first layer of the electrode surfaces did not contain Cu. This may be attributed to the continuous dissolution and re-deposition of ZnO during the CO_2RR process [105]. At -0.8 V, Cu/Zn ratio is higher than that at -1.2 V, which shows that the surface undergoes severe reconstruction processes during the reaction. It can be suggested that CO selectivity is higher at -0.8 V due to the higher amount of Cu at the surface, which further confirms the critical role of Cu at the surface for CO selectivity.

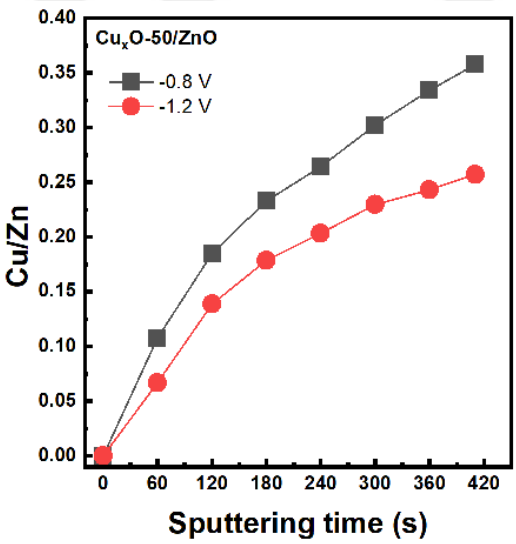

Figure 3.7. The change in Cu/Zn ratio with increasing sputtering time.

Strategies to improve CO selectivity in CO_2RR usually involve using different electrocatalysts and optimization of reaction conditions. Cu_xO is electrodeposited on ZnO, FE of CO can be maximized with a certain potential range, however, the enhancement appears to be the dynamic nature of the surface during reaction conditions

and tuning of the electrode potential can be beneficial to keep the selectivity high. CO:H_2 ratio critical to the F-T process can then be tuned by applied potential and the amount of Cu_xO initially deposited. Cu in the surface layer and CuZn alloy formation play a significant role in CO formation, however, operando spectroscopy investigations might be required to identify the nature of the adsorption site of *COOH and *CO.

3.4.Conclusion

In this chapter, we have presented 4 different ZnO electrocatalysts with different amounts of Cu_xO. CO_2RR performance tests showed that Cu_xO/ZnO electrodes had higher FE% for CO than pristine ZnO. According to EIS results, the addition of Cu_xO reduces charge transfer resistance, which may help in improving CO_2RR, as it contains multiple charge transfer steps. Cu_xO-50/ZnO was selected for post-reaction characterization at -0.8 V and -1.2 V to further understand the effect of Cu_xO on CO selectivity. XRD analysis shows that $CuZn_4$ alloy forms during the CO_2RR as a result of the dynamic behavior of the structure. Cu_xO-50/ZnO had different Cu/Zn ratios on the surface depending on the applied potential during CO_2RR. At -0.8 V, Cu_xO-50/ZnO showed a higher Cu/Zn ratio as determined by XPS. Our findings strongly indicate that the formation of $CuZn_4$ alloy in the course of CO_2RR is responsible for the higher number of active sites and optimized *COOH binding strength that leads to higher CO FE. To check the stability, Cu_xO-50/ZnO electrode was tested for 4 h at -0.8 V (see Figure A1.8). Both current density and CO FE showed high stability during this test. Overall, our work highlights the importance of the role of Cu_xO in the modification of the selectivity of ZnO and helps in designing cost-effective commercial electrocatalysts for CO_2RR to CO.

Chapter 4:Modification of ZnO by ALD Cu_xO for Enhancing CO Selectivity

4.1.Introduction

Electrochemical CO_2 reduction reaction (CO_2RR) to CO presents a promising technology for reducing carbon emissions and offers a sustainable pathway for CO_2 utilization [45]. However, the high cost of current electrocatalysts, which are primarily based on Ag and Au, limits their wide range utilization. Zn is the only rare-earth metal capable of producing CO with acceptable selectivity. Nevertheless, a significant overpotential must be applied to bulk Zn to achieve satisfactory activity and selectivity [35]. Alternative solutions, such as nanostructured Zn, oxide-derived Zn, and bimetallic Zn-based alloys, have been explored to enhance the catalytic behavior of bulk Zn. Nanostructured Zn, for instance, has demonstrated high selectivity to CO, reaching Faradaic efficiency (FE) values of up to 95% [86], [87], [106], [107]. Oxide-derived Zn has also shown improved CO selectivity, with FE values exceeding 90% [88], [90], [91], [108]. The increased surface area provided by these nanostructures introduces new active sites, rendering them more selective and active than bulk Zn. Bimetallic AgZn electrocatalysts have exhibited high CO FEs [109], [110], while bimetallic CuZn catalysts have emerged as another promising candidate. Wan et al. reported a phase-separated CuZn catalyst with a 94% FE for CO [49], attributing this improvement to the enhanced binding energy of the carboxyl (*COOH) intermediate. Similarly, Wang et al. demonstrated a CuZn-based catalyst with a 95% FE for CO [104], again attributing the enhancement to the superior binding energy of the *COOH intermediate. Xue et al. showed that decorating ZnO with Cu increased the FE to 90% [46].

Atomic layer deposition (ALD) stands out among other thin film fabrication techniques due to its high uniformity and precise thickness control. It proves particularly advantageous when substrates of complex structures, such as nanorods are used, ensuring a uniform coating throughout. In addition, ALD operates under comparatively lower temperatures than other similar methods, which mitigates any potential damage to the substrate that can be caused by high-temperature procedures [111]. Several works attempted to use electrocatalysts synthesized by ALD for the CO_2RR. Sherier et al demonstrated that the ALD of SnO_2 onto CuO nanowires enhanced the selectivity toward

CO, attributing this to the diminished adsorption strength of CO_2 to CO reaction key intermediates.[112]. In another work, Zheng and co-workers showed that S-modulated Sn synthesized through ALD improved the selectivity of formate ($HCOO^-$) to FE of 93%. The usage of ALD allowed them to precisely control the amount of S and thickness of the film and hence better CO_2RR performance [113]. Ren et al, revealed that a small layer of ZnO added via ALD to CuO nanowires was able to increase the ethanol C_2H_5OH/C_2H_4 ratio over five times and achieve a FE of 41% for C_2 products. This enhancement was attributed to the modification in adsorption of intermediate that was confirmed by in-situ Raman spectroscopy [114].

In this study, we present that ZnO nanorods coated with Cu_xO via ALD exhibit higher selectivity to CO than bare ZnO. The FE of CO reaches a peak of 88% at an optimal Cu_xO coverage at a comparatively low potential (-0.8 V). Comprehensive characterizations were undertaken to understand the origins of this enhancement. We showed ε-$CuZn_4$ phase had developed during the pre-reduction step. Moreover, the electrodes possessed different surface composition than the bulk, the optimum Cu_xO/ZnO had the highest Cu content on the surface, leading to a lower charge transfer resistance and the required Cu/Zn ratio on the surface. These combinations resulted in a synergy effect between ε-$CuZn_4$ and Zn- η phases that co-existed simultaneously at the surface of electrocatalysts.

4.2.Experimental procedure

All experimental procedures regarding synthesis, testing and characterizing are described in chapter 2.

4.2.1.Electrochemical measurements:

Electrochemical surface area (ECSA) measurements were performed in CO_2-saturated 0.1 M $KHCO_3$ by applying cyclic voltammetry (CV) with different scan rates. Finding a non-faradic region for the as-prepared electrodes was somewhat challenging due to instabilities during anodic sweep; therefore, the range was selected from the open circuit potential (OCP) to -0.1 V away from OCP, with six different scan rates: 20, 40, 60, 80, 100, and 200 $mV.s^{-1}$. The 20 $mV.s^{-1}$ scan rate was excluded in calculations of double-layer capacitance (C_{dl}) due to its deviation. For ECSA measurements after CO_2RR tests, cyclic voltammetry (CV) scans with five different scan rates: 20, 40, 60, 80, and

100 mV.s^{-1} were applied. The potential range was selected in a non-faradic region, which was easier to find than for as-prepared electrodes between -0.5 and -0.6 V.

4.2.2. Quantitative Analysis of ε and η Phases

The ε and η phases were determined from the phase diagram depicted in Figure B1.10. Cu/Zn ratios were sourced from EDS (for bulk composition) and XPS (for surface composition). Subsequently, the lever rule was used to quantify each phase. We operated under the assumption that the presence of oxides on the surface was minimal and that no phases other than ε and η exist. This assumption was based on the data collected by XRD, which showed no peaks other than those corresponding to the two aforementioned phases.

4.3.Results and Discussion

Figure 4.1 shows the FESEM images of the as-prepared Cu_xO-/ZnO electrodes as a function of the number of ALD cycles. Figure 4.1a shows the bare ZnO electrode where nanorods are distributed across the surface, providing a homogenous surface for the subsequent ALD Cu_xO deposition. Figure 4.1b shows the Cu_xO-100/ZnO where Cu_xO particles are barely discernible due to their small thickness. Cu_xO overlayer grows and becomes more visible with increasing cycle number. In the case of Cu_xO-150/ZnO, cubic Cu_xO particles are observed to partially cover the nanorods whereas at Cu_xO-250/ZnO electrode, Cu_xO particles almost entirely cover the ZnO nanorods. As the number of ALD cycles further increases, the Cu_xO particles start to agglomerate forming larger particles cluster (Figure 4.1e and 4.1f). It is important to note that the orientation of ZnO nanorods may exhibit a slight variation between electrodes, which is due to a slight variation in the electrodeposition condition between electrodes employed during synthesis. Despite these small differences, the overall homogenous distribution and the growth of ZnO nanorods and Cu_xO particles remain consistent across the electrodes.

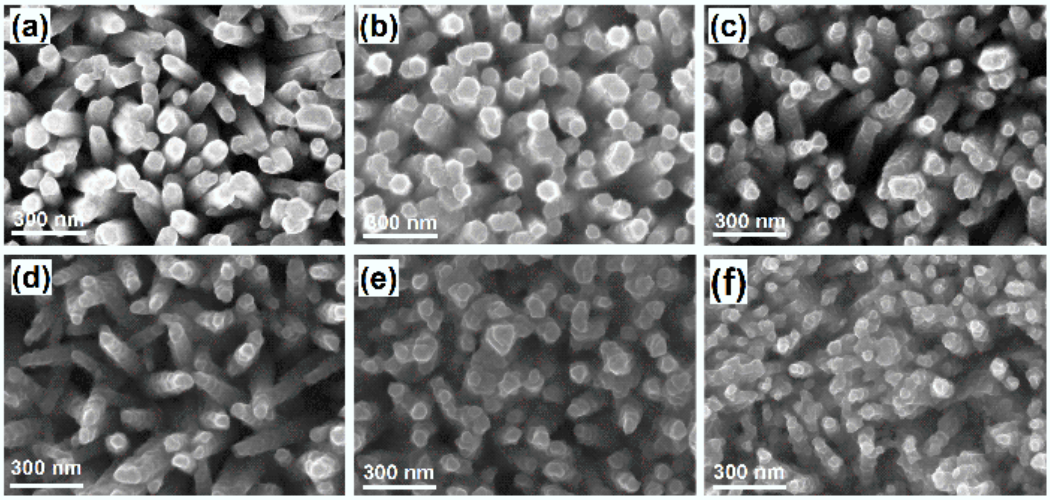

Figure 4.1.FESEM images of as-prepared electrodes. (a) ZnO, (b) Cu_xO-100/ZnO, (c) Cu_xO-150/ZnO, (d) Cu_xO-250/ZnO, (e) Cu_xO-400/ZnO, and (f) Cu_xO-500/ZnO.

Figure 4.2 presents the Raman spectra for the as-prepared electrodes. The measurements were taken to identify the Cu oxidation states in the bulk materials and observe the evolution of peaks with increasing ALD cycle numbers. Four main peaks associated with ZnO can be observed at 99.5 cm^{-1}, 335 cm^{-1}, 374 cm^{-1}, and 438 cm^{-1}. These peaks correspond to the E_2^{low}, E_2^{high}-E_2^{low}, A_1(TO), and E_2^{high} vibrational modes of ZnO respectively [96], [115]. The E_2^{low} and E_2^{high} modes are related to the vibrations of the Zn and O atoms in the wurtzite crystal structure of ZnO, E_2^{high}-E_2^{low} corresponds to a difference in frequency between these two vibrational modes, while $A_1^{(TO)}$ is associated with the transverse optical mode of ZnO [116]. The Cu_xO peaks at 147 cm^{-1} and 220 cm^{-1}, assigned to the Cu^+ oxidation state, become more prominent with increasing cycle numbers, indicating the progressive growth of Cu_2O on the surface. These vibrational modes are attributed to the second-order E_u mode and T_{1u} respectively, which both correspond to the rotations of Cu tetrahedra around their centers [117].

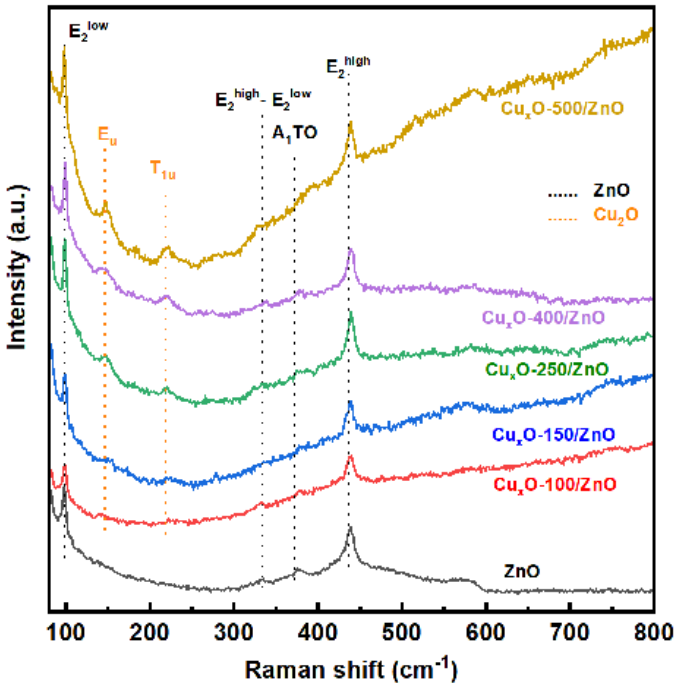

Figure 4.2. Raman spectra of as-prepared electrodes.

To examine the surface composition and oxidation states, XPS measurements were implemented for the as-prepared electrodes. As demonstrated in Figure B1.1a, the Zn 2p spectra align with the binding energy of ZnO for all electrodes [118], [119]. Meanwhile, a shift to higher binding energy in Zn 2p spectra is observed with the increase of Cu_xO. This shift is indicative of a reduction in the electron density around the Zn atoms due to the introduction of Cu_xO [46], [49], [50]. Concurrently, the Cu 2p spectra reveal that electrode surfaces show both Cu^+ and Cu^{2+}. The presence of Cu^{2+} is associated with a pronounced satellite feature between the Cu $2p_{3/2}$ and Cu $2p_{1/2}$ peaks, as well as another satellite at binding energy exceeding that of Cu $2p_{1/2}$. A depth profile analysis, depicted in Figure B1.2, was performed specifically on the Cu_xO-250/ZnO electrode. These findings confirm that Cu^{2+} is confined to the topmost surface layer, which disappears after 60 seconds of soft sputtering. This observation aligns with the Raman results, which did not show any peaks associated with Cu^{2+}. The formation of this layer is likely due to air-induced oxidation.

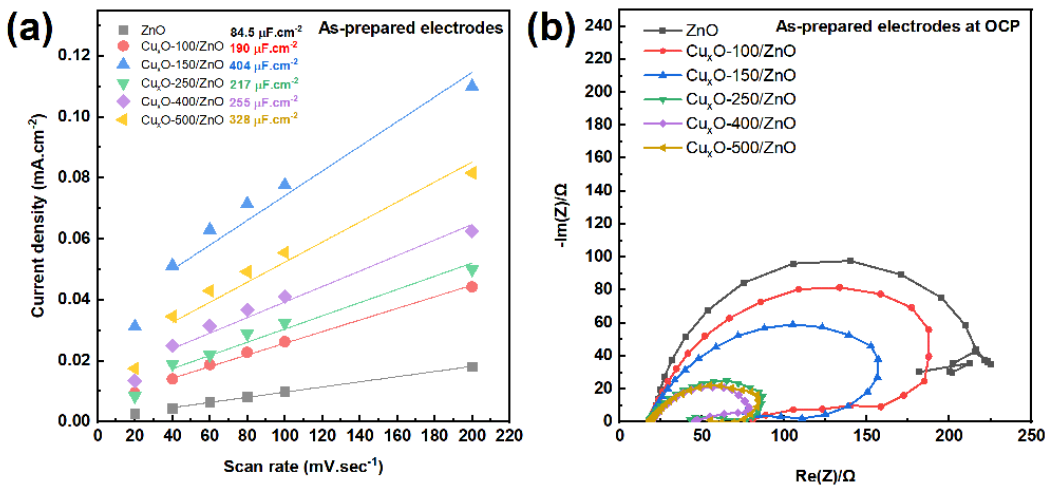

Figure 4.3. (a) C_{dl} of the as-prepared electrodes estimated from the changes in anodic and cathodic charging measurement at different potential scan rates. (b) Nyquist plots of as-prepared electrodes. Both performed in CO_2-saturated 0.1 M $KHCO_3$.

To understand the effect of Cu_xO on C_{dl} and R_{ct}, ECSA and EIS measurements were carried out on the as-prepared electrodes in CO_2-saturated 0.1 M $KHCO_3$. The ECSA results reveal that the addition of Cu_xO increases the electrochemical surface area for the as-prepared electrodes, with Cu_xO-150/ZnO exhibiting the highest C_{dl} value. This can be attributed to the Cu_xO content, which has not yet begun to cover the nanorods and form a compact layer, thus providing the largest initial surface area among other electrodes. It is worth noting that the electrodes undergo significant changes during the CO_2RR and pre-reduction steps. Therefore, post-reaction characterizations were performed to understand these alterations during CO_2RR. Figure 4.3b represents the Nyquist plots that were obtained at an OCP. Based on the radius of the Nyquist plots, the R_{ct} of Cu_xO/ZnO became significantly smaller than bare ZnO, suggesting the accelerated charge transfer process to adsorbed species for forming the reactive intermediates.

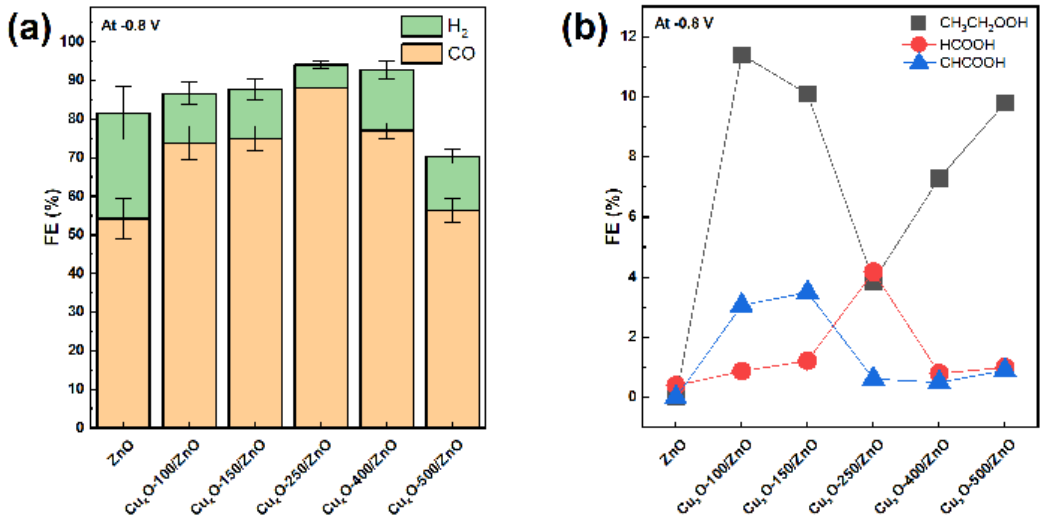

Figure 4.4. FEs of (a) gaseous products and, (b) liquid products at -0.8 V.

The electrocatalytic performance test reveals that the addition of Cu_xO leads to an enhancement in CO selectivity at -0.8 V. Figure 4.4a and 4b presents the FE values for both gaseous and liquid products for the 6 different electrocatalysts. The FE of CO increases with the number of ALD cycles up to Cu_xO-250/ZnO electrode, where it reaches a maximum value of 88%. Beyond Cu_xO-250/ZnO, the CO FE drops while C_2H_5OH and H_2 increase again. The increase in C_2H_5OH selectivity in favor of CO indicates that CO formed on 400-Cu_xO/ZnO and 500-Cu_xO/ZnO electrodes had further reacted to form C2 products, suggesting a change in the chemical nature of active sites [54].

Figure B1.3 shows the FE of gaseous products at 5 different applied potentials ranging from -0.8 V to -1.2 V. Notably, the Cu_xO-400/ZnO and Cu_xO-500/ZnO electrodes exhibit higher CO selectivity at more negative potentials. This observation emphasizes that when the Cu_xO overlayer is thick, the electrodes require greater applied potentials to promote the formation of CO, which could be attributed to the higher potential required to form the active surface for CO formation. As the electrodes undergo a re-construction process, the applied potential affects the dissolution rate of Zn atoms and hence, affects Cu/Zn ratio on the surface [91], [103].

To emphasize the synergistic effect of both oxide layers, Cu_xO-250 was synthesized directly on Zn foil without the ZnO nanorods layer. Figure B1.4 presents the FE of gaseous products at the 5 different potentials. A clear distinction can be observed between the performance of the two electrodes. The Cu_xO-250/ZnO electrode exhibits a higher

CO selectivity significantly and lower H_2 compared to the Cu_xO-250 electrode. This control experiment highlights the importance of the synergistic effect between Cu_xO and ZnO layers in achieving high CO selectivity. The reduction of these layers during pre-reduction and CO_2RR is crucial in the formation of ε-$CuZn_4$ alloy that possesses a higher density of CO-active sits compared to both bare ZnO and Cu_xO-250 layers.

Figure 4.5a presents the ECSA measurements after CO_2RR at -0.8 V. The C_{dl} of the electrodes has significantly increased after CO_2RR compared to the as-prepared electrodes. This increase is due to the formation of new porous morphology with a higher surface area than the initial structures. In line with the results obtained from as-prepared electrodes, the results clearly demonstrate that the addition of Cu_xO increases the C_{dl}, which is correlated to the surface area and consequently increases the activity of the electrodes. Even a tiny amount of Cu_xO, as seen in the case of Cu_xO-100/ZnO was capable of increasing the C_{dl} by 2.3 times. This enhancement is attributed to the change in the dissolution/re-deposition process that occurs differently among electrodes during pre-reduction and CO_2RR. The C_{dl} of the electrodes continues to increase up to Cu_xO-400/ZnO and then experiences a slight decrease, due to the agglomeration of CuZn particles, which also can be seen in Figure 4.6. Although the Cu_xO-250/ZnO and Cu_xO-500/ZnO electrodes appear to have similar double-layer capacitance, their selectivities are quite distinct This observation suggests that increasing the amount of Cu_xO changes the nature of active sites, which in turn affects the selectivity of the electrocatalytic process.

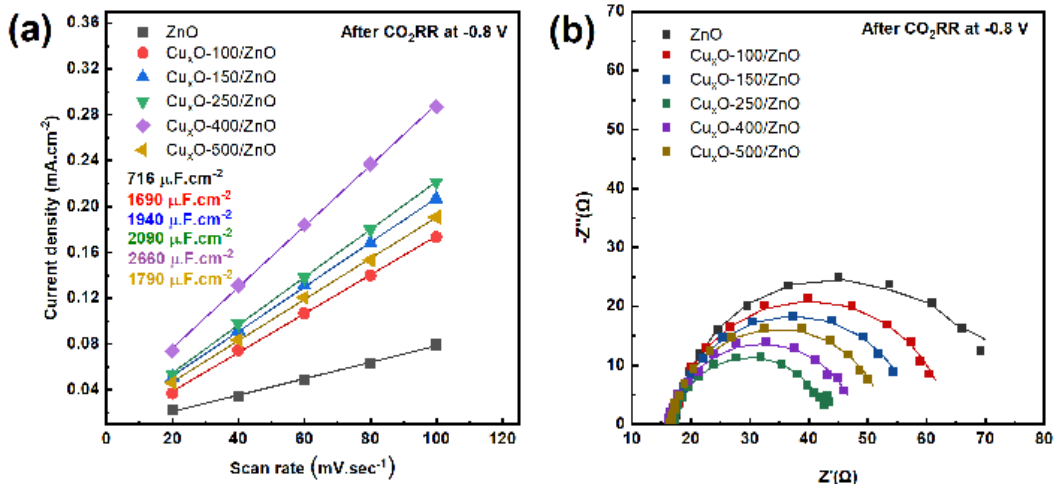

Figure 4.5. (a) Double layer capacitance of the electrodes, and (b) Nyquist plots employed at -0.8 V. Both measurements were implemented for CO_2RR tested electrodes at -0.8 V in CO_2-saturated 0.1 M $KHCO_3$.

Figure 4.5b presents the Nyquist plots of the 6 different electrodes after CO_2RR at -0.8 V. The results indicate that the addition of Cu_xO reduces the R_{ct} for all Cu_xO-ZnO electrodes. Interestingly, Cu_xO-250/ZnO showed the highest CO selectivity and lowest R_{ct}, suggesting that an optimum amount of Cu_xO layer minimizes the value of R_{ct}, and consequently, contributes to its enhanced electrocatalytic activity and selectivity toward CO.

Figure B1.5a shows the J_{co} at five different potentials. J_{co} increases with the increasing applied potential where Cu_xO-250/ZnO showed the highest J_{co} compared to the other electrodes until -1.1 V. The high J_{co} of Cu_xO-250/ZnO derives from a combination of high selectivity and high surface area value shown in Figure 4.5a. Figure B1.5b showcases the partial current density, normalized to C_{dl}. Among all tested electrodes Cu_xO-250/ZnO maintained its superior performance with the highest normalized J_{co}. This suggests that high J_{co} at -0.8 V comes from the more selective characteristic of active sites, promoting the need for further analysis to understand the reasons behind this enhancement.

Figure 4.6 presents the FESEM images of the electrodes after CO_2RR at -0.8 V for 1 h. It is evident that the morphology of the electrodes has undergone significant changes, resulting in distinct structures. The bare ZnO electrode transformed into a porous

structure, while the other electrodes developed into an agglomeration of nanoparticles. As the amount of Cu_xO increased, the agglomeration became more pronounced, as seen in Cu_xO-500/ZnO electrode. Both Cu_xO and ZnO got reduced during pre-reduction and CO_2RR processes, forming an ε-$CuZn_4$ alloy that was confirmed by XRD (see Figure B1.6). After the pre-reduction process at -0.7 V, all ZnO peaks disappeared except for the CuxO-100/ZnO electrode which showed small peaks of ZnO remaining. It appears that the addition of Cu_xO facilitates the reduction of ZnO nanorods.

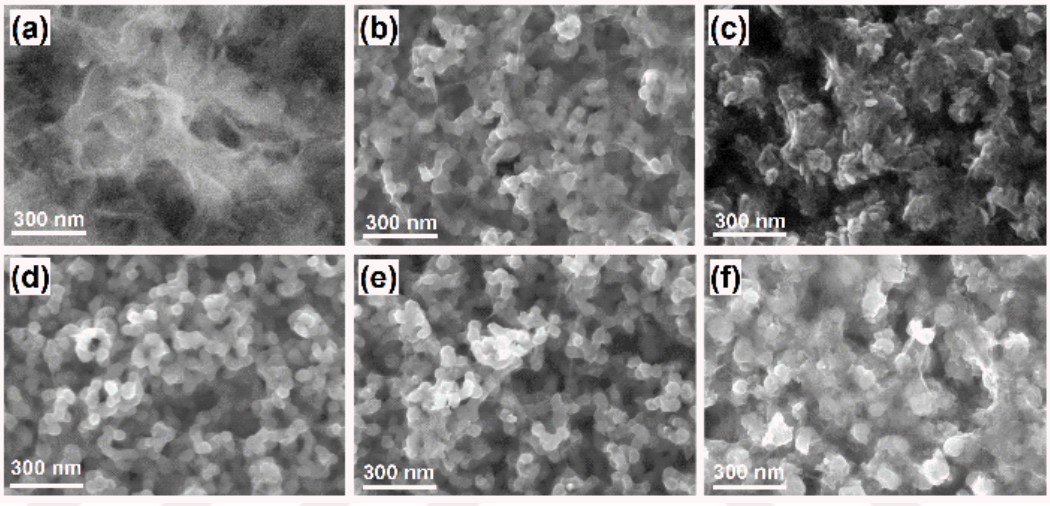

Figure 4.6. FESEM images of electrodes after CO_2RR at -0.8 V for 1 h. (a) ZnO, (b) Cu_xO-100/ZnO, (c) Cu_xO-150/ZnO, (d) Cu_xO-250/ZnO, (e) Cu_xO-400/ZnO, and (f) Cu_xO-500/ZnO.

Even though it is proved that the ε-$CuZn_4$ alloy forms during the pre-reduction process, the surface composition changes, depending on the applied potential during CO_2RR. This was concluded from ICP measurements. The concentration of dissolved Zn in the electrolyte after 1 h at -0.8 V, was found to be lower than that observed after the pre-reduction step, noting that CO_2RR at -0.8 V was conducted after a pre-reduction step for 30 mins utilizing the same electrolyte (Figure B1.7a).

This can be explained by the re-deposition of Zn ions that dissolved during pre-reduction. This observation emphasizes that Cu/Zn ratio on the surface might not maintain the same at different potentials. Meanwhile, the dissolution of Zn increases with the amount of Cu_xO overlayer, possibly due to a galvanic effect between Cu and Zn atoms which might prompt Zn atoms to preferentially dissolve. Interestingly, no Cu species are detected either after -0.8 V or after pre-reduction, suggesting a complete re-deposition of

Cu to form a ε-$CuZn_4$ alloy. This dynamic behavior of the surface underlines the complex interplay at work and requires further investigation on surfaces of electrodes to understand their composition during CO_2RR.

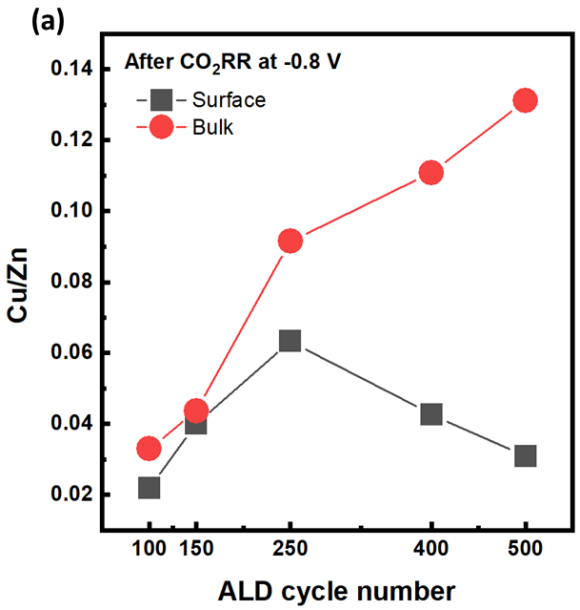

(b)

Electrode	Bulk (EDS)		Surface (XPS)	
	η%	ε %	η%	ε %
Cu_xO-100/ZnO	75%	25%	84.15	15.85
Cu_xO-150/ZnO	67.5%	32.5%	71.28	28.72
Cu_xO-250/ZnO	34.8%	65.2%	55.71	44.29
Cu_xO-400/ZnO	22.5%	77.5%	69.56	30.44
Cu_xO-500/ZnO	10%	90%	77.86	22.14

Figure 4.7. (a). Cu/Zn ratio obtained from XPS and EDS after CO_2RR at -0.8 V for 1 h. The quantification of the surface Cu/Zn ratio was performed by first normalizing the background of the spectra, followed by the integration of Zn $2p_{3/2}$ and Cu $2p_{3/2}$ XPS peaks. (b) The ratio of ε and η phases was calculated from Cu-Zn phase diagrams (Additional details pertaining to the calculation methods can be found in the Experimental section)

XPS and EDS were conducted after CO_2RR at -0.8 V to find the precise Cu/Zn ratio on the surface and the bulk of the electrodes. Surface-sensitive XPS results showed that the surface of electrodes composes of ZnO, where Zn 2p shows a binding energy corresponding to ZnO on the surface. (see Figure B1.7). Cu 2p spectra showed no evidence of Cu specie on the upper surface of Cu_xO-100/ZnO, the others however might contain a minute amount. This observation can likely be attributed to the higher tendency of re-deposited Zn atoms to oxidize when exposed to air. To counteract this, the surface of the electrodes was sputtered for 60 s to remove the layer of ZnO. Cu layers were then observed as shown in Figure B1.9. By quantifying Cu/Zn ratio on the surface (Figure 4.7), it was observed that Cu/Zn ratio first increases with the Cu content until it peaks at Cu_xO-250/ZnO, after which it starts to descend. This pattern provides a plausible explanation for the similar selectivity exhibited by Cu_xO-400/ZnO and Cu_xO-150/ZnO electrodes.

Nonetheless, Cu_xO-500/ZnO showed lower selectivity than Cu_xO-100/ZnO regardless of close Cu/Zn ratio, potentially due to its distinctive morphology, as shown in Figure 4.6. Conversely, the bulk Cu/Zn ratio exhibited an almost linear increment in correspondence with the Cu amount, aligning with expectations based on the increasing ALD cycle numbers. At these atomic ratios provided on the surface and in the bulk, two phases, ε and η, could potentially arise, which is further substantiated by the XRD reflections displayed in Figure B1.6 and B1.7.

From Cu-Zn binary phase diagram, the fraction of ε and η phases were calculated for the bulk and surface. Notably, Cu_xO-250/ZnO exhibited a proportion of 44.3% ε and 55.7% η phase. This emphasizes the synergistic effects between these phases in boosting CO selectivity, as both phases co-exist simultaneously in close ratios.

4.4.Conclusion

In conclusion, this study offers critical insights into the behavior of oxide-derived CuZn-based electrodes. The synthesized Cu_xO/ZnO electrodes using ALD of CuxO exhibited promising CO selectivity reaching 88% at -0.8 V for Cu_xO-250/ZnO. Several compositional, structural, and electrochemical characterizations were performed to understand the role of Cu_xO in CO selectivity enhancement. The observed differences between the bulk and surface composition underline the dynamic nature of these electrocatalysts under CO_2RR. Our results also highlight the important roles played by the reconstruction process and the galvanic effect between Cu and Zn atoms in modulating the surface composition and the selectivity of these electrodes. Our finding suggests that the enhanced catalytic activity of Cu_xO-250/ZnO is derived from the lowest R_{ct}, the formation of ε -$CuZn_4$ phase that exhibited higher selectivity toward CO than bare η-Zn. The current density of Cu_xO-250/ZnO was tested to be stable for more than 4 h (see Figure B1.11), offering viable alternatives to traditional precious metal-based CO electrocatalysts. This work not only expands our current understanding of CuZn-based electrocatalysts but also creates new pathways for future studies in designing more efficient electrocatalysts for CO_2RR.

Chapter 5:Summary and Conclusions

In the first part of this study, we explored the performance of electrodeposited Cu_xO-ZnO electrocatalysts for CO_2RR to CO. Compared to the bare ZnO, these electrodes demonstrated a superior selectivity toward CO formation. Post-reaction characterization revealed that the electrodes underwent a reconstruction process during which both oxide phases were reduced. Further, XRD analysis indicated the formation of a $CuZn_4$ alloy post-CO_2RR, which was proposed as the crucial alloy in the enhanced selectivity. EIS indicated that Cu_xO-50/ZnO presented a lower R_{ct} at -0.8 V compared to bare ZnO. Despite acknowledging that Rct does not necessarily affect product selectivity, we propose that reducing R_{ct} played a noteworthy role in enhancing CO_2RR performance towards CO. XPS depth profile analysis suggested a different surface composition for Cu_xO-50/ZnO after CO_2RR at -0.8 V and -1.2 V. Notably, higher Cu/Zn ratio was observed after -0.8 V, aligning with observed CO selectivity patterns. We hence assert that the presence of Cu in specific ratios initially boosts the selectivity towards CO during CO_2RR.

In the second part, we further explored the effects the addition Cu_xO on ZnO via ALD, where we synthesized a series of electrodes with varying ALD cycles. Remarkably, the Cu_xO-250/ZnO electrode outperformed the others, achieving a FE of 88% at -0.8 V. Interestingly, this electrode also showed the lowest R_{ct} among all the others, indicating that a reduced R_{ct} could indeed play a significant role in improving CO selectivity. Post-CO_2RR XPS analysis revealed that the Cu_xO-250/ZnO electrode had the highest Cu content on the surface among all the tested electrodes, which emphasizes that the initial amount of Cu_xO in the fresh electrodes does not necessarily reflect the actual surface composition during and after CO_2RR due to the dynamic nature of this electrocatalysts. Additionally, we tracked the development and appearance of the $CuZn_4$ alloy during CO_2RR, where we observed the emergence of the alloy after pre-reduction at -0.7 V further development during CO_2RR.

These findings offer valuable insights that can guide future studies in designing stable and selective Cu-Zn-based electrocatalysts and in understanding the active phase for CO production. We recommend further in-situ investigations utilizing XPS, Raman spectroscopy, and X-ray absorption spectroscopy (XAS) for a more comprehensive

understanding of surface changes occurring during CO_2RR. The dynamic nature of these electrodes might pose challenges for commercializing such electrocatalysts. Therefore, more in-situ studies could provide insights into stabilization strategies of such electrocatalysts. Additionally, we believe that this study offers valuable insights into ALD Cu_xO, which could be effectively utilized for synthesis on hydrophobic gas diffusion electrodes (GDE) and further industrialization of the technique.

Chapter 6:Bibliography

[1] G. Marland, T. A. Boden, and R. J. Andres, "Global, Regional, and National Fossil Fuel CO2 Emissions." Environmental System Science Data Infrastructure for a Virtual Ecosystem, 1985. doi: 10.15485/1463701.

[2] D. M. Etheridge, L. P. Steele, R. L. Langenfelds, R. J. Francey, J.-M. Barnola, and V. I. Morgan, "Natural and anthropogenic changes in atmospheric CO_2 over the last 1000 years from air in Antarctic ice and firn," *J. Geophys. Res.*, vol. 101, no. D2, pp. 4115–4128, Feb. 1996, doi: 10.1029/95JD03410.

[3] A. J. Dolman, R. Valentini, and A. Freibauer, Eds., *The Continental-Scale Greenhouse Gas Balance of Europe*, vol. 203. in Ecological Studies, vol. 203. New York, NY: Springer New York, 2008. doi: 10.1007/978-0-387-76570-9.

[4] J. D. Shakun *et al.*, "Global warming preceded by increasing carbon dioxide concentrations during the last deglaciation," *Nature*, vol. 484, no. 7392, pp. 49–54, Apr. 2012, doi: 10.1038/nature10915.

[5] J. Rogelj *et al.*, "Paris Agreement climate proposals need a boost to keep warming well below 2 °C," *Nature*, vol. 534, no. 7609, pp. 631–639, Jun. 2016, doi: 10.1038/nature18307.

[6] J. Albo, P. Luis, and A. Irabien, "Carbon Dioxide Capture from Flue Gases Using a Cross-Flow Membrane Contactor and the Ionic Liquid 1-Ethyl-3-methylimidazolium Ethylsulfate," *Ind. Eng. Chem. Res.*, vol. 49, no. 21, pp. 11045–11051, Nov. 2010, doi: 10.1021/ie1014266.

[7] Z. Yang *et al.*, "Electrochemical Energy Storage for Green Grid," *Chem. Rev.*, vol. 111, no. 5, pp. 3577–3613, May 2011, doi: 10.1021/cr100290v.

[8] S. Nitopi *et al.*, "Progress and Perspectives of Electrochemical CO_2 Reduction on Copper in Aqueous Electrolyte," *Chem. Rev.*, vol. 119, no. 12, pp. 7610–7672, Jun. 2019, doi: 10.1021/acs.chemrev.8b00705.

[9] S. J. Davis *et al.*, "Net-zero emissions energy systems," *Science*, vol. 360, no. 6396, p. eaas9793, Jun. 2018, doi: 10.1126/science.aas9793.

[10] T. Lockwood, "A Compararitive Review of Next-generation Carbon Capture Technologies for Coal-fired Power Plant," *Energy Procedia*, vol. 114, pp. 2658–2670, Jul. 2017, doi: 10.1016/j.egypro.2017.03.1850.

[11] N. S. Sifat and Y. Haseli, "A Critical Review of CO2 Capture Technologies and Prospects for Clean Power Generation," *Energies*, vol. 12, no. 21, p. 4143, Oct. 2019, doi: 10.3390/en12214143.

[12] M. Hanifa, R. Agarwal, U. Sharma, P. C. Thapliyal, and L. P. Singh, "A review on CO2 capture and sequestration in the construction industry: Emerging approaches and commercialised technologies," *Journal of CO2 Utilization*, vol. 67, p. 102292, Jan. 2023, doi: 10.1016/j.jcou.2022.102292.

[13] R.-P. Ye *et al.*, "CO2 hydrogenation to high-value products via heterogeneous catalysis," *Nat Commun*, vol. 10, no. 1, p. 5698, Dec. 2019, doi: 10.1038/s41467-019-13638-9.

[14] C.-H. Huang and C.-S. Tan, "A Review: CO2 Utilization," *Aerosol Air Qual. Res.*, vol. 14, no. 2, pp. 480–499, 2014, doi: 10.4209/aaqr.2013.10.0326.

[15] B. Kumar, M. Llorente, J. Froehlich, T. Dang, A. Sathrum, and C. P. Kubiak, "Photochemical and Photoelectrochemical Reduction of CO_2," *Annu. Rev. Phys. Chem.*, vol. 63, no. 1, pp. 541–569, May 2012, doi: 10.1146/annurev-physchem-032511-143759.

[16] N. Zhang, R. Long, C. Gao, and Y. Xiong, “Recent progress on advanced design for photoelectrochemical reduction of CO2 to fuels,” *Sci. China Mater.*, vol. 61, no. 6, pp. 771–805, Jun. 2018, doi: 10.1007/s40843-017-9151-y.
[17] P. R. Yaashikaa, P. Senthil Kumar, S. J. Varjani, and A. Saravanan, “A review on photochemical, biochemical and electrochemical transformation of CO2 into value-added products,” *Journal of CO2 Utilization*, vol. 33, pp. 131–147, Oct. 2019, doi: 10.1016/j.jcou.2019.05.017.
[18] J. Grodkowski and P. Neta, “Copper-Catalyzed Radiolytic Reduction of CO_2 to CO in Aqueous Solutions,” *J. Phys. Chem. B*, vol. 105, no. 21, pp. 4967–4972, May 2001, doi: 10.1021/jp004567d.
[19] S. Garg *et al.*, “Advances and challenges in electrochemical CO_2 reduction processes: an engineering and design perspective looking beyond new catalyst materials,” *J. Mater. Chem. A*, vol. 8, no. 4, pp. 1511–1544, 2020, doi: 10.1039/C9TA13298H.
[20] G. Glockler, “Carbon–Oxygen Bond Energies and Bond Distances,” *J. Phys. Chem.*, vol. 62, no. 9, pp. 1049–1054, Sep. 1958, doi: 10.1021/j150567a006.
[21] W. Lai, Y. Qiao, J. Zhang, Z. Lin, and H. Huang, “Design strategies for markedly enhancing energy efficiency in the electrocatalytic CO_2 reduction reaction,” *Energy Environ. Sci.*, vol. 15, no. 9, pp. 3603–3629, 2022, doi: 10.1039/D2EE00472K.
[22] Y. Cao, Q. Chen, C. Shen, and L. He, “Polyoxometalate-Based Catalysts for CO2 Conversion,” *Molecules*, vol. 24, no. 11, p. 2069, May 2019, doi: 10.3390/molecules24112069.
[23] S. Verma, B. Kim, H.-R. “Molly” Jhong, S. Ma, and P. J. A. Kenis, “A Gross-Margin Model for Defining Technoeconomic Benchmarks in the Electroreduction of CO_2,” *ChemSusChem*, vol. 9, no. 15, pp. 1972–1979, Aug. 2016, doi: 10.1002/cssc.201600394.
[24] Y. Hua, J. Wang, T. Min, and Z. Gao, “Electrochemical CO2 conversion towards syngas: Recent catalysts and improving strategies for ratio-tunable syngas,” *Journal of Power Sources*, vol. 535, p. 231453, Jul. 2022, doi: 10.1016/j.jpowsour.2022.231453.
[25] M. Ramdin *et al.*, “High Pressure Electrochemical Reduction of CO_2 to Formic Acid/Formate: A Comparison between Bipolar Membranes and Cation Exchange Membranes,” *Ind. Eng. Chem. Res.*, vol. 58, no. 5, pp. 1834–1847, Feb. 2019, doi: 10.1021/acs.iecr.8b04944.
[26] M. Todoroki, K. Hara, A. Kudo, and T. Sakata, “Electrochemical reduction of high pressure CO2 at Pb, Hg and In electrodes in an aqueous KHCO3 solution,” *Journal of Electroanalytical Chemistry*, vol. 394, no. 1–2, pp. 199–203, Sep. 1995, doi: 10.1016/0022-0728(95)04010-L.
[27] A. R. T. Morrison, V. Van Beusekom, M. Ramdin, L. J. P. Van Den Broeke, T. J. H. Vlugt, and W. De Jong, “Modeling the Electrochemical Conversion of Carbon Dioxide to Formic Acid or Formate at Elevated Pressures,” *J. Electrochem. Soc.*, vol. 166, no. 4, pp. E77–E86, 2019, doi: 10.1149/2.0121904jes.
[28] M. R. Singh, J. D. Goodpaster, A. Z. Weber, M. Head-Gordon, and A. T. Bell, “Mechanistic insights into electrochemical reduction of CO_2 over Ag using density functional theory and transport models,” *Proc. Natl. Acad. Sci. U.S.A.*, vol. 114, no. 42, Oct. 2017, doi: 10.1073/pnas.1713164114.

[29] E. W. Lees, B. A. W. Mowbray, F. G. L. Parlane, and C. P. Berlinguette, “Gas diffusion electrodes and membranes for CO2 reduction electrolysers,” *Nat Rev Mater*, vol. 7, no. 1, pp. 55–64, Sep. 2021, doi: 10.1038/s41578-021-00356-2.

[30] S. Chinnathambi, M. Ramdin, and T. J. H. Vlugt, “Mass Transport Limitations in Electrochemical Conversion of CO2 to Formic Acid at High Pressure,” *Electrochem*, vol. 3, no. 3, pp. 549–569, Sep. 2022, doi: 10.3390/electrochem3030038.

[31] G. Marcandalli, M. C. O. Monteiro, A. Goyal, and M. T. M. Koper, “Electrolyte Effects on CO $_2$ Electrochemical Reduction to CO,” *Acc. Chem. Res.*, vol. 55, no. 14, pp. 1900–1911, Jul. 2022, doi: 10.1021/acs.accounts.2c00080.

[32] M. Moura De Salles Pupo and R. Kortlever, “Electrolyte Effects on the Electrochemical Reduction of CO $_2$,” *ChemPhysChem*, vol. 20, no. 22, pp. 2926–2935, Nov. 2019, doi: 10.1002/cphc.201900680.

[33] A. Bagger, W. Ju, A. S. Varela, P. Strasser, and J. Rossmeisl, “Electrochemical CO $_2$ Reduction: A Classification Problem,” *ChemPhysChem*, vol. 18, no. 22, pp. 3266–3273, Nov. 2017, doi: 10.1002/cphc.201700736.

[34] Y. Hori, K. Kikuchi, and S. Suzuki, “PRODUCTION OF CO AND CH $_4$ IN ELECTROCHEMICAL REDUCTION OF CO $_2$ AT METAL ELECTRODES IN AQUEOUS HYDROGENCARBONATE SOLUTION,” *Chem. Lett.*, vol. 14, no. 11, pp. 1695–1698, Nov. 1985, doi: 10.1246/cl.1985.1695.

[35] Y. Hori, “Electrochemical CO2 Reduction on Metal Electrodes,” in *Modern Aspects of Electrochemistry*, C. G. Vayenas, R. E. White, and M. E. Gamboa-Aldeco, Eds., in Modern Aspects of Electrochemistry, vol. 42. New York, NY: Springer New York, 2008, pp. 89–189. doi: 10.1007/978-0-387-49489-0_3.

[36] Y. Hou, Y.-L. Liang, P.-C. Shi, Y.-B. Huang, and R. Cao, “Atomically dispersed Ni species on N-doped carbon nanotubes for electroreduction of CO2 with nearly 100% CO selectivity,” *Applied Catalysis B: Environmental*, vol. 271, p. 118929, Aug. 2020, doi: 10.1016/j.apcatb.2020.118929.

[37] X. Li *et al.*, “Exclusive Ni–N $_4$ Sites Realize Near-Unity CO Selectivity for Electrochemical CO $_2$ Reduction,” *J. Am. Chem. Soc.*, vol. 139, no. 42, pp. 14889–14892, Oct. 2017, doi: 10.1021/jacs.7b09074.

[38] N. Han *et al.*, “Ultrathin bismuth nanosheets from in situ topotactic transformation for selective electrocatalytic CO2 reduction to formate,” *Nat Commun*, vol. 9, no. 1, p. 1320, Apr. 2018, doi: 10.1038/s41467-018-03712-z.

[39] C. Masters, “The Fischer-Tropsch Reaction,” in *Advances in Organometallic Chemistry*, Elsevier, 1979, pp. 61–103. doi: 10.1016/S0065-3055(08)60321-4.

[40] D. D. Zhu, J. L. Liu, and S. Z. Qiao, “Recent Advances in Inorganic Heterogeneous Electrocatalysts for Reduction of Carbon Dioxide,” *Adv. Mater.*, vol. 28, no. 18, pp. 3423–3452, May 2016, doi: 10.1002/adma.201504766.

[41] B. A. Rosen *et al.*, “Ionic Liquid–Mediated Selective Conversion of CO $_2$ to CO at Low Overpotentials,” *Science*, vol. 334, no. 6056, pp. 643–644, Nov. 2011, doi: 10.1126/science.1209786.

[42] Y. Hori, H. Wakebe, T. Tsukamoto, and O. Koga, “Electrocatalytic process of CO selectivity in electrochemical reduction of CO2 at metal electrodes in aqueous media,” *Electrochimica Acta*, vol. 39, no. 11–12, pp. 1833–1839, Aug. 1994, doi: 10.1016/0013-4686(94)85172-7.

[43] A. A. Peterson and J. K. Nørskov, “Activity Descriptors for CO $_2$ Electroreduction to Methane on Transition-Metal Catalysts,” *J. Phys. Chem. Lett.*, vol. 3, no. 2, pp. 251–258, Jan. 2012, doi: 10.1021/jz201461p.

[44] K. P. Kuhl, T. Hatsukade, E. R. Cave, D. N. Abram, J. Kibsgaard, and T. F. Jaramillo, "Electrocatalytic Conversion of Carbon Dioxide to Methane and Methanol on Transition Metal Surfaces," *J. Am. Chem. Soc.*, vol. 136, no. 40, pp. 14107–14113, Oct. 2014, doi: 10.1021/ja505791r.

[45] S. Jin, Z. Hao, K. Zhang, Z. Yan, and J. Chen, "Advances and Challenges for the Electrochemical Reduction of CO_2 to CO: From Fundamentals to Industrialization," *Angew Chem Int Ed*, vol. 60, no. 38, pp. 20627–20648, Sep. 2021, doi: 10.1002/anie.202101818.

[46] L. Xue *et al.*, "Unraveling the Improved Co2 Adsorption and Cooh* Formation Over Cu-Decorated Zno Nanosheets for Co2 Reduction Toward C O," *SSRN Journal*, 2022, doi: 10.2139/ssrn.4192378.

[47] H. U. Sverdrup, K. V. Ragnarsdottir, and D. Koca, "On modelling the global copper mining rates, market supply, copper price and the end of copper reserves," *Resources, Conservation and Recycling*, vol. 87, pp. 158–174, Jun. 2014, doi: 10.1016/j.resconrec.2014.03.007.

[48] L. Wang *et al.*, "Bimetallic effects on Zn-Cu electrocatalysts enhance activity and selectivity for the conversion of CO2 to CO," *Chem Catalysis*, vol. 1, no. 3, pp. 663–680, Aug. 2021, doi: 10.1016/j.checat.2021.05.006.

[49] L. Wan *et al.*, "Bimetallic Cu–Zn Catalysts for Electrochemical CO_2 Reduction: Phase-Separated versus Core–Shell Distribution," *ACS Catal.*, vol. 12, no. 5, pp. 2741–2748, Mar. 2022, doi: 10.1021/acscatal.1c05272.

[50] K. Wang *et al.*, "Tuning the local electronic structure of oxygen vacancies over copper-doped zinc oxide for efficient CO2 electroreduction," *eScience*, vol. 2, no. 5, pp. 518–528, Sep. 2022, doi: 10.1016/j.esci.2022.08.002.

[51] H. S. Jeon *et al.*, "Operando Insight into the Correlation between the Structure and Composition of CuZn Nanoparticles and Their Selectivity for the Electrochemical CO_2 Reduction," *J. Am. Chem. Soc.*, vol. 141, no. 50, pp. 19879–19887, Dec. 2019, doi: 10.1021/jacs.9b10709.

[52] G. Keerthiga and R. Chetty, "Electrochemical Reduction of Carbon Dioxide on Zinc-Modified Copper Electrodes," *J. Electrochem. Soc.*, vol. 164, no. 4, pp. H164–H169, 2017, doi: 10.1149/2.0421704jes.

[53] Y.-P. Huang *et al.*, "*In situ* probing the dynamic reconstruction of copper–zinc electrocatalysts for CO_2 reduction," *Nanoscale*, vol. 14, no. 25, pp. 8944–8950, 2022, doi: 10.1039/D2NR01478E.

[54] D. Ren, B. S.-H. Ang, and B. S. Yeo, "Tuning the Selectivity of Carbon Dioxide Electroreduction toward Ethanol on Oxide-Derived Cu_x Zn Catalysts," *ACS Catal.*, vol. 6, no. 12, pp. 8239–8247, Dec. 2016, doi: 10.1021/acscatal.6b02162.

[55] L. Wu, L. Wu, C. Guo, Y. Guan, H. Wang, and J. Lu, "Progress in Electroreduction of CO2 to Form Various Fuels Based on Zn Catalysts," *Processes*, vol. 11, no. 4, p. 1039, Mar. 2023, doi: 10.3390/pr11041039.

[56] I. M. Dharmadasa and J. Haigh, "Strengths and Advantages of Electrodeposition as a Semiconductor Growth Technique for Applications in Macroelectronic Devices," *J. Electrochem. Soc.*, vol. 153, no. 1, p. G47, 2006, doi: 10.1149/1.2128120.

[57] S. T. Ren, G. H. Fan, M. L. Liang, Q. Wang, and G. L. Zhao, "Electrodeposition of hierarchical ZnO/Cu_2O nanorod films for highly efficient visible-light-driven photocatalytic applications," *Journal of Applied Physics*, vol. 115, no. 6, p. 064301, Feb. 2014, doi: 10.1063/1.4863468.

[58] R. W. Johnson, A. Hultqvist, and S. F. Bent, “A brief review of atomic layer deposition: from fundamentals to applications,” *Materials Today*, vol. 17, no. 5, pp. 236–246, Jun. 2014, doi: 10.1016/j.mattod.2014.04.026.
[59] S. M. George, “Atomic Layer Deposition: An Overview,” *Chem. Rev.*, vol. 110, no. 1, pp. 111–131, Jan. 2010, doi: 10.1021/cr900056b.
[60] C. F. Poole, Ed., *Gas chromatography*, 2nd ed. Cambridge: Elsevier, 2021.
[61] I. P. Gerothanassis, A. Troganis, V. Exarchou, and K. Barbarossou, “NUCLEAR MAGNETIC RESONANCE (NMR) SPECTROSCOPY: BASIC PRINCIPLES AND PHENOMENA, AND THEIR APPLICATIONS TO CHEMISTRY, BIOLOGY AND MEDICINE,” *Chem. Educ. Res. Pract.*, vol. 3, no. 2, pp. 229–252, 2002, doi: 10.1039/B2RP90018A.
[62] M. Łukaszewski, M. Soszko, and A. Czerwiński, “Electrochemical Methods of Real Surface Area Determination of Noble Metal Electrodes – an Overview,” *International Journal of Electrochemical Science*, vol. 11, no. 6, pp. 4442–4469, Jun. 2016, doi: 10.20964/2016.06.71.
[63] H. S. Magar, R. Y. A. Hassan, and A. Mulchandani, “Electrochemical Impedance Spectroscopy (EIS): Principles, Construction, and Biosensing Applications,” *Sensors*, vol. 21, no. 19, p. 6578, Oct. 2021, doi: 10.3390/s21196578.
[64] A. A. Bunaciu, E. G. Udriştioiu, and H. Y. Aboul-Enein, “X-Ray Diffraction: Instrumentation and Applications,” *Critical Reviews in Analytical Chemistry*, vol. 45, no. 4, pp. 289–299, Oct. 2015, doi: 10.1080/10408347.2014.949616.
[65] A. V. Girão, G. Caputo, and M. C. Ferro, “Application of Scanning Electron Microscopy–Energy Dispersive X-Ray Spectroscopy (SEM-EDS),” in *Comprehensive Analytical Chemistry*, Elsevier, 2017, pp. 153–168. doi: 10.1016/bs.coac.2016.10.002.
[66] F. A. Stevie and C. L. Donley, “Introduction to x-ray photoelectron spectroscopy,” *Journal of Vacuum Science & Technology A*, vol. 38, no. 6, p. 063204, Dec. 2020, doi: 10.1116/6.0000412.
[67] M. P. Seah, “A review of the analysis of surfaces and thin films by AES and XPS,” *Vacuum*, vol. 34, no. 3–4, pp. 463–478, Mar. 1984, doi: 10.1016/0042-207X(84)90084-8.
[68] G. S. Bumbrah and R. M. Sharma, “Raman spectroscopy – Basic principle, instrumentation and selected applications for the characterization of drugs of abuse,” *Egyptian Journal of Forensic Sciences*, vol. 6, no. 3, pp. 209–215, Sep. 2016, doi: 10.1016/j.ejfs.2015.06.001.
[69] S. Mosca, C. Conti, N. Stone, and P. Matousek, “Spatially offset Raman spectroscopy,” *Nat Rev Methods Primers*, vol. 1, no. 1, p. 21, Mar. 2021, doi: 10.1038/s43586-021-00019-0.
[70] J. C. Abanades, E. S. Rubin, M. Mazzotti, and H. J. Herzog, “On the climate change mitigation potential of CO_2 conversion to fuels,” *Energy Environ. Sci.*, vol. 10, no. 12, pp. 2491–2499, 2017, doi: 10.1039/C7EE02819A.
[71] P. Friedlingstein *et al.*, “Persistent growth of CO2 emissions and implications for reaching climate targets,” *Nature Geosci*, vol. 7, no. 10, pp. 709–715, Oct. 2014, doi: 10.1038/ngeo2248.
[72] M. K. Mondal, H. K. Balsora, and P. Varshney, “Progress and trends in CO2 capture/separation technologies: A review,” *Energy*, vol. 46, no. 1, pp. 431–441, Oct. 2012, doi: 10.1016/j.energy.2012.08.006.

[73] O. Martin *et al.*, “Indium Oxide as a Superior Catalyst for Methanol Synthesis by CO 2 Hydrogenation,” *Angew. Chem. Int. Ed.*, vol. 55, no. 21, pp. 6261–6265, May 2016, doi: 10.1002/anie.201600943.

[74] S. Sultana, P. Chandra Sahoo, S. Martha, and K. Parida, “A review of harvesting clean fuels from enzymatic CO 2 reduction,” *RSC Adv.*, vol. 6, no. 50, pp. 44170–44194, 2016, doi: 10.1039/C6RA05472B.

[75] J. Fu, K. Jiang, X. Qiu, J. Yu, and M. Liu, “Product selectivity of photocatalytic CO2 reduction reactions,” *Materials Today*, vol. 32, pp. 222–243, Jan. 2020, doi: 10.1016/j.mattod.2019.06.009.

[76] S. Ajmal *et al.*, “Zinc-Modified Copper Catalyst for Efficient (Photo-)Electrochemical CO 2 Reduction with High Selectivity of HCOOH Production,” *J. Phys. Chem. C*, vol. 123, no. 18, pp. 11555–11563, May 2019, doi: 10.1021/acs.jpcc.9b00119.

[77] M. A. Scibioh and B. Viswanathan, “Electrochemical Reduction of CO 2,” in *Carbon Dioxide to Chemicals and Fuels*, Elsevier, 2018, pp. 307–371. doi: 10.1016/B978-0-444-63996-7.00007-9.

[78] S. Ali, A. Razzaq, and S.-I. In, “Development of graphene based photocatalysts for CO2 reduction to C1 chemicals: A brief overview,” *Catalysis Today*, vol. 335, pp. 39–54, Sep. 2019, doi: 10.1016/j.cattod.2018.12.003.

[79] C. Xiao and J. Zhang, “Architectural Design for Enhanced C 2 Product Selectivity in Electrochemical CO 2 Reduction Using Cu-Based Catalysts: A Review,” *ACS Nano*, vol. 15, no. 5, pp. 7975–8000, May 2021, doi: 10.1021/acsnano.0c10697.

[80] M. M. Abdelnaby, K. Liu, K. Hassanein, and Z. Yin, “Photo/electrochemical Carbon Dioxide Conversion into C 3+ Hydrocarbons: Reactivity and Selectivity,” *ChemNanoMat*, vol. 7, no. 9, pp. 969–981, Sep. 2021, doi: 10.1002/cnma.202100106.

[81] T. Zheng, K. Jiang, and H. Wang, “Recent Advances in Electrochemical CO 2 -to-CO Conversion on Heterogeneous Catalysts,” *Adv. Mater.*, vol. 30, no. 48, p. 1802066, Nov. 2018, doi: 10.1002/adma.201802066.

[82] P. Li *et al.*, “Tuning the efficiency and product composition for electrocatalytic CO 2 reduction to syngas over zinc films by morphology and wettability,” *Green Chem.*, vol. 24, no. 4, pp. 1439–1444, 2022, doi: 10.1039/D1GC04364A.

[83] S. Liu *et al.*, “Shape-Dependent Electrocatalytic Reduction of CO 2 to CO on Triangular Silver Nanoplates,” *J. Am. Chem. Soc.*, vol. 139, no. 6, pp. 2160–2163, Feb. 2017, doi: 10.1021/jacs.6b12103.

[84] E. B. Nursanto *et al.*, “Gold catalyst reactivity for CO2 electro-reduction: From nano particle to layer,” *Catalysis Today*, vol. 260, pp. 107–111, Feb. 2016, doi: 10.1016/j.cattod.2015.05.017.

[85] H. S. Jeon *et al.*, “Operando Evolution of the Structure and Oxidation State of Size-Controlled Zn Nanoparticles during CO 2 Electroreduction,” *J. Am. Chem. Soc.*, vol. 140, no. 30, pp. 9383–9386, Aug. 2018, doi: 10.1021/jacs.8b05258.

[86] W. Luo, J. Zhang, M. Li, and A. Züttel, “Boosting CO Production in Electrocatalytic CO 2 Reduction on Highly Porous Zn Catalysts,” *ACS Catal.*, vol. 9, no. 5, pp. 3783–3791, May 2019, doi: 10.1021/acscatal.8b05109.

[87] J. Rosen, G. S. Hutchings, Q. Lu, R. V. Forest, A. Moore, and F. Jiao, “Electrodeposited Zn Dendrites with Enhanced CO Selectivity for Electrocatalytic CO 2 Reduction,” *ACS Catal.*, vol. 5, no. 8, pp. 4586–4591, Aug. 2015, doi: 10.1021/acscatal.5b00922.

[88] T.-L. Chen *et al.*, "*In situ* unraveling of the effect of the dynamic chemical state on selective CO_2 reduction upon zinc electrocatalysts," *Nanoscale*, vol. 12, no. 35, pp. 18013–18021, 2020, doi: 10.1039/D0NR03475D.

[89] P. Moreno-García *et al.*, "Selective Electrochemical Reduction of CO_2 to CO on Zn-Based Foams Produced by Cu^{2+} and Template-Assisted Electrodeposition," *ACS Appl. Mater. Interfaces*, vol. 10, no. 37, pp. 31355–31365, Sep. 2018, doi: 10.1021/acsami.8b09894.

[90] Z. Geng *et al.*, "Oxygen Vacancies in ZnO Nanosheets Enhance CO_2 Electrochemical Reduction to CO," *Angew. Chem.*, vol. 130, no. 21, pp. 6162–6167, May 2018, doi: 10.1002/ange.201711255.

[91] W. Luo, Q. Zhang, J. Zhang, E. Moioli, K. Zhao, and A. Züttel, "Electrochemical reconstruction of ZnO for selective reduction of CO2 to CO," *Applied Catalysis B: Environmental*, vol. 273, p. 119060, Sep. 2020, doi: 10.1016/j.apcatb.2020.119060.

[92] M. Morimoto *et al.*, "Visualization of catalytic edge reactivity in electrochemical CO2 reduction on porous Zn electrode," *Electrochimica Acta*, vol. 290, pp. 255–261, Nov. 2018, doi: 10.1016/j.electacta.2018.09.080.

[93] S. Lamaison *et al.*, "Zn-Cu Alloy Nanofoams as Efficient Catalysts for the Reduction of CO_2 to Syngas Mixtures with a Potential-Independent H_2 /CO Ratio," *ChemSusChem*, vol. 12, no. 2, pp. 511–517, Jan. 2019, doi: 10.1002/cssc.201802287.

[94] J. Zeng *et al.*, "Coupled Copper–Zinc Catalysts for Electrochemical Reduction of Carbon Dioxide," *ChemSusChem*, vol. 13, no. 16, pp. 4128–4139, Aug. 2020, doi: 10.1002/cssc.202000971.

[95] L. Xue *et al.*, "Surface modification and reconstruction of ZnO hollow microspheres for selective electroreduction of CO2 to CO," *Journal of Alloys and Compounds*, vol. 882, p. 160703, Nov. 2021, doi: 10.1016/j.jallcom.2021.160703.

[96] M. Šćepanović, M. Grujić-Brojčin, K. Vojisavljević, S. Bernik, and T. Srećković, "Raman study of structural disorder in ZnO nanopowders," *Journal of Raman Spectroscopy*, vol. 41, no. 9, pp. 914–921, 2010, doi: 10.1002/jrs.2546.

[97] K. Reimann and K. Syassen, "Raman scattering and photoluminescence in Cu 2 O under hydrostatic pressure," *Phys. Rev. B*, vol. 39, no. 15, pp. 11113–11119, May 1989, doi: 10.1103/PhysRevB.39.11113.

[98] N. M. Vuong, N. D. Chinh, B. T. Huy, and Y.-I. Lee, "CuO-Decorated ZnO Hierarchical Nanostructures as Efficient and Established Sensing Materials for H2S Gas Sensors," *Sci Rep*, vol. 6, no. 1, p. 26736, May 2016, doi: 10.1038/srep26736.

[99] H. Guzmán, F. Zammillo, D. Roldán, C. Galletti, N. Russo, and S. Hernández, "Investigation of Gas Diffusion Electrode Systems for the Electrochemical CO2 Conversion," *Catalysts*, vol. 11, no. 4, p. 482, Apr. 2021, doi: 10.3390/catal11040482.

[100] T. Cheng, H. Xiao, and W. A. Goddard, "Reaction Mechanisms for the Electrochemical Reduction of CO_2 to CO and Formate on the Cu(100) Surface at 298 K from Quantum Mechanics Free Energy Calculations with Explicit Water," *J. Am. Chem. Soc.*, vol. 138, no. 42, pp. 13802–13805, Oct. 2016, doi: 10.1021/jacs.6b08534.

[101] X. Zhi, Y. Jiao, Y. Zheng, A. Vasileff, and S.-Z. Qiao, "Selectivity roadmap for electrochemical CO2 reduction on copper-based alloy catalysts," *Nano Energy*, vol. 71, p. 104601, May 2020, doi: 10.1016/j.nanoen.2020.104601.

[102] M. J. Isaacson, F. R. McLarnon, and E. J. Cairns, “Current Density and ZnO Precipitation-Dissolution Distributions in Zn - ZnO Porous Electrodes and Their Effect on Material Redistribution: A Two-Dimensional Mathematical Model,” *J. Electrochem. Soc.*, vol. 137, no. 7, pp. 2014–2021, Jul. 1990, doi: 10.1149/1.2086856.
[103] C. M. López and K.-S. Choi, “Electrochemical Synthesis of Dendritic Zinc Films Composed of Systematically Varying Motif Crystals,” *Langmuir*, vol. 22, no. 25, pp. 10625–10629, Dec. 2006, doi: 10.1021/la0611864.
[104] L. Wang *et al.*, “Bimetallic effects on Zn-Cu electrocatalysts enhance activity and selectivity for the conversion of CO2 to CO,” *Chem Catalysis*, vol. 1, no. 3, pp. 663–680, Aug. 2021, doi: 10.1016/j.checat.2021.05.006.
[105] M. P. L. Kang, M. J. Kolb, F. Calle-Vallejo, and B. S. Yeo, “The Role of Undercoordinated Sites on Zinc Electrodes for CO $_2$ Reduction to CO,” *Adv Funct Materials*, vol. 32, no. 23, p. 2111597, Jun. 2022, doi: 10.1002/adfm.202111597.
[106] Y. Lu, B. Han, C. Tian, J. Wu, D. Geng, and D. Wang, “Efficient electrocatalytic reduction of CO2 to CO on an electrodeposited Zn porous network,” *Electrochemistry Communications*, vol. 97, pp. 87–90, Dec. 2018, doi: 10.1016/j.elecom.2018.11.002.
[107] D. H. Won *et al.*, “Highly Efficient, Selective, and Stable CO $_2$ Electroreduction on a Hexagonal Zn Catalyst,” *Angew. Chem. Int. Ed.*, vol. 55, no. 32, pp. 9297–9300, Aug. 2016, doi: 10.1002/anie.201602888.
[108] D. L. T. Nguyen *et al.*, “Selective CO $_2$ Reduction on Zinc Electrocatalyst: The Effect of Zinc Oxidation State Induced by Pretreatment Environment,” *ACS Sustainable Chem. Eng.*, vol. 5, no. 12, pp. 11377–11386, Dec. 2017, doi: 10.1021/acssuschemeng.7b02460.
[109] A. Jo, “Enhanced electrochemical conversion of CO2 to CO at bimetallic Ag-Zn catalysts formed on polypyrrole-coated electrode,” *Journal of Catalysis*, p. 8, 2021.
[110] Z. Zhang *et al.*, “‘Two Ships in a Bottle’ Design for Zn–Ag–O Catalyst Enabling Selective and Long-Lasting CO $_2$ Electroreduction,” *J. Am. Chem. Soc.*, vol. 143, no. 18, pp. 6855–6864, May 2021, doi: 10.1021/jacs.0c12418.
[111] Z. Chen, G. Zhang, J. Prakash, Y. Zheng, and S. Sun, “Rational Design of Novel Catalysts with Atomic Layer Deposition for the Reduction of Carbon Dioxide,” *Adv. Energy Mater.*, vol. 9, no. 37, p. 1900889, Oct. 2019, doi: 10.1002/aenm.201900889.
[112] M. Schreier *et al.*, “Solar conversion of CO2 to CO using Earth-abundant electrocatalysts prepared by atomic layer modification of CuO,” *Nat Energy*, vol. 2, no. 7, p. 17087, Jun. 2017, doi: 10.1038/nenergy.2017.87.
[113] X. Zheng *et al.*, “Sulfur-Modulated Tin Sites Enable Highly Selective Electrochemical Reduction of CO2 to Formate,” *Joule*, vol. 1, no. 4, pp. 794–805, Dec. 2017, doi: 10.1016/j.joule.2017.09.014.
[114] D. Ren *et al.*, “Atomic Layer Deposition of ZnO on CuO Enables Selective and Efficient Electroreduction of Carbon Dioxide to Liquid Fuels,” *Angew. Chem. Int. Ed.*, vol. 58, no. 42, pp. 15036–15040, Oct. 2019, doi: 10.1002/anie.201909610.
[115] K. A. Alim, V. A. Fonoberov, and A. A. Balandin, “Origin of the optical phonon frequency shifts in ZnO quantum dots,” *Appl. Phys. Lett.*, vol. 86, no. 5, p. 053103, Jan. 2005, doi: 10.1063/1.1861509.
[116] N. Ben Moussa *et al.*, “Synthesis of ZnO sol–gel thin-films CMOS-Compatible,” *RSC Adv.*, vol. 11, no. 37, pp. 22723–22733, 2021, doi: 10.1039/D1RA02241E.

[117] S. Tafazoli, M. Yusufoğlu, T. Balkan, and S. Kaya, “In-situ Surface Enhanced Raman Spectroscopy Investigations on Surface Transformations of Oxide Derived Copper Electrodes During CO2RR,” *Journal of Catalysis*, p. S0021951723001550, May 2023, doi: 10.1016/j.jcat.2023.04.021.

[118] Y.-C. Liang and C.-C. Wang, “Surface crystal feature-dependent photoactivity of ZnO–ZnS composite rods *via* hydrothermal sulfidation,” *RSC Adv.*, vol. 8, no. 9, pp. 5063–5070, 2018, doi: 10.1039/C7RA13061A.

[119] R. Al-Gaashani, S. Radiman, A. R. Daud, N. Tabet, and Y. Al-Douri, “XPS and optical studies of different morphologies of ZnO nanostructures prepared by microwave methods,” *Ceramics International*, vol. 39, no. 3, pp. 2283–2292, Apr. 2013, doi: 10.1016/j.ceramint.2012.08.075.

[120] P. Kejzlar, J. Machuta, and I. Nová, “Comparison of the Structure of CuZn40MnAl Alloy Casted into Sand and Metal Moulds,” *Manufacturing Technology*, vol. 17, no. 1, pp. 44–48, Feb. 2017, doi: 10.21062/ujep/x.2017/a/1213-2489/MT/17/1/44.

Chapter 7: Appendix

Appendix A: Supporting Information for Modification of ZnO by Electrodeposited Cu_xO for Enhancing CO Selectivity.

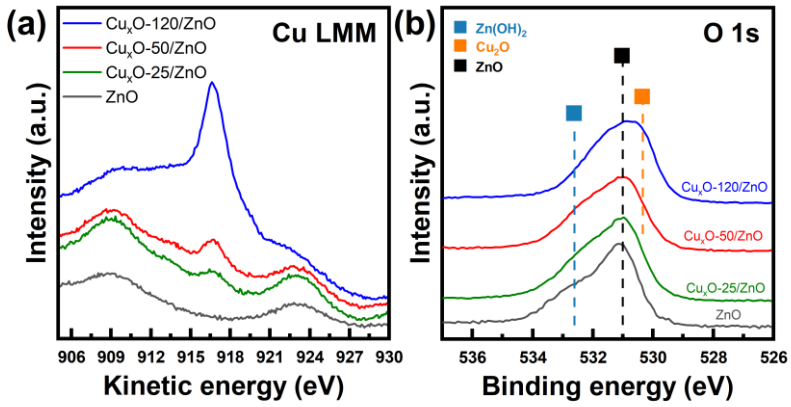

Figure A1.1. XPS spectra of as-prepared electrodes: (a) Cu LMM (b) O 1s.

Table A1.1. FE of liquid products obtained at 2 different potentials after 1 h of electrolysis in CO_2-saturated 0.1 M $KHCO_3$ analyzed by H-NMR.

	Cu_xO-50/ZnO	ZnO
-0.8 V	0.46% $HCOO^-$	0.4% $HCOO^-$
-1.2 V	4.11% $HCOO^-$	1.5% $HCOO^-$

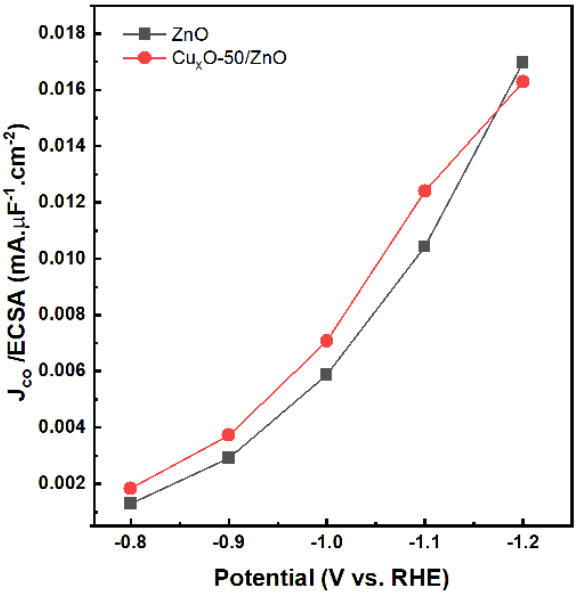

Figure A1.2. ECSA-normalized J_{CO} of Cu_xO-50/ZnO and ZnO electrodes.

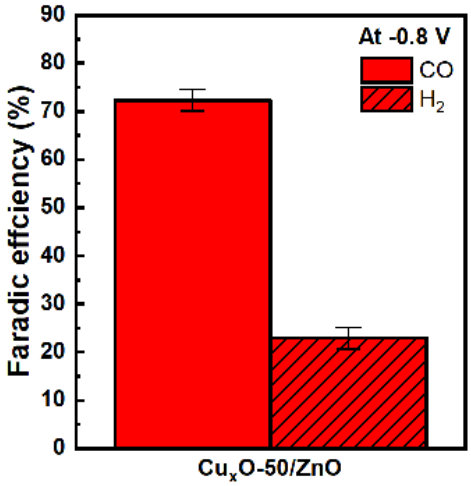

Figure A1. 3. Faradaic efficiency (FE) of the gaseous product of Cu_xO-50/ZnO electrode at -0.8 V, measured three times for consistency.

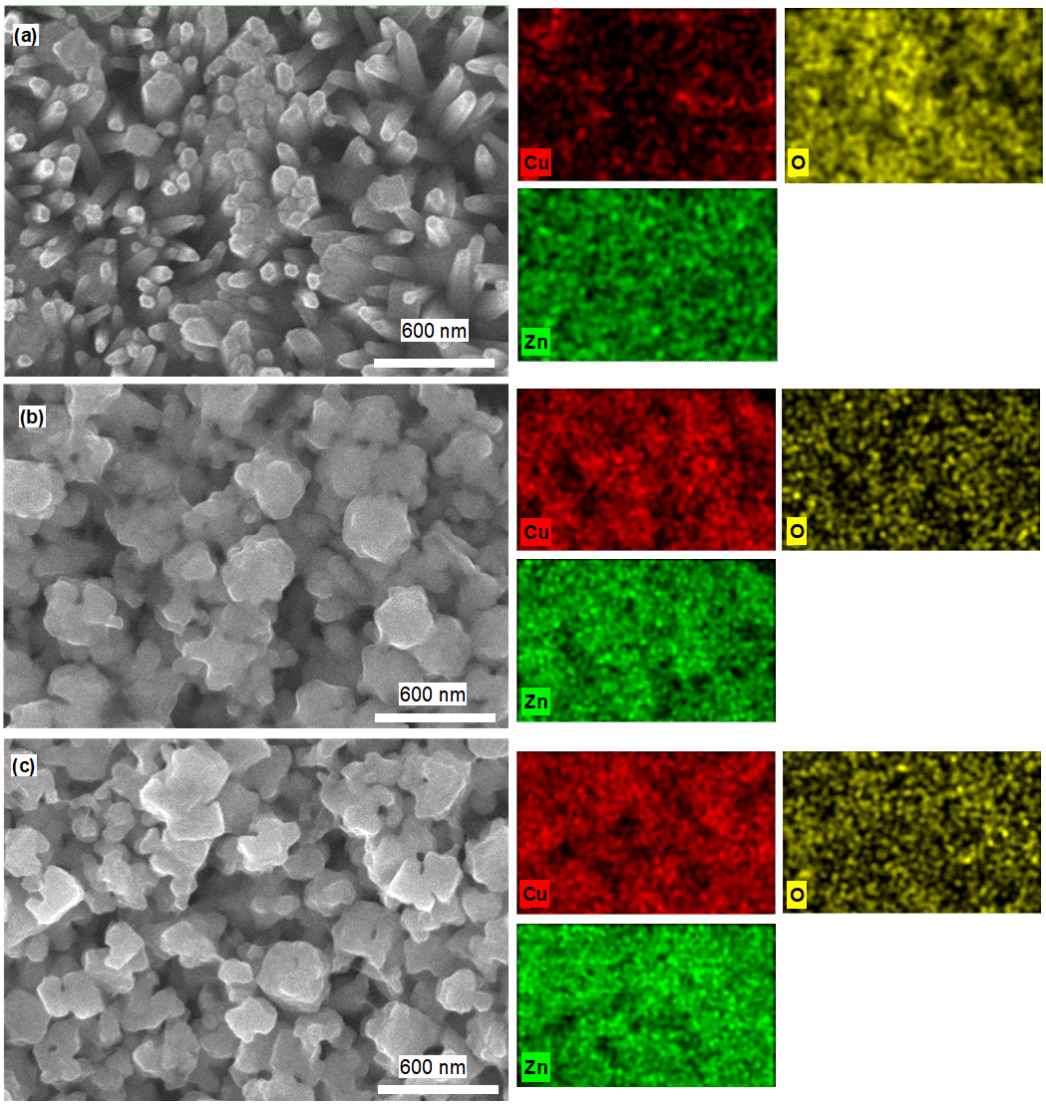

Figure A1.4. Elemental mapping obtained by FESEM-EDS of (a) fresh Cu_xO-50/ZnO, after 1 h electrolysis at (b) -0.8 V and (c) -1.2 V.

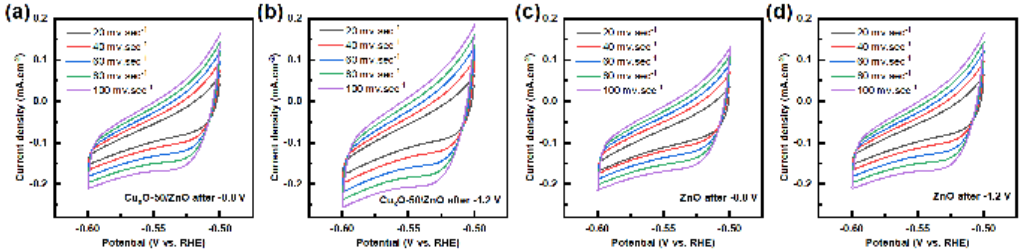

Figure A1.5. CV scans at different scan rates in CO_2-saturated 0.1 M $KHCO_3$ of (a) Cu_xO-50/ZnO after -0.8 V, and (b) after -1.2 V. ZnO electrode after (c) -0.8 V and (d) -1.2 V.

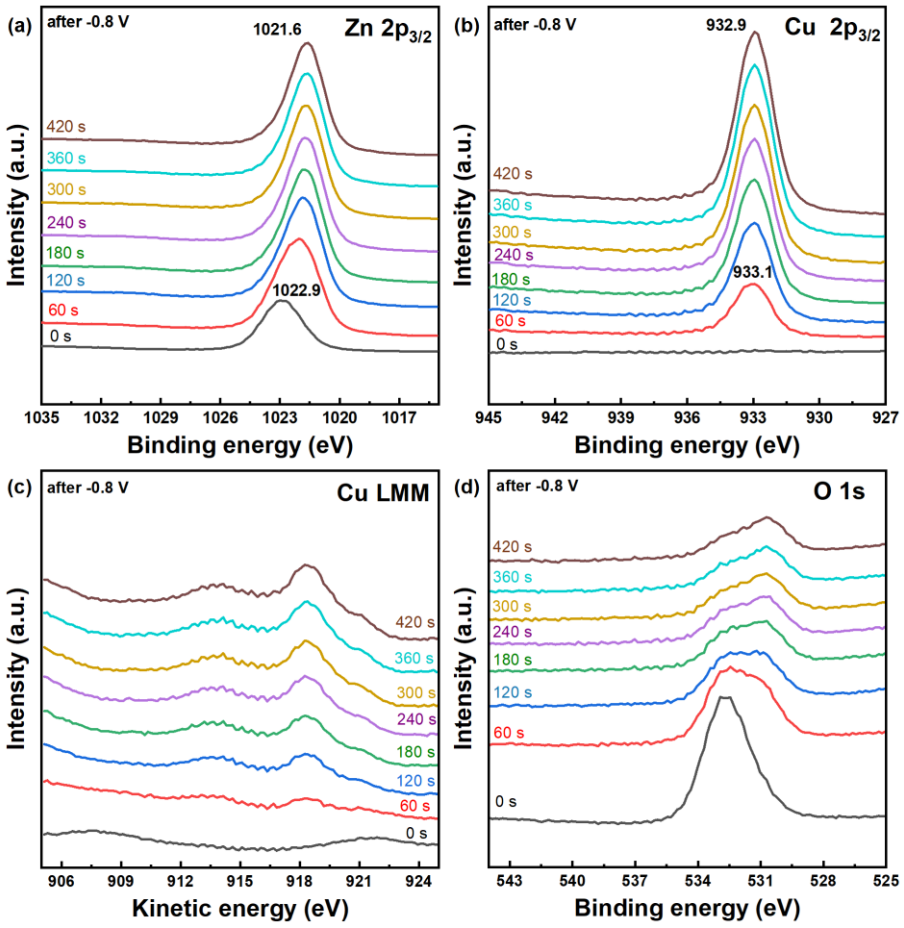

Figure A1.6. XPS depth profile analysis of Cu_xO-50/ZnO after 1 h of electrolysis at -0.8 V (a) Zn $2p_{3/2}$ (b) Cu $2p_{3/2}$ (c) Cu LMM (d) O 1s.

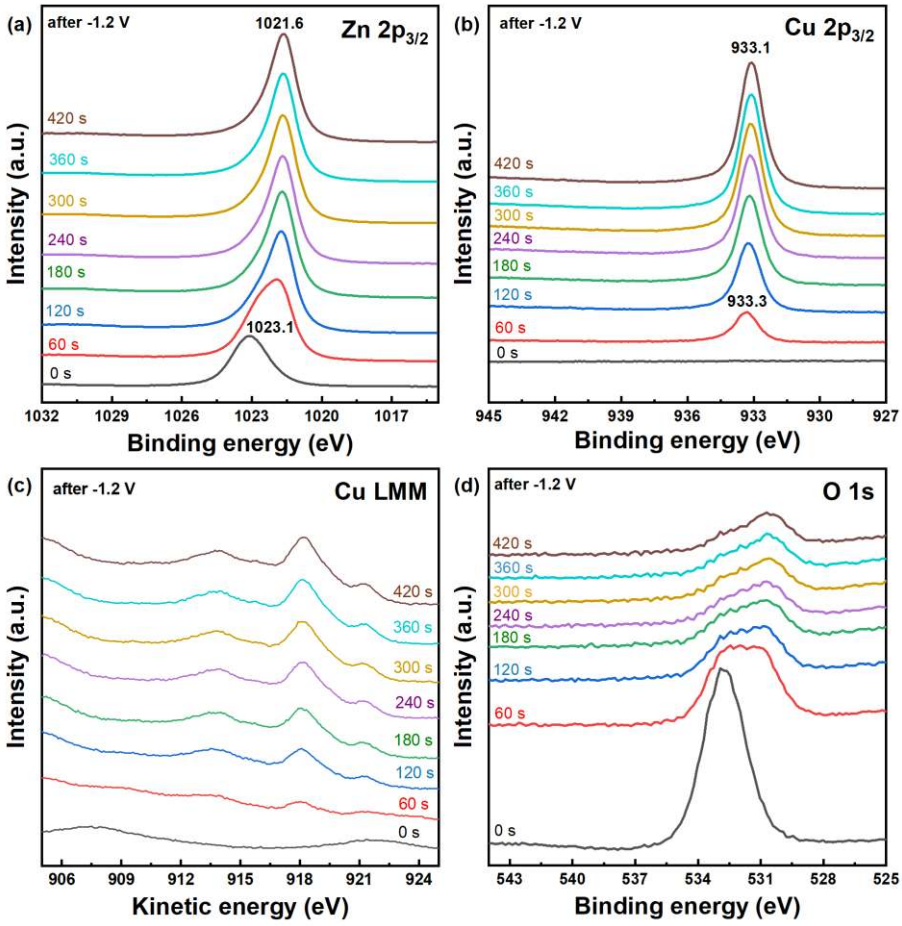

Figure A1.7. XPS depth profile analysis of Cu_xO-50/ZnO after 1 h of electrolysis at -1.2 V (a) Zn $2p_{3/2}$ (b) Cu $2p_{3/2}$ (c) Cu LMM (d) O 1s

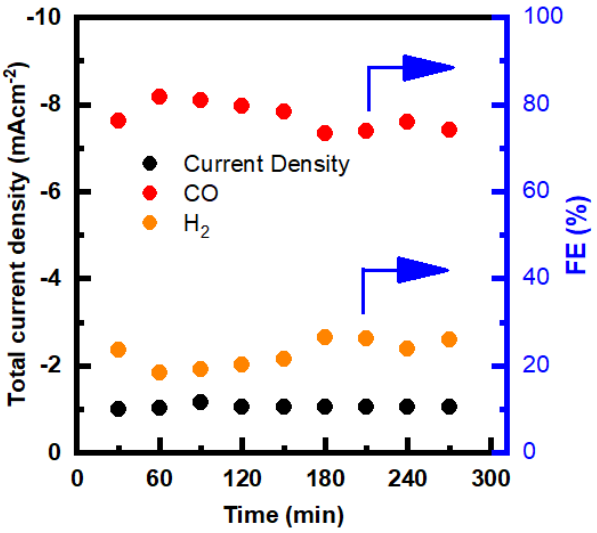

Figure A1.8. The stability test of Cu_xO-50/ZnO at -0.8 V in 0.1 M $KHCO_3$.

Appendix B Supporting Information for Modification of ZnO by ALD Cu_xO for Enhancing CO Selectivity

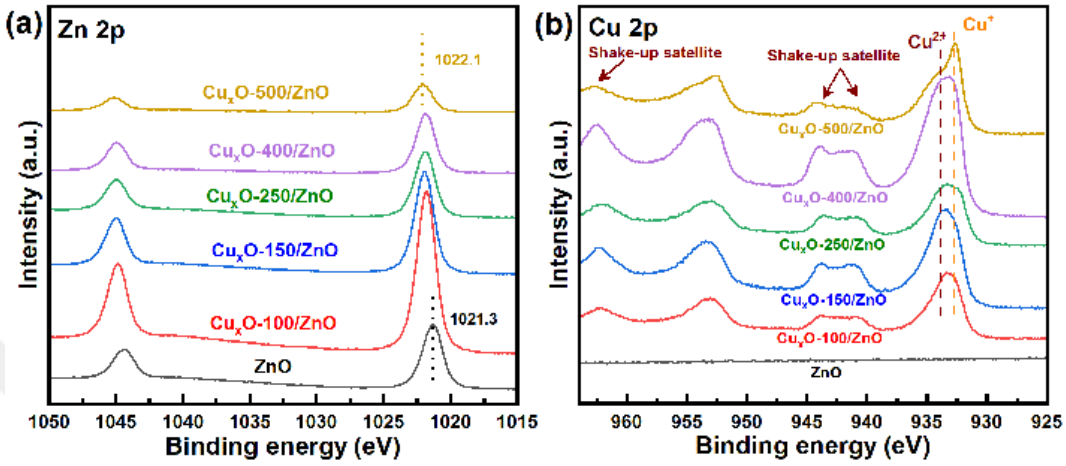

Figure B1.1. XPS spectra of as-prepared electrodes (a) Zn 2p (b) Cu 2p.

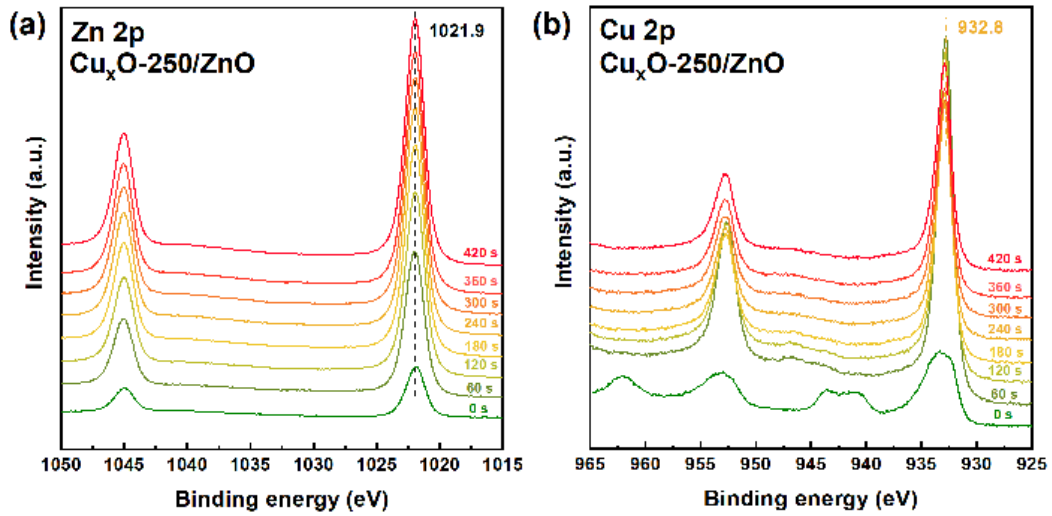

Figure B1.2. XPS spectra of as-prepared electrodes (a) Zn 2p (b) Cu 2p**.**

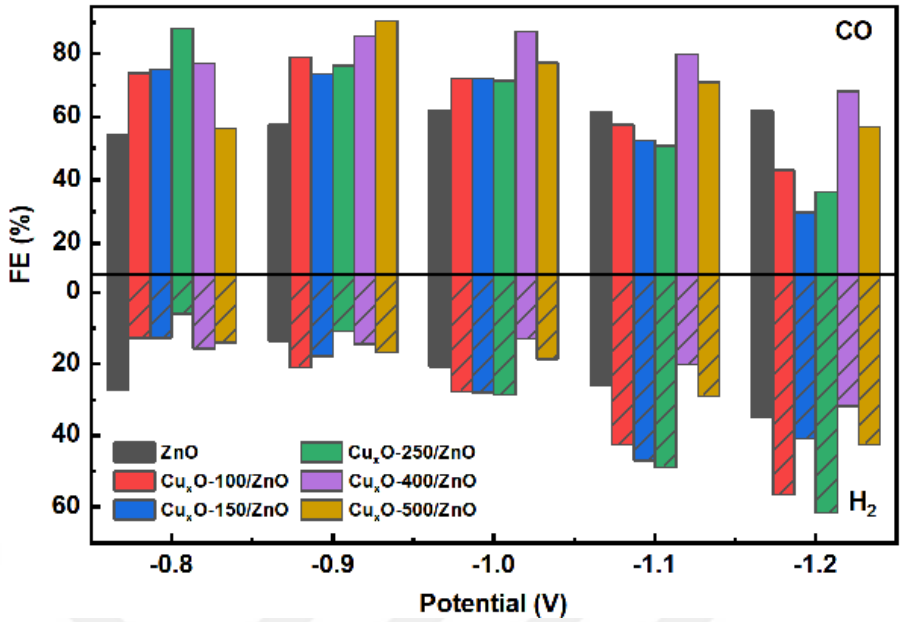

Figure B1.3. FEs of gaseous products of the 6 electrodes, pre-reduced at -0.7 V for 30 min. The same electrodes were used at all potentials, each potential was applied for 30 mins sequentially.

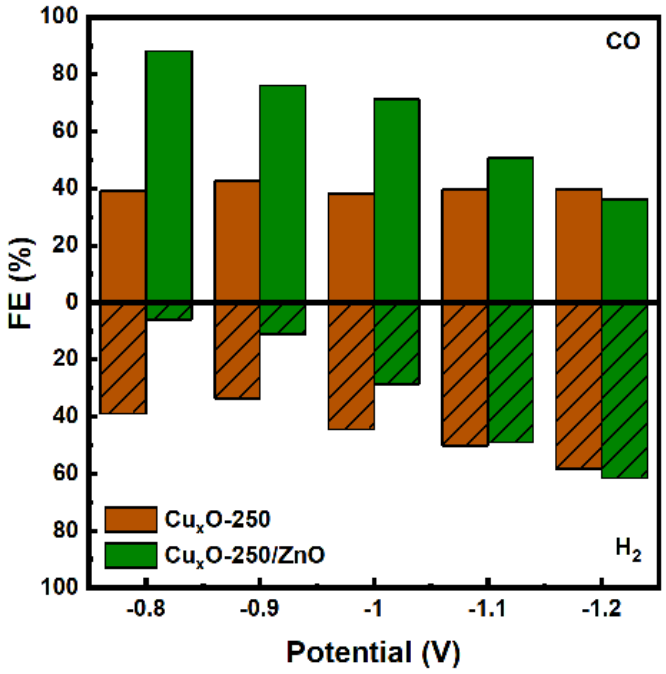

Figure B1.4. FEs of gaseous products of the 6 electrodes, pre-reduced at -0.7 V for 30 min. The same electrodes were used at all potentials, each potential was applied for 30 mins sequentially.

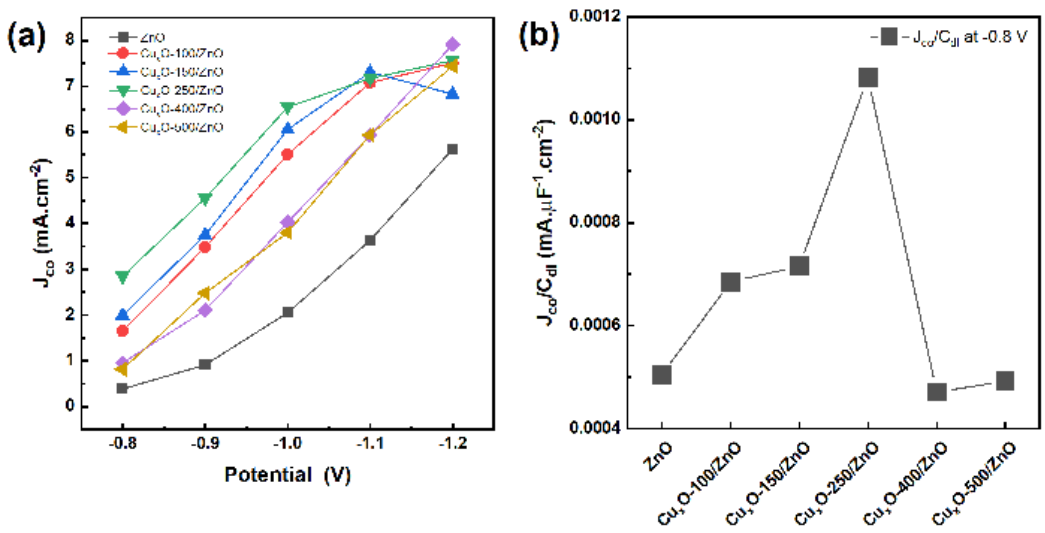

Figure B1.5. (a) Partial current density of CO (J_{CO}) at five different potentials. (b). ECSA-normalized J_{CO} at -0.8 V estimated by dividing J_{CO} by C_{dl} found after -0.8 V.

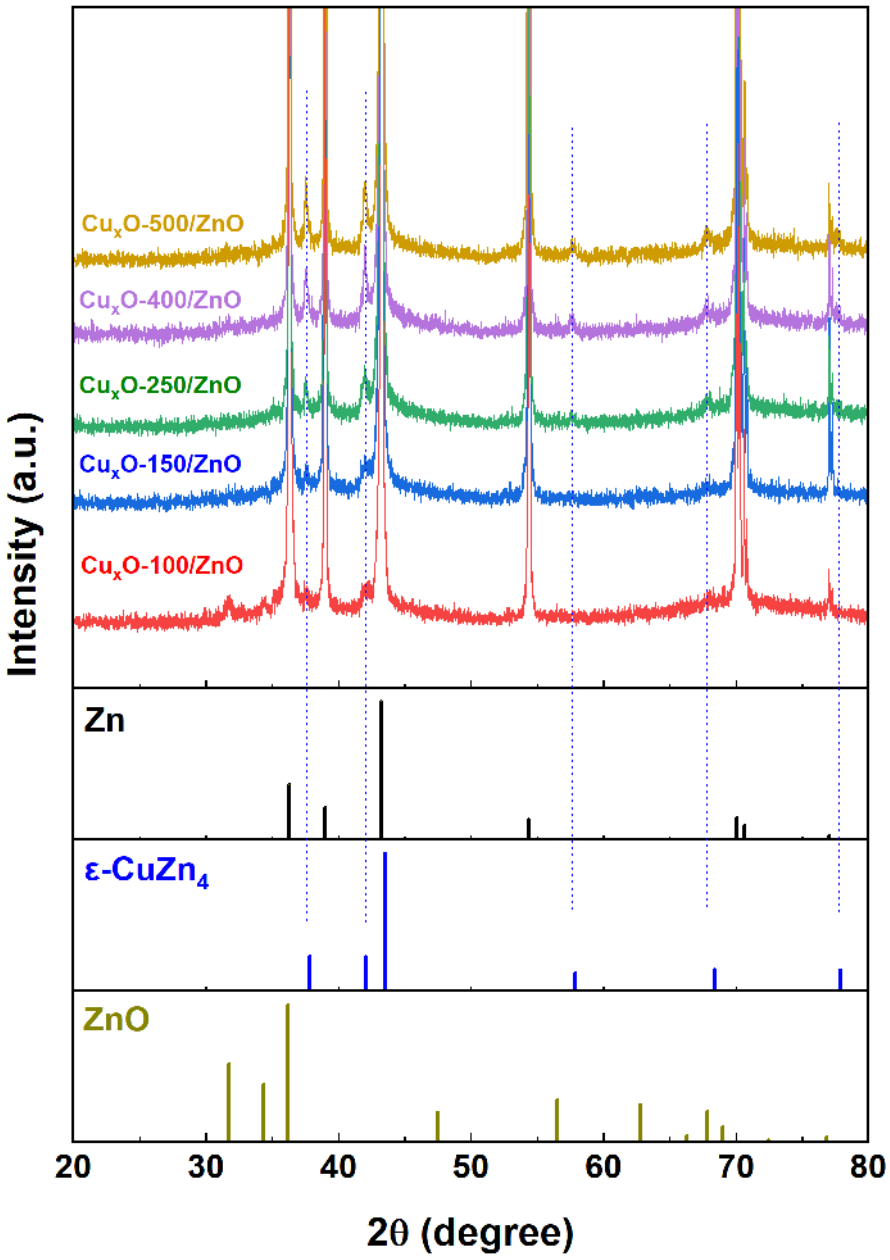

Figure B1.6. XRD reflections obtained after pre-reduction at -0.7 V for 30 min in 0.1 M $KHCO_3$.

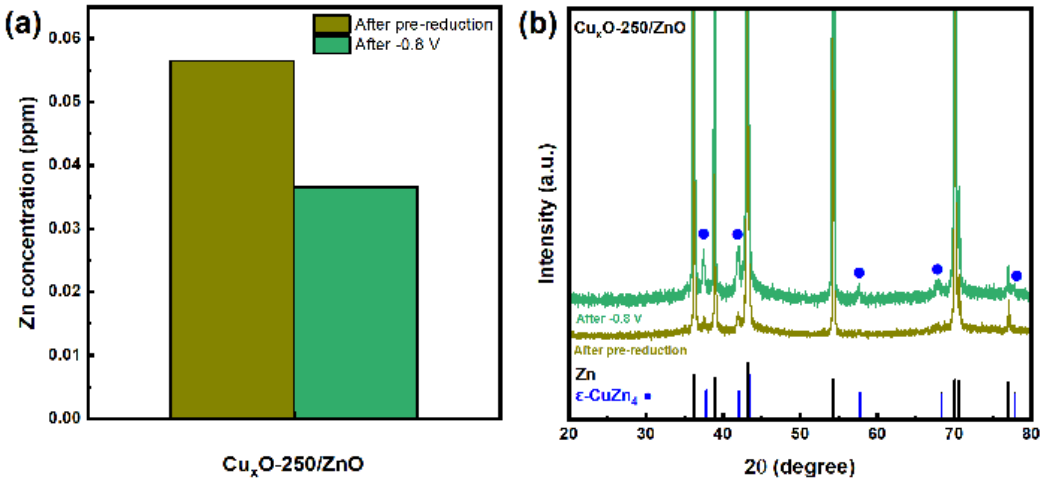

Figure B1.7. (a) Zn concentration in the electrolyte after pre-reduction and CO_2RR at -0.8 V obtained from ICP. It's noteworthy that before initiating CO_2RR at -0.8 V, a pre-reduction step was carried out utilizing the same electrolyte. (b). represents the XRD reflection after pre-reduction step and CO_2RR at -0.8 V in 0.1 M $KHCO_3$ for Cu_xO-250/ZnO.

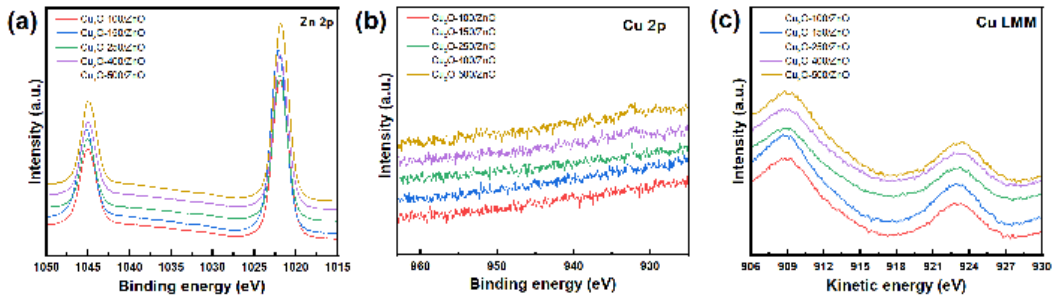

Figure B1.8. (a) Zn concentration in the electrolyte after pre-reduction and CO_2RR at -0.8 V obtained from ICP. It's noteworthy that before initiating CO_2RR at -0.8 V, a pre-reduction step was carried out utilizing the same electrolyte. (b). represents the XRD reflection after pre-reduction step and CO_2RR at -0.8 V in 0.1 M $KHCO_3$ for Cu_xO-250/ZnO.

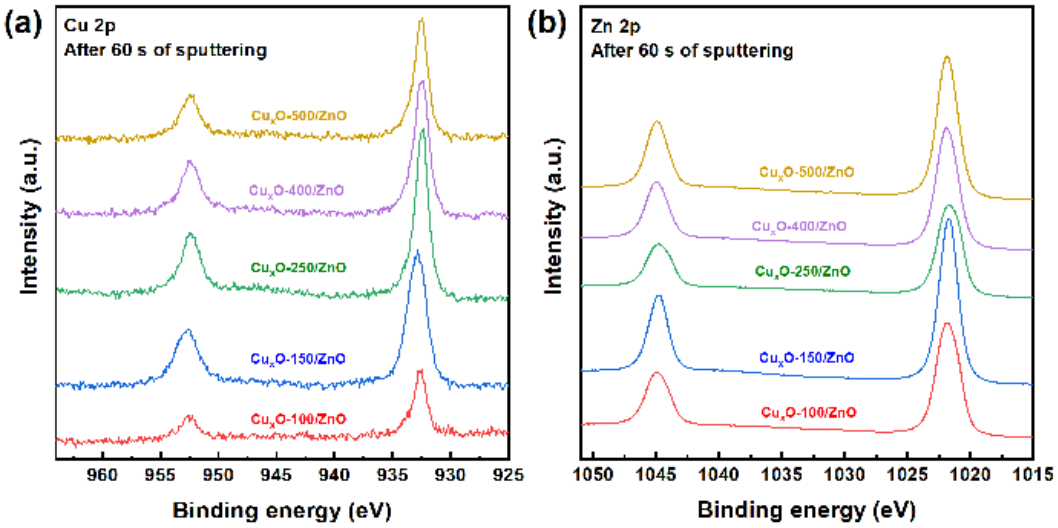

Figure B1.9. (a) Zn 2p, (b) Cu 2p XPS spectra of the electrodes after CO_2RR at -0.8 V., recorded after 60 s of sputtering with Ar^+ at sputtering rate of 0.2 $nm.s^{-1}$.

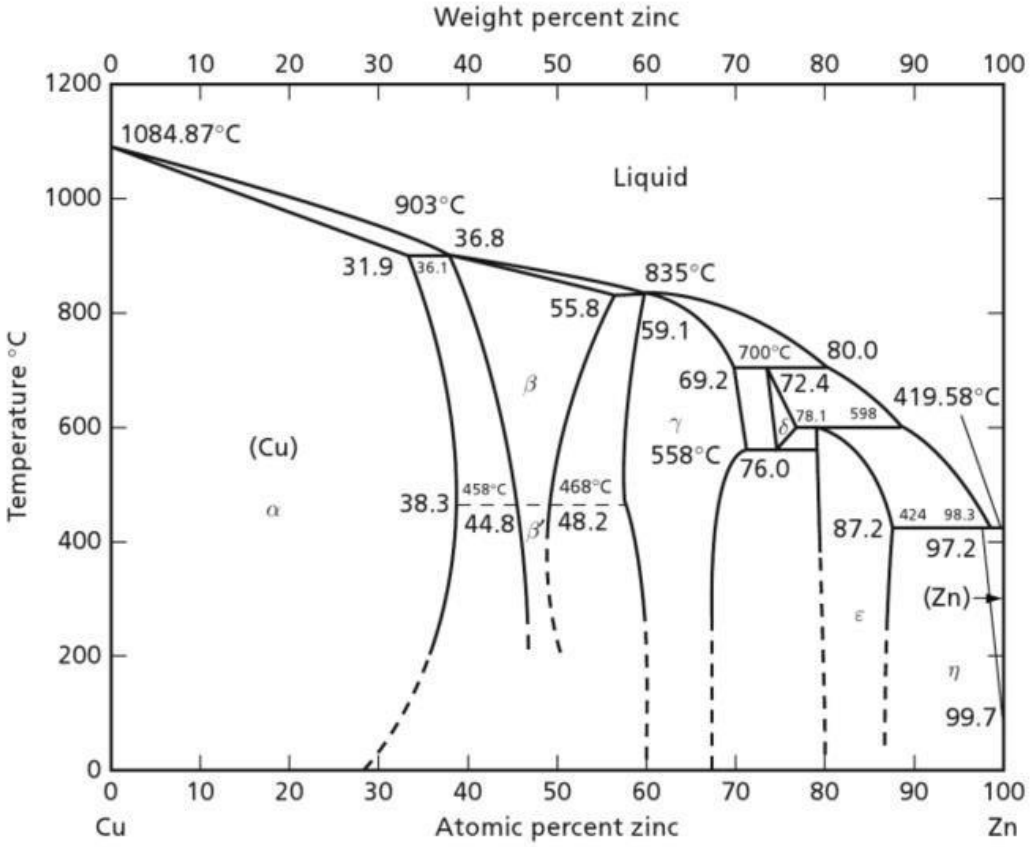

Figure B1. 10. The equilibrium Cu-Zn binary phase diagram used for quantitative calculation of each phase [120]

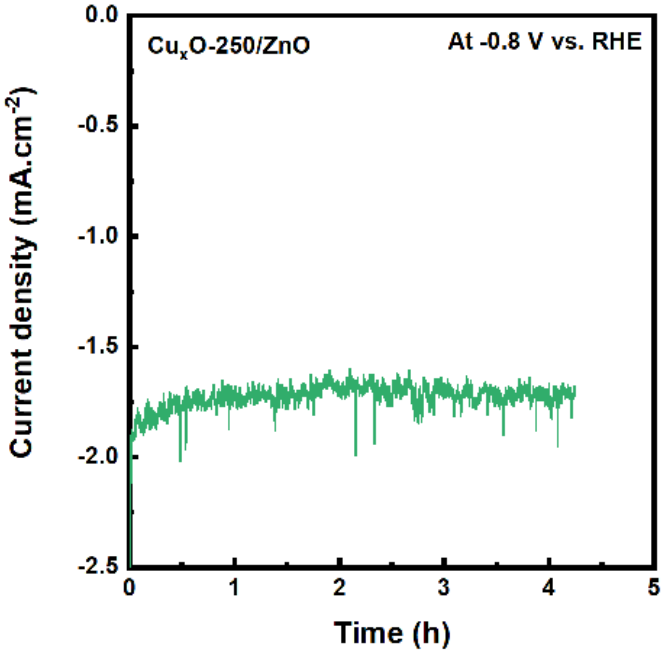

Figure B1.11. Stability test of Cu_xO-250/ZnO at -0.8 V. The current density was maintained stable for more than 4 h.